Use Authorization

In presenting this thesis in partial fulfillment of the requirements for an advanced degree at Idaho State University, I agree that the Library shall make it freely available for inspection. I further state that permission to download and/or print my thesis for scholarly purposes may be granted by the Dean of the Graduate School, Dean of my academic division, or by the University Librarian. It is understood that any copying or publication of this thesis for financial gain shall not be allowed without my written permission.

Signature: _____

Date: _____

FUNDAMENTAL PARAMETERS FOR URANIUM OXIDE CRYSTALS USING AN X-RAY DIFFRACTOMETER

by

Malwina A. Wilding

A thesis

submitted in partial fulfillment

of the requirements for the degree of

Master of Science in the Department of Nuclear Science and Engineering

Idaho State University

Fall 2016

To the Graduate Faculty:

The members of the committee appointed to examine the thesis of MALWINA A. WILDING find it satisfactory and recommend that it be accepted.

_____

Dr. Mary Lou Dunzik-Gougar,

Major Advisor

_____

Dr. Christopher McGrath,

Committee Member

_____

Dr. David Beard,

Graduate Faculty Representative

DEDICATION

Throughout my life one person has always been there during my most challenging and difficult times. I would like to dedicate this thesis to my wonderful mother, Małgorzata Chaczko, who has been very supportive. In addition to her, I wouldn't be here today without my aunt Grace Serwin, who has helped me get an education in this country. I have always been surrounded with strong and incredible Polish women, who I not only look up to but also wish to become one.

TABLE OF CONTENTS

LIST OF FIGURES

FIGURE **PAGE**

LIST OF TABLES

TABLE **PAGE**

LIST OF EQUATIONS

LIST OF ACRONYMS

Acronym	Description
BCC	body-centered cubic
CPC	closed-packed cubic
FCC	face-centered cubic
FWHM	full width at half maximum
HRSRD	high-resolution x-ray diffraction
LC	locked couple scan
NIST	national institute of standards and technology
RC	rocked curve scan
RISE	research and innovation in science and engineering complex
SEM	scanning electron microcopy
SRM	standard reference material
TEM	transmission electron microscopy
UC	unlocked couple scan
XRD	x-ray diffraction

ABSTRACT

The purpose of this research project was to analyze the quality of UO_2 crystals using single crystal XRD. Depleted UO_2 samples were grown at the RISE Complex using a high precision induction furnace. A single-crystal X-ray diffractometry was used as a non-destructive method to analyze the internal lattice parameters to determine the sizes of the single crystals and the presence of any strains in the crystal structure. This study showed that the UO_2 samples contain single crystals with less than 2% variation in the lattice constants; however, the induced strains and the sizes of the single crystals were very inconsistent across all of the samples. The average variations for sizes are 41% and 58%, and for strains are 73% and 123%. However, removing data for sample 3 and 4 (out of 8 samples) from the data set gave more consistent results. It was also determined in this study that sample holder design must be improved to facilitate more thorough analyses to give a better understanding of the crystalline behavior within the UO_2 samples.

CHAPTER I: INTRODUCTION

Background

In 1912, Max von Laue became the first to observe an X-ray diffraction (XRD) pattern, in this case from a copper sulfate crystal. When X-rays irradiate a solid, crystalline material, the atoms in the crystal diffract them. Because crystal structures are made up of equally spaced atoms in a repetitive manner, XRD patterns indicate the locations of and the distances between the atoms. In 1913, William Lawrence Bragg and his father William Henry Bragg observed that crystalline solids produce patterns of reflected X-rays and made it possible to calculate the positions of the atoms in the crystal (Bragg's Law). [1]

An x-ray diffractometer is the instrument used for analyzing crystalline structures. The x-rays have a wavelength ranging between 0.01 and 10 nm (0.1-100 Å) and are generated by a cathode-ray tube, filtered to produce approximately monochromatic radiation, and directed toward the crystalline material. The interaction of the incident X-rays with the crystalline material produces reflected (diffracted) X-rays described by Bragg's law. The diffracted X-rays are detected with a scintillation detector and the resulting signal is processed to determine the structural parameters of the crystal. [1]

When material is introduced to forces, i.e. external loads, changes in temperature, or chemical reactions, stresses are produced. Tensile stress tends to stretch or lengthen the material, whereas compressive stress will compress or shorten the material. Strain is the deformation of materials due to the stresses applied. Measuring strain in the material is crucial for deducing mechanical behavior and determining the integrity of the crystalline structures. High-quality crystals will diffract X-rays with a high efficiency due to the

equally spaced and repetitive structure of the crystal. High efficiency diffraction produces sharp and clear peaks in the diffraction pattern. On the other hand, crystals with defects will have a variety of perturbation types in the interplanar spacing of the crystal structure causing the diffraction peaks to be broadened, distorted, weakened, or a combination of all of these. [2]

Statement of Purpose

The most widely used nuclear fuel in today's commercial power reactors is UO_2. The main reason for its use is that UO_2 has excellent stability, with a high melting temperature of 2860 °C. The purpose of this research project was to determine the sizes of single crystals and the presence of any strains in the crystal structure of depleted UO_2 crystals. Analyzing the quality of UO_2 crystals will enhance our understanding of the current fuel cycle in the commercial nuclear industry. Simulations have been done of the behavior in single crystals of UO_2 for various situations with no measurable evidence; this study will give basic measurements and understanding of the crystalline behavior for depleted UO_2.

CHAPTER II: THEORY

Bragg's Law

The atoms in a crystal structure sometimes reflect x-rays that penetrate through a solid crystalline material. Since X-rays penetrate through matter far enough to pass through many planes of atoms in the structure, they contribute to multiple (*n*) observed diffractions (reflections). Bragg developed a mathematical relationship to describe this behavior. When monochromatic X-rays interact with a crystal structure, the angle of diffraction (θ) from the crystal planes in the same as the angle of incidence (θ), as shown in Figure 1 and represented in Equation 1. [3]

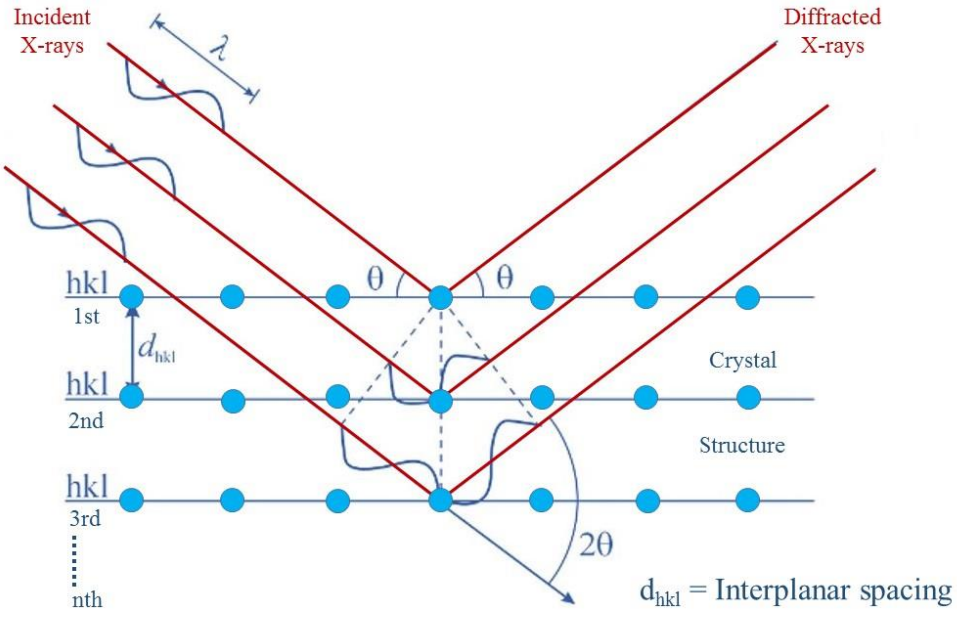

Figure 1 Diffraction of incident x-rays from a set of atomic planes separated by interplanar spacing in a crystal structure.

$$d_{hkl} = \frac{n\lambda}{2 \sin \theta}$$

Equation 1 - Bragg's Law [3]

where

d_{hkl} = *interplanar spacing of the crystal lattice planes (hkl)*
n = *the order of reflection*
λ = *wavelength of incident X-ray*
θ = *angle of incidence and reflected X-rays*

Geometry of Crystals

The groups of atoms that create a crystal structure are repeated at evenly spaced intervals maintaining their orientation to one another. This arrangement of atoms is called a *lattice*, where a *lattice point* is assigned to each atom creating a crystal structure. A *unit cell* is the smallest and simplest group of atoms, that when repeated in three-dimensions produces a crystal lattice. *Lattice parameters (lattice constants)* define and describe the crystal structure with three lattice translation vectors (*a, b, c*) on three orthogonal axes and interaxial angles (α, β, γ). [4]Figure 2 illustrates how the vectors and angles relate.

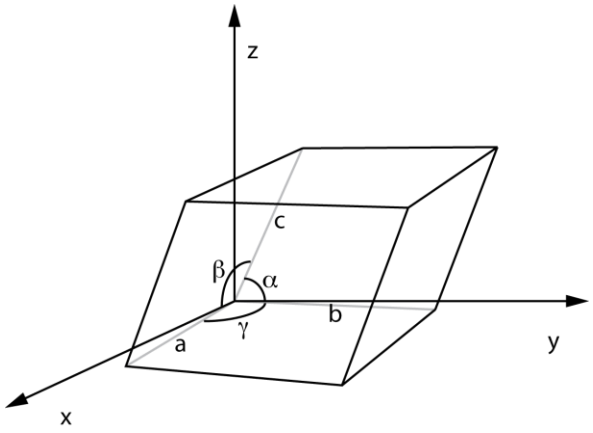

Figure 2 - Unit cell illustrating relation of lattice vectors (*a*, *b*, *c*) and angles (α, β, γ). [5]

Crystal Systems

There are seven simple crystal systems, which are summarized in Table 1.

Table 1 - Seven basic crystal systems and Bravais lattices [4]

Crystal System	Axial lengths	Axial angles	Bravais lattice
Cubic	$a = b = c$	$\alpha = \beta = \gamma = 90°$	Simple Body-Centered Face-Centered
Rhombohedral	$a = b = c$	$\alpha = \beta = \gamma \neq 90°$	Simple
Tetragonal	$a = b \neq c$	$\alpha = \beta = \gamma = 90°$	Simple Body-Centered
Hexagonal	$a = b \neq c$	$\alpha = \beta = 90°, \gamma = 120°$	Simple
Orthorhombic	$a \neq b \neq c$	$\alpha = \beta = \gamma = 90°$	Simple Body-Centered Base-Centered Face-Centered
Monoclinic	$a \neq b \neq c$	$\alpha = \beta = \gamma \neq 90°$	Simple Base-Centered
Triclinic	$a \neq b \neq c$	$\alpha \neq \beta \neq \gamma \neq 90°$	Simple

Four of the seven simple crystal systems have more than one unique lattice structure, giving a total of fourteen different types of lattices (*Bravais lattices*). The research described in this study focused on UO_2 crystals, which have a combination of simple and face-centered structure as shown in Figure 3. In each crystal system, the simple system is also known as *primitive*.

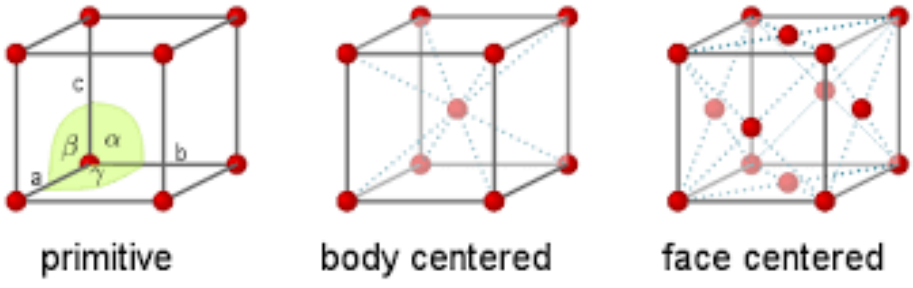

Figure 3 - Three types of cubic Bravais lattices. [6]

The primitive cubic crystal structure consists of one lattice point at each corner of the cube. Body-Centered Cubic (BCC) crystal structure has one atom in the center of a cubic unit cell surrounded by eight atoms, one at each cube corner. Face-Centered Cubic (FCC) crystal structure has one atom at the center of each cube face in addition to eight corner atoms. The FCC crystal system is also known as close-packed cubic (CPC) due to it being the most densely packed cubic system. [4]

Crystal structures of compounds of unlike atoms, like UO_2, have a combination of Bravais lattices as mentioned previously. The crystal structure of UO_2 is of the fluorite type, which is named for the mineral calcium fluorite (CaF_2). Figure 4 demonstrates the fluorite-type unit cell of UO_2, where the FCC uranium ion sublattice is interlaced with a simple cubic oxygen ion sublattice. [4]

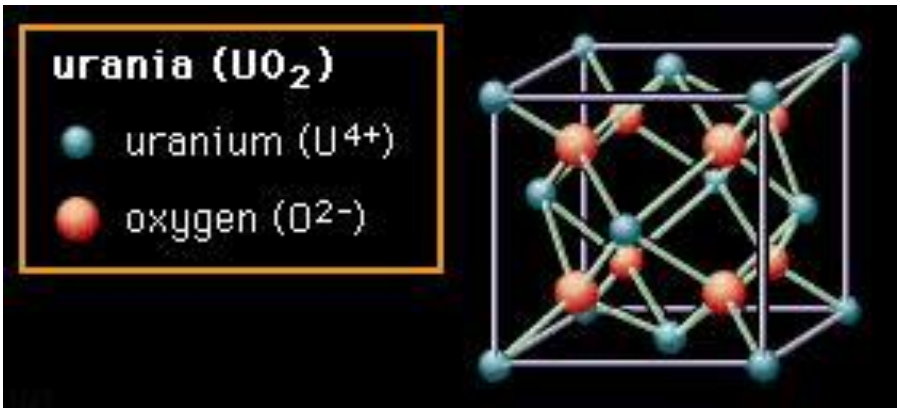

Figure 4 - Schematic of UO2 fluorite-type crystal structure. [7]

Miller Indices

Miller indices are used to specify directions and planes in the crystal structure. They use generic letters such as *hkl*, to represent numbers that relate to the coordinate systems. Figure 5 shows Miller indices and the difference between lattice points, lattice directions and lattice planes in the cubic crystal system. Lattice points are represented by *(h,k,l)*, lattice directions are represented by *[hkl]*, and *(hkl)* represent planes in the lattice structure. Figure 5 shows that *h* represents the plane perpendicular to the *x-axis*, *k* represents the plane perpendicular to the *y-axis*, and *l* represents the plane perpendicular to the *z-axis*. If a parameter is in the negative direction it will be represented with a bar above it, i.e. -1 is $\bar{1}$. [3]

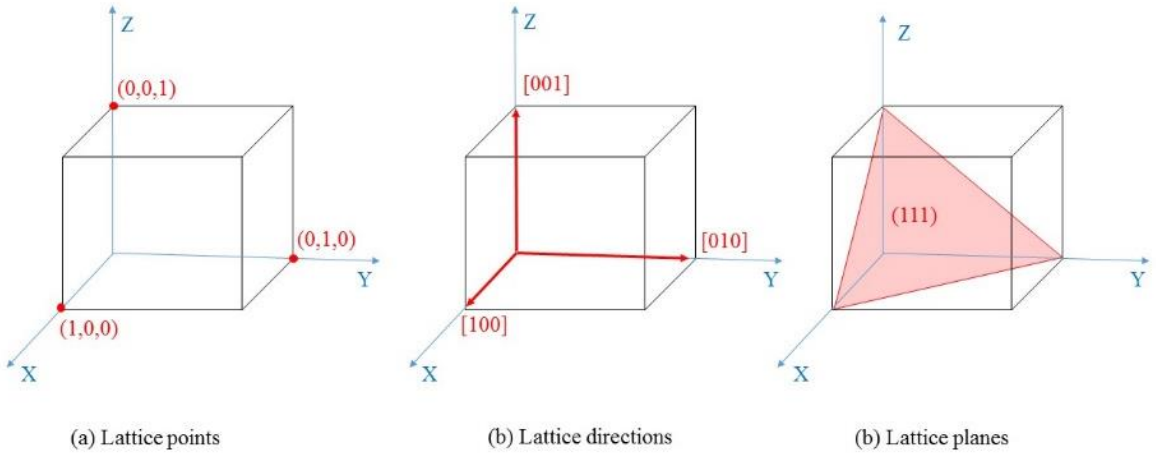

Figure 5 – Miller notation for (a) points, (b) directions, and (c) planes in a cubic system.

A lattice point represents only one point in the unit cell and is used for finding directions in the crystal structure. Lattice direction represents one unit of length in the unit cell that requires an arbitrary origin.

The following procedure, with reference to Figure 6, is used to assign Miller indices for direction in the cubic crystal system.

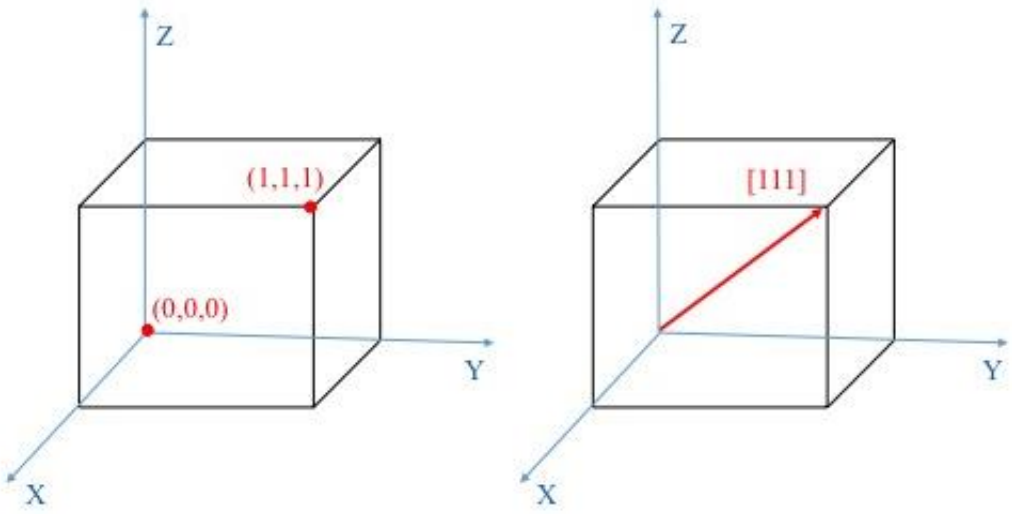

Figure 6 – Miller indices for directions in the cubic system.

1) *Draw a vector and find the coordinates of the head and tail lattice points.* Figure 6 shows two lattice points that serve as the head (1,1,1) and tail (0,0,0) of the vector.
2) *Subtract the coordinates of tail from head.* In this case we take (1,1,1) and subtract with (0,0,0) to get (1,1,1).
3) *If any fractions are present, convert to the smallest integer.* For example: (0, ½,1) will become (0,1,2) by multiplying all of the numbers by 2.
4) *Directions are enclosed with square brackets.* The final answer for direction in this case is [1,1,1] and is shown on the right in Figure 6.

The orientation of crystals is defined by planes and is defined by the following procedure in a cubic crystal system.

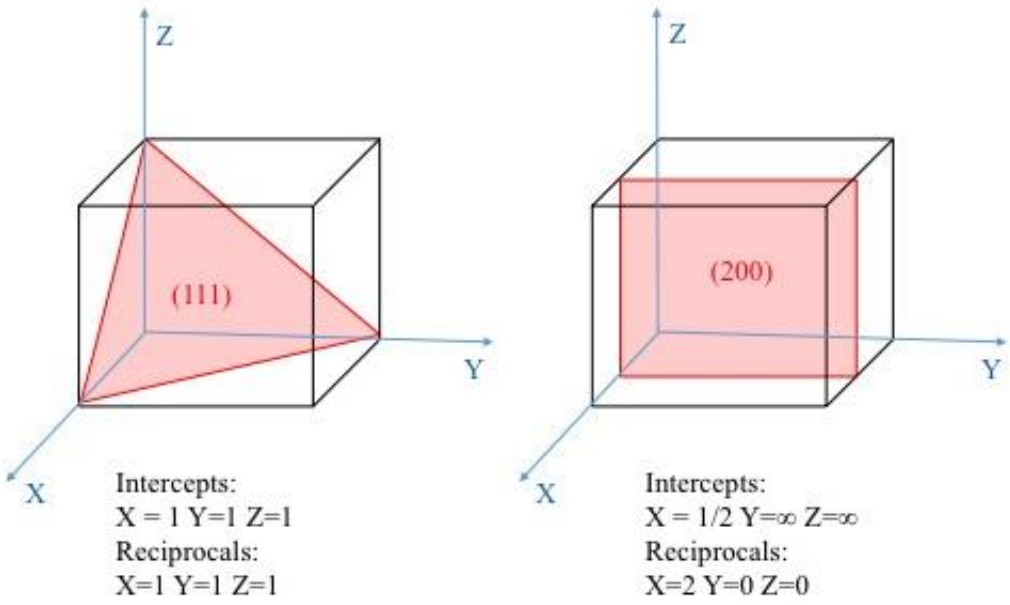

Figure 7 – Miller notation for crystal planes in the cubic system.

1) *Identify the intercepts on the x-,y-, and z-axes.* Figure 7 shows intercepts at 1,1,1 for the left picture and ½,∞,∞ for the right picture; if there is no intercept on an axis then it is taken as infinite (∞).
2) *Take reciprocals of the intercepts.* The reciprocals of 1 and ∞ are 1 and 0 respectively; therefore, in this case there are 1,1,1 for the left and 2,0,0 for the right.
3) *If any fractions are present, convert to the smallest integer.* For example: ½,0,1 will become 1,0,2 by multiplying all of the numbers by 2.
4) *Planes are enclosed with parenthesis.* The plane indications in this case are (111) for the left image and (200) for the right image in Figure 7.

This project mainly focused on (111) and (200) planes because these are the most common planes for the two cubic sublattice structures, SC and FCC, which make up a UO_2 crystal. Figure 8 shows the most commonly occurring planes for each cubic lattice structure. Defining the distance, i.e. *d*-spacing, between lattice planes in the given crystal defines its geometry. Equation 2 shows the mathematical representation for the distance (*d*) between adjacent planes in the set (*hkl*). The cubic system has vectors *a*,*b*,c of equal length and at right angles to one another; hence the parameter *a* is directly proportional to the spacing *d* of any particular set of Bragg planes (Equation 2). XRD will measure the Bragg angle, θ, for a specific *hkl* plane and using Bragg's law (Equation 1) to determine d_{hkl} will allow calculation of *a* (Equation 2).

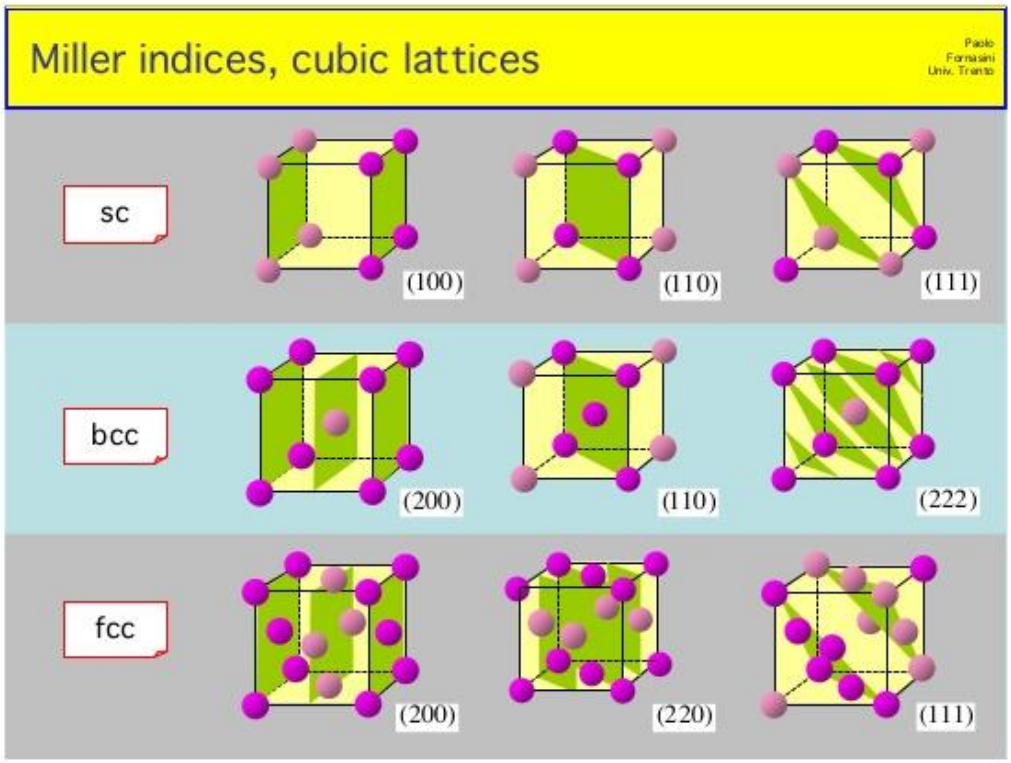

Figure 8 – Miller indices of lattice planes in the cubic system. [8]

$$a = d_{hkl}\sqrt{h^2 + k^2 + l^2}$$

Equation 2 - Interplanar spacing for the cubic crystal system [3]

where

a = lattice constant of the cube's side
d_{hkl} = interplanar spacing in the crystal
h,k,l = Miller indices of lattice plane

Contributions to Diffraction Peak Profile

X-ray diffraction from the different planes of atoms in the crystal structure produces a diffraction pattern, which consists of one or more diffraction peak at specific angle θ. The number of planes, or the thickness of the sample, affects the width of a diffraction peak. Figure 9 demonstrates how the incident and reflected X-rays and Bragg angle (θ), change based on the number of planes in the sample. A decrease in the thickness (number of planes) of the crystal causes an increase in the width of the diffraction peak ($\Delta\theta$) as shown in Figure 9 and Figure 10. Peak width (B) is a measure of the broadness of the peak, which is full width at half maximum (FWHM) of the peak's intensity. [3]

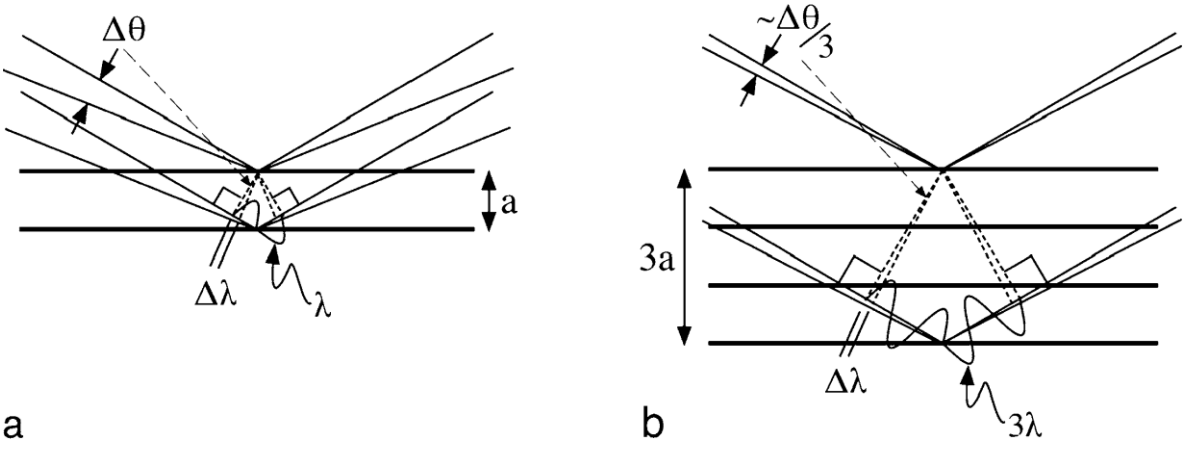

Figure 9 – Effect of crystal size on diffraction: (a) thin sample, (b) thick sample.[1]

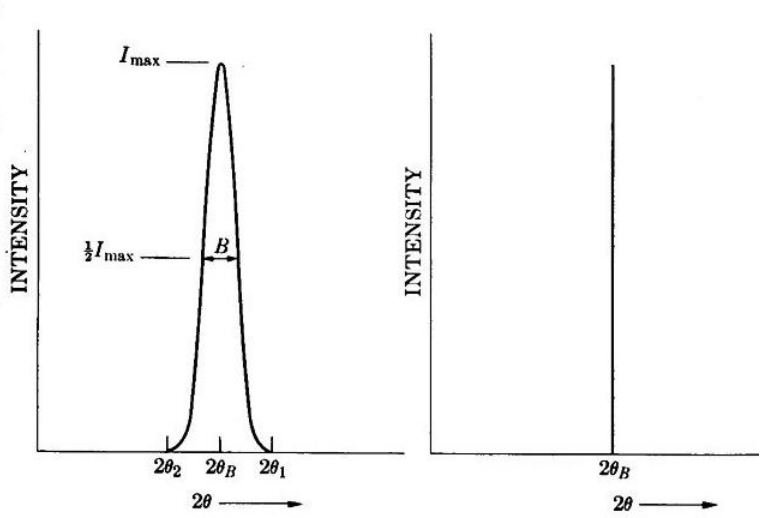

Figure 10 – Effect of crystallite size on diffraction curve: left side thin sample, right side thick sample. [3]

Many engineering materials are polycrystalline, composed of many individual single crystals. The size of an individual crystal is called the *crystallite size* when it is less than 100 nm. As explained above, crystals in this size range cause broadening of the diffraction width (*B*), which can be calculated using Scherrer's Equation (Equation 3). All diffraction curves have a measurable width even when the crystallite size exceeds 100 nm; but Equation 3 is no longer reliable in that case due to B being reduced to near 0. In this case, the most accurate way to measure grain sizes (crystallite size bigger than 100 nm) is with microscopy techniques (TEM or SEM). Application of Scherrer's equation is common for loose powders, but can also be applied to high quality single crystals. [3]

$$B_{SIZE} = \frac{0.9\lambda}{t\cos\theta}$$

Equation 3 - Scherrer's Equation [3]

where

B_{SIZE} = FWHM of the broadened diffraction curve
θ = Bragg angle of diffraction peak
λ = incident x-ray wavelength
t = average diameter of the crystallites

Many other factors contribute to diffraction-peak profile data, including instrumental peak profile, strains, and temperature factors. Equation 4 is used for diffraction peaks that are Gaussian-shaped.

$$B_{EXP} = \sqrt{B_{SIZE}{}^2 + B_{STRAIN}{}^2 + B_{INST}{}^2}$$

Equation 4 – Experimentally measured FWHM of Gaussian-shaped diffraction peak

where

B_{EXP} *= experimentally measured FWHM*
B_{SIZE} *= FWHM due to crystallite size*
B_{STRAIN} *= FWHM due to microstrain*
B_{INST} *= FWHM due to instrument*

The instrumental peak FWHM (B_{inst}) is crucial for determining the crystallite size and the microstrain broadening of the diffraction peak. The peak width from the instrument varies based on the combination of x-ray source profile and goniometer optics. The x-ray source changes peak width due to different x-ray wavelength widths and the size of the x-ray source. Goniometer optics changes peak width by varying divergence and receiving slit widths, imperfect focusing, beam size, and penetration into the sample. If the instrumental peak width is bigger than the broadening due to crystallite size, then there is no accurate way of determining crystallite size. Hence, it is recommended to use the smallest goniometer optics to get the smallest instrumental peak width for analyzing larger nanocrystallites. [9]

Finally, strains or dislocations can also deform crystal structures contributing to changes in the diffraction peak profile data. When a material is loaded with a force, it will produce stress. Strain is the deformation of the material due to the stress applied. Real crystals, whether single crystals or individual crystallites in polycrystalline aggregate, have some

dislocations and imperfections. Crystals are not comprised of atoms arranged in a perfectly regular lattice extending from one side of the crystal to the other; rather the lattice is broken up into a number of tiny blocks, each slightly disoriented one from another. Two types of stresses can be identified, microstresses and macrostresses. Microstresses can vary from one crystallite to another, which is on the microscopic scale. However, if the stress is quite uniform over a large distance, then it is referred to as macrostress. The effect of strain, both uniform and nonuniform, on the direction of x-ray reflection is shown in Figure 11. [3]

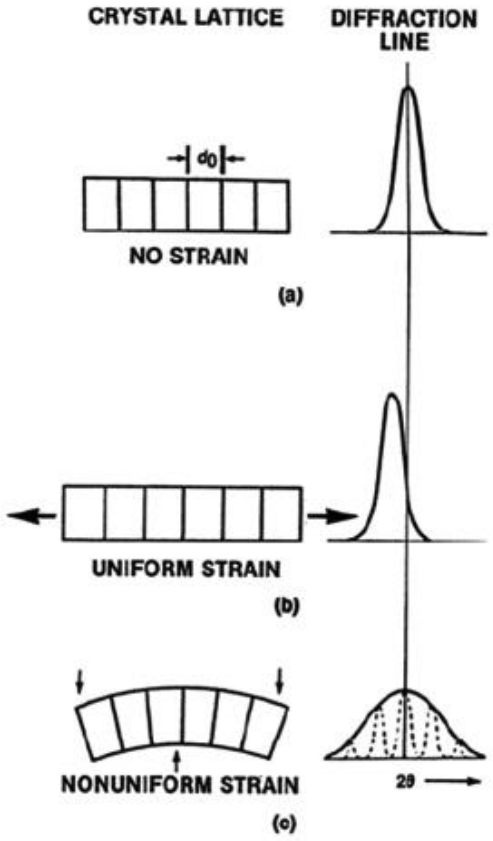

Figure 11 - Effect of uniform and non-uniform strains on diffraction peaks position and width. [10]

A section of unstrained crystal structure is shown in (a) of Figure 11, where each unstrained crystallite is evenly separated by spacing of d_0. If the crystallites have uniform tensile strain, their spacing becomes larger than d_0 and the corresponding diffraction line only shifts without any shape changes, shown in (b). Tensile (uniform) strain will only stretch or lengthen material which is on the macroscale. But, if the crystallites are compressed in a nonuniform way, the strain is on the microscale and the result is a broadened the diffraction line as shown in (c). A non-uniform strain can be directly associated with a change in *d*-spacing as shown in Figure 12. If the material is strained with compressive stress the *d*-spacing will be smaller, but the opposite happens when tensile strain is applied as shown in Figure 12.

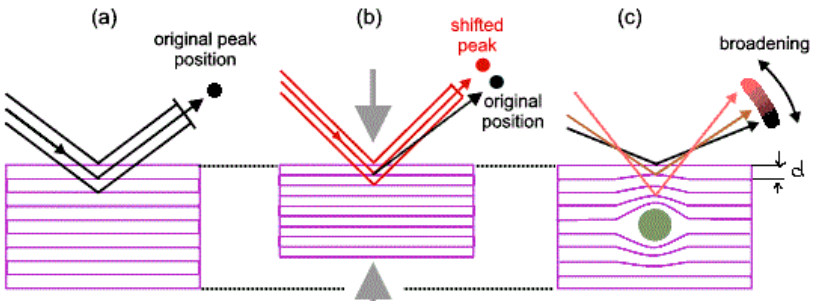

Figure 12 - Effect of strains on diffraction peak position and width: (a) unstrained sample, (b) uniform strain, (c) non-uniform strain starting at the center of the sample (green dot). [11]

The non-uniformity can be represented using Equation 5 below. The value of ε includes both tensile and compressive strain and can be divided by two to separate them only if both are assumed to be equal.

$$B_{STRAIN} = \Delta 2\theta = -2\varepsilon \tan\theta$$

Equation 5 - Non-uniform strain equation [3]

where

B_{STRAIN} = *FWHM for extra broadening of diffraction peak*
θ = *Bragg angle of diffraction peak*
ε = *strain (tensile + compressive) of crystal structure*

Another way for determining size and strain within a crystal is by using the Williamson-Hall method. This method requires a plot of $B\cos\theta$ with respect to $\sin\theta$ for multiple peaks from the crystal sample. If size broadening is the only significant contribution to the peak width, then $B\cos\theta$ is a constant for all peaks. If strain broadening is the important contribution, then $B\cos\theta$ is a linear function of $\sin\theta$. The strain component comes from the slope ($C\varepsilon$) and the size component from the intercept ($0.9\lambda/t$) of the Williamson-Hall plot as shown in Figure 13 and Equation 6. [11]

$$B = B_{SIZE} + B_{STRAIN}$$

$$(B = \frac{0.9\lambda}{t\cos\theta} - 2\varepsilon\tan\theta)\cos\theta$$

$$B\cos\theta = \frac{0.9\lambda}{t} - 2\varepsilon\sin\theta$$

Equation 6 – Equation for crystallite size and strain components for Williamson-Hall plot [11]

where

B = FWHM of total diffraction peak
Bsize = FWHM of diffraction peak due to crystalline size
Bstrain = FWHM of diffraction peak due to strain
θ = Bragg angle of diffraction peak
λ = incident x-ray wavelength
t = average crystallite size
ε = strain (tensile + compressive)

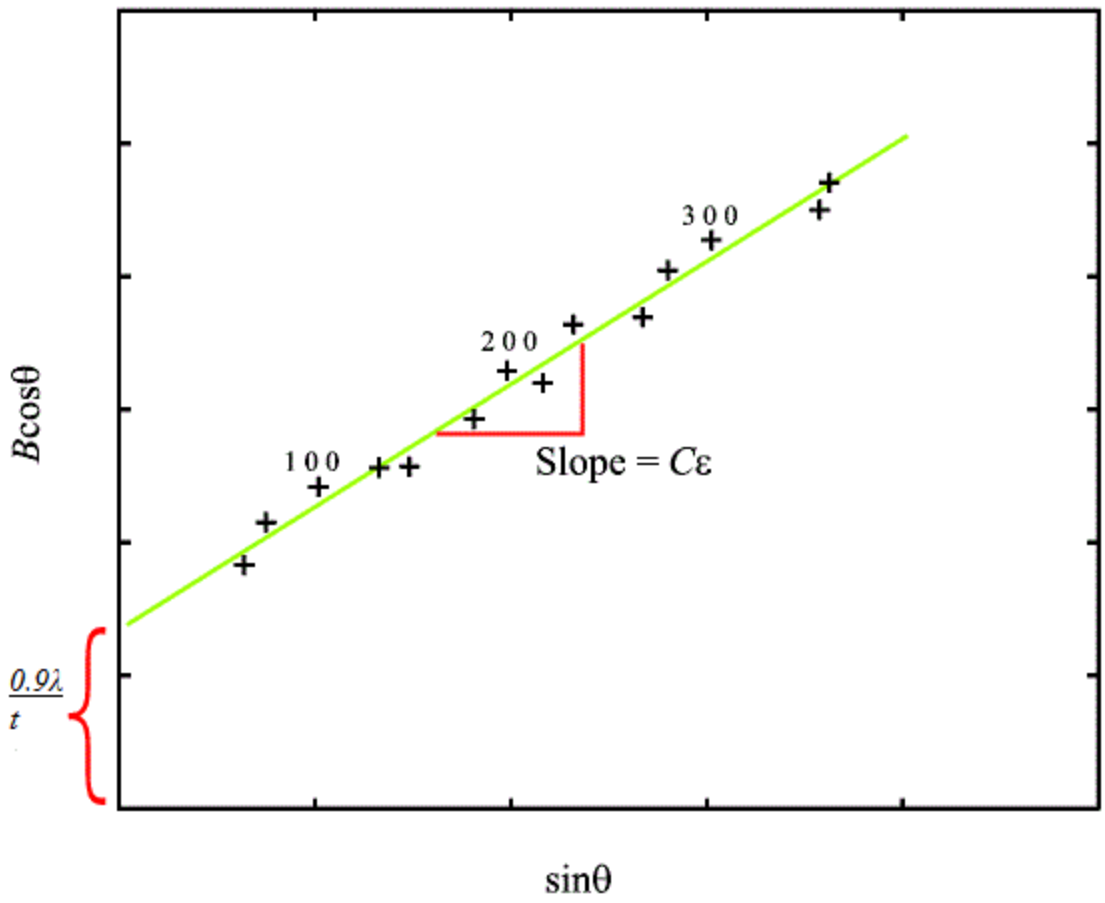

Figure 13 - Williamson-Hall plot for determining size and strain of a crystal. [11]

CHAPTER III: METHOD

Siemens D 5000 Diffractometer

An x-ray diffractometer is most commonly used for precise determination of unit cell parameters that include cell dimensions and positions of atoms within the crystal lattice. However, an XRD can be used for nearly all X-ray diffraction applications such as structure research, crystallite size, phase analysis, stress and texture measurements. An X-ray diffractometer consists of three basic elements: an X-ray tube, a sample holder, and an X-ray detector as shown in Figure 14. The mechanism that supports the sample and detector is called a goniometer. The goniometer has two independently controlled stepper motors in both horizontal and vertical modes, which allow precise movement. Each time the Bragg condition is satisfied; the detector will collect diffracted X-rays and display intensity as peaks on the screen of the computer. However, if the Bragg condition is not satisfied or the sample is not mounted properly, the detector will only collect and display background counts.[12]

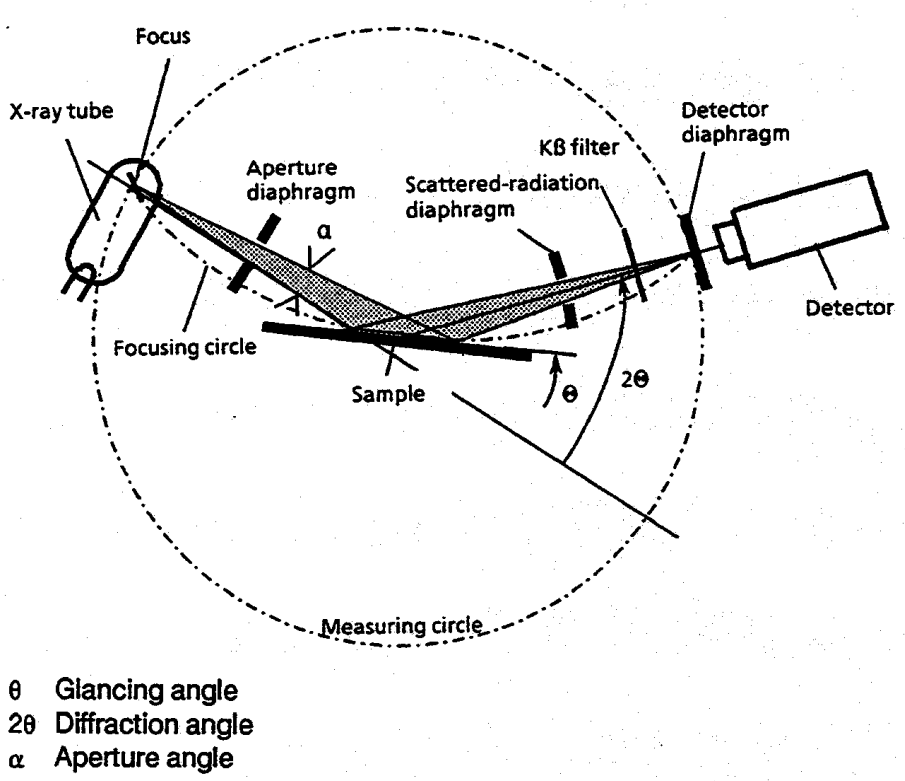

Figure 14 - Diffractometer beam path in Siemens D 5000. [12]

The x-ray tube component of an XRD must contain a source of electrons, a high accelerating voltage, and a metal target. All x-ray tubes have two electrodes, an anode (the metal target), and a cathode. The cathode is the source of electrons that are accelerated to strike the anode. Most of the energy of the incoming electrons is converted to heat and for that reason cooling water flows through the anode for heat extraction. X-ray production is a very inefficient process where only about 1% of the electrons are actually converted into X-rays. Finally, X-rays pass through the beryllium window on the side of the tube. [13]

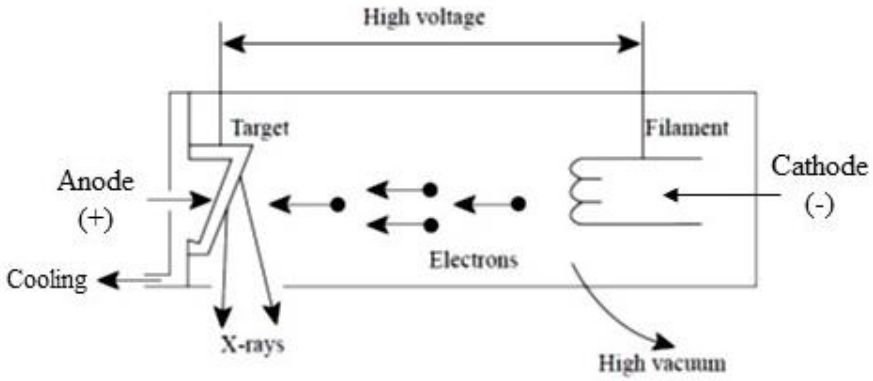

Figure 15 – Schematic of the X-ray tube in the diffractometer. [13]

Since most measurements require monochromatic X-ray radiation, a filter is used to improve the X-ray radiation by minimizing the spread of wavelengths. The x-ray diffraction pattern in Figure 16 shows two peaks, K_α and K_β, that result from using a copper target with and without a nickel filter. A nickel filter is used due to the significant difference between its absorption coefficient for the K_α and K_β components of the x-ray beam. The lower wavelength K_β x-rays are absorbed by nickel, while the K_α x-rays pass through. [3]

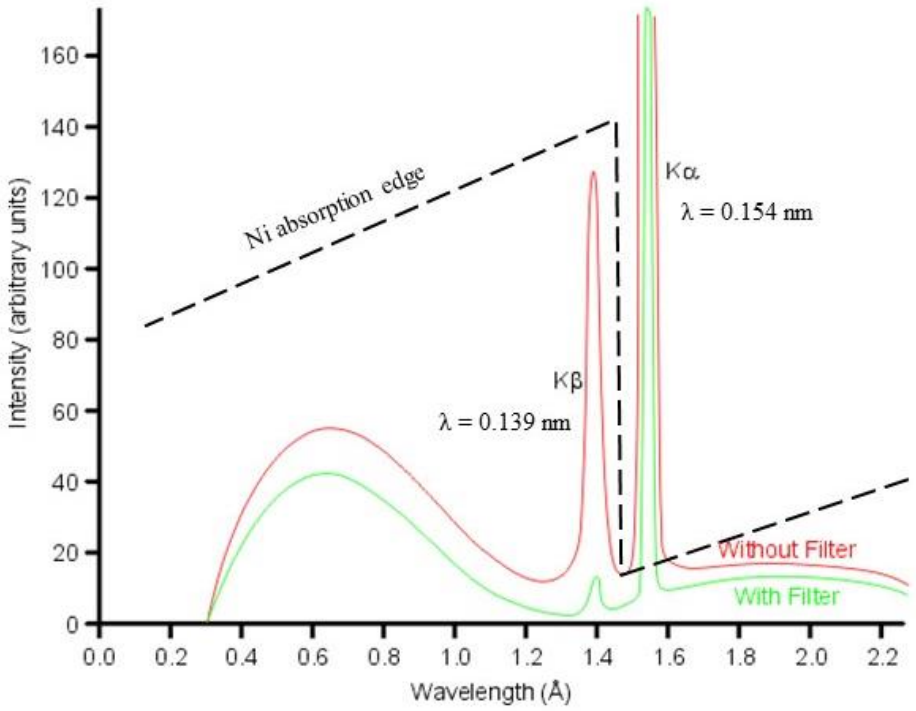

Figure 16 – X-ray spectrum for Copper target with Nickel filter. [13]

A schematic of the detector is shown in Figure 17. The detector consists of a sodium iodide (NaI) crystal doped with thallium, which converts the incident X-rays into blue light. The X-rays excite electrons from the valence shell to the conduction shell of the crystal and visible light is released when the electron returns to the valence shell. The photomultiplier tube converts the visible radiation to electrons that create an electric current that is related to the intensity of the incident X-rays. [1]

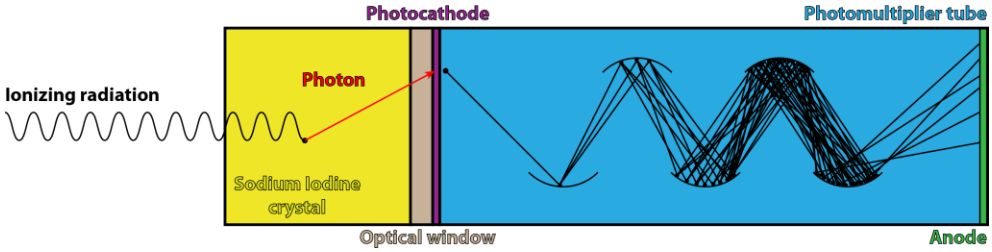

Figure 17 – Schematic of the scintillation counter. [1]

Specification

The Siemens D 5000 diffractometer used in this study is a single-crystal x-ray diffractometer with a large-diameter goniometer, a low-divergence collimator, and Soller slits. The goniometer is installed horizontally in a radiation-protection housing (lead-shielded walls and windows). Figure 18 shows the x-ray tube, an FK 60-04 air-insulated tube, and its tube stand on the left-hand side of both pictures. The tube stand has built-in radiation-alarm lamps that light up when the window shutter is open, and a safety switch, which is depressed by the diffractometer safety bracket. [12]

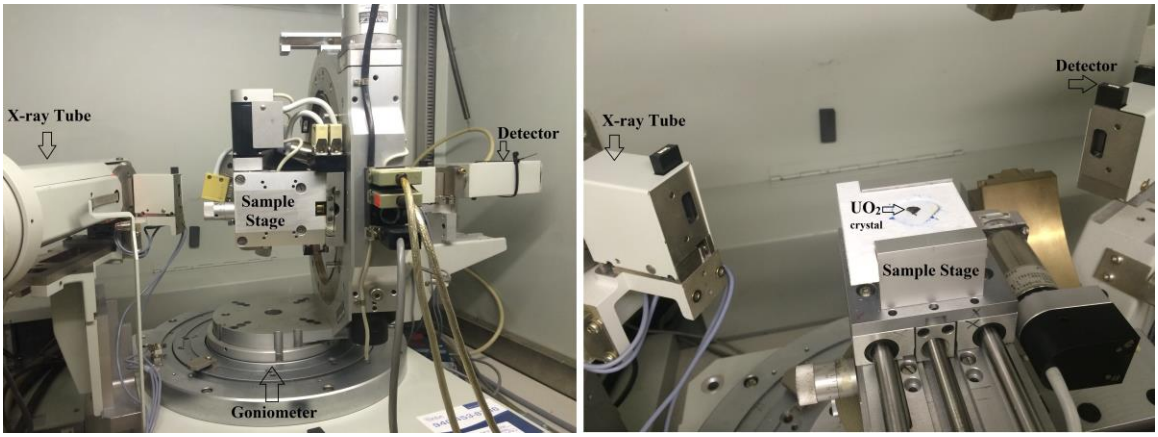

Figure 18 - D 5000 diffractometer horizontal installation, front view (left) and front-top view (right).

The goniometer is a stage that supports the sample and the detector as shown in Figure 18. It has four axes of motion to adjust sample and detector position. The four degrees of freedom are: rotation of the sample about the vertical axis, rotation of the detector about the vertical axis, tilt of the sample about the horizontal axis (χ), and rotation of the sample about the axis normal to the sample surface through the center of sample holder (φ). [12]The four degrees of freedom are shown in Figure 19.

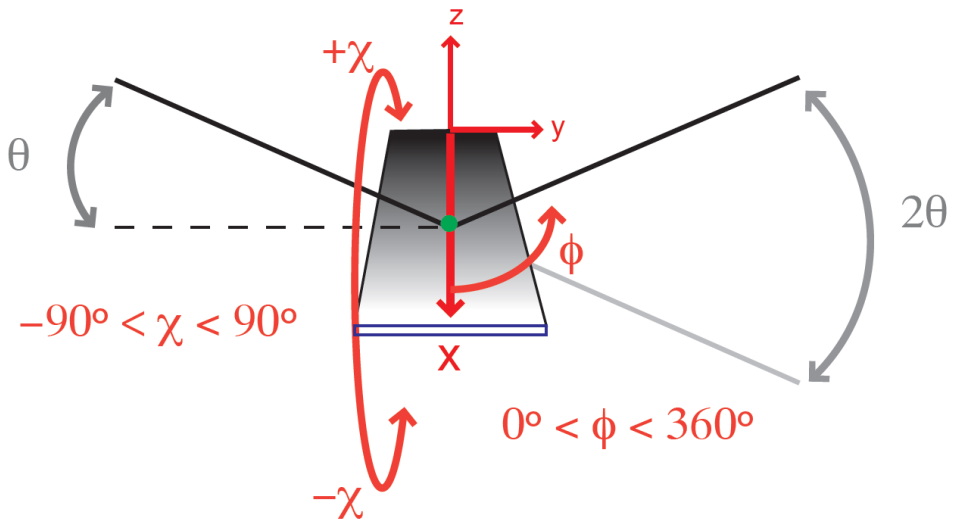

Figure 19 - Movement of the goniometer in D 5000 Diffractometer.

On the opposite side from the x-ray tube is the scintillation counter, shown in Figure 18. This particular instrument was chosen for its sensitivity to the x-rays produced by the system. The diffractometer has good peak intensities and great resolution due to focusing of the diffracted beam. Therefore, for this study two Soller slits, Cu and Ni filters, two 1-mm divergence slits, and a 0.2-mm divergence slit were used for measurements shown in Figure 20 and Figure 21. Soller slits contain set of closely spaced thin metal plates, which make low angle reflections more symmetrical and improve resolution. This arrangement is suitable for analyzing samples that produce diffraction patterns with many peaks in the low-angle region and with overlapping peaks. The amount of the sample that is irradiated by incident X-rays depends on the slit settings and on the diffraction angle. At lower 2θ, a larger area of the sample is irradiated compared to higher 2θ without any changes to the goniometer optics. [3] The exact placement and dimensions for the x-ray tube, sample holder, and detector are shown in Figure 20 and Figure 21. For optimal measurements source slit # 2 (closest to the sample) and receiving slit # 1 (closest to the sample) are a 1

mm divergence slit, whereas receiving slit # 3 (closest to the detector) is a 0.2 mm divergence slit. Furthermore, a Cu filter of 6 mm is the receiving slit # 2 for lowering counts of high quality samples and protecting the detector from burning-up, and the Ni filter is attached behind receiving slit # 1.

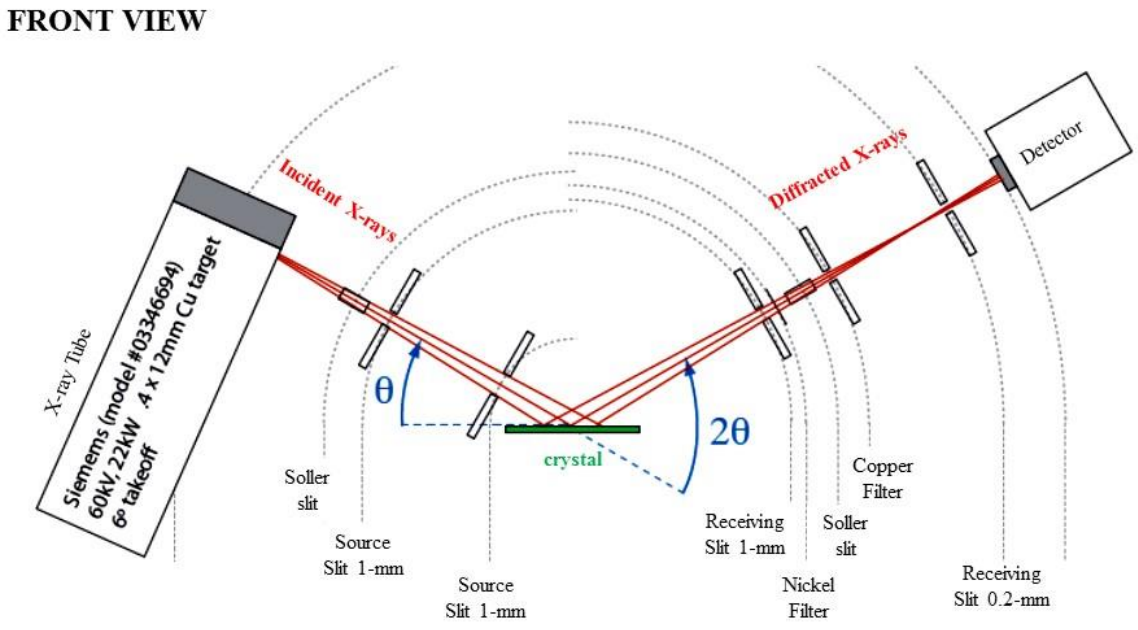

Figure 20 – Front view for diffraction beam path in the D 5000 Diffractometer.

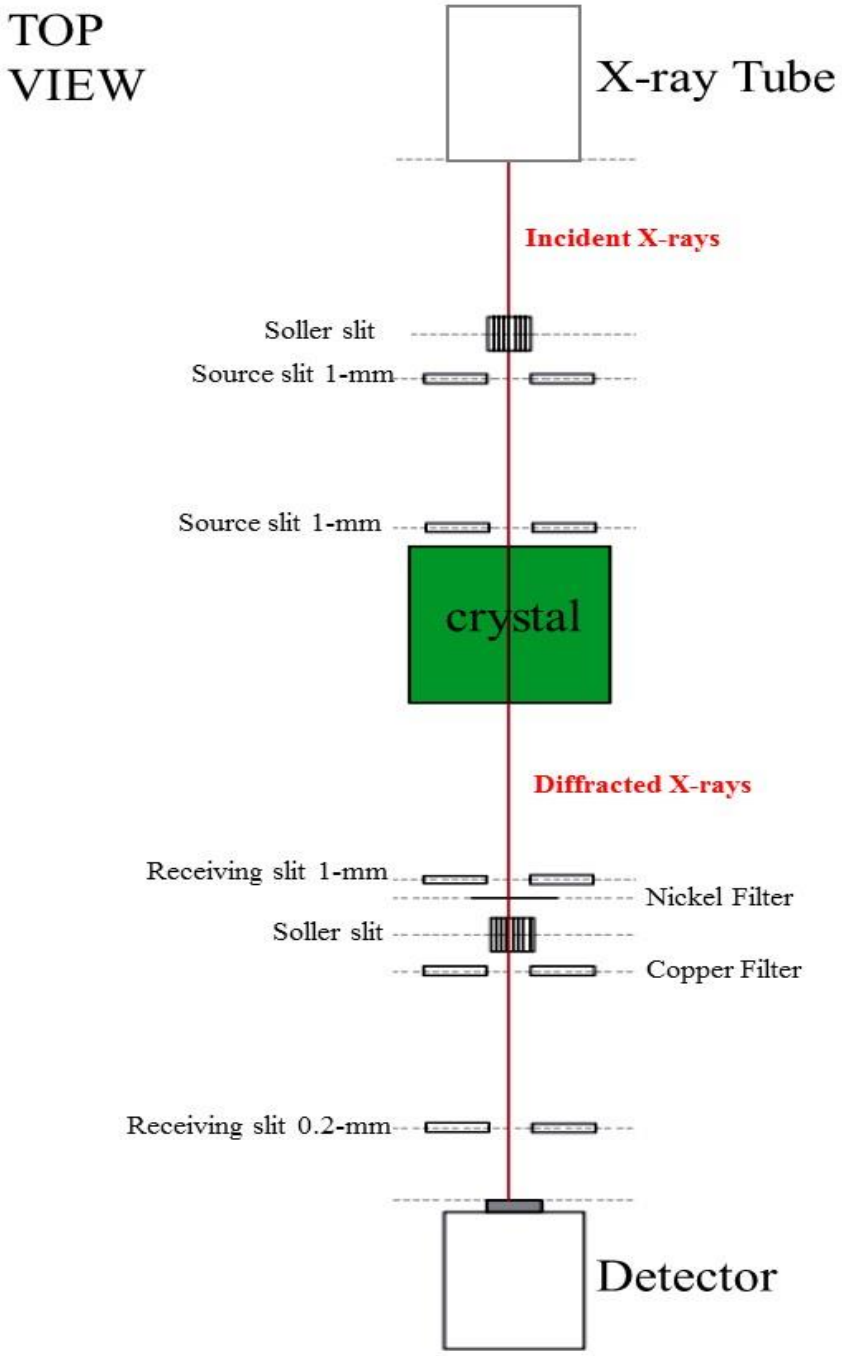

Figure 21 - Top view for diffraction beam path in the D 5000 Diffractometer

Diffrac Plus XRD Commander software controls data collection and *XRD* Wizard software creates specific scanning jobs on a desktop computer. *Diffrac Plus XRD Commander* controls all of the degrees of freedom for the xrd instrument, allowing the

xrd instrument to perform multiple types of scans. A Locked Coupled (LC) scan moves the sample stage and detector through θ and 2θ such that this scan satisfies Bragg's Law ($\theta = ½*2\theta$). An Unlocked Coupled (UC) scan moves the sample stage and the detector through θ and 2θ with an offset where $\theta = ½* 2\theta + offset$. A Rocking Curve (RC) scan moves only the sample stage or the incident-angle (θ) while the other parameters are fixed. A Detector (DT) Scan: moves only the detector-angle (2θ) while all the other parameters are fixed. Chi (χ) scan moves the tilt of the sample around the *y*-axis.
A Phi (φ) scan rotates the whole sample stage around the *z*-axis. An X drive scan: moves the sample motor in the *x*-direction only. Each degree of freedom has limits as shown in Figure 19. Finally, the instrument's software allows the user to combine multiple scans at once to analyze samples.

Experimental Parameters

Depleted UO_2 samples were grown at the RISE Complex using a high precision induction furnace. The induction furnace includes four major parts: furnace chamber, power supply, matching network, and cooling system. The power supply produces high frequency electromagnetic waves, which are transmitted to the matching network. The electromagnetic waves are coupled, through an induction coil, to the given conductive material, in this case a graphite susceptor. The induction furnace requires constant cooling due to very high temperatures (>2000°C) during the growth process. Figure 22 shows heating of non-radioactive material during testing phase in the induction furnace.

Three common crystal growth methods are combined to grow high quality UO_2 crystals: the floating zone method, the modified vertical Bridgman method, and the induction skull melting method. The floating zone method is used to create molten material and push

impurities to the outside edges of the molten zone. The modified vertical Bridgman method is used to move a molten center in the vertical direction throughout the whole material. Finally, the induction skull melting method is used to maintain the outside surface of the sample as a crucible, to keep the molten material confined. Combining all three methods gives great advantages: precise control of temperatures, a non-contact method of heating, the ability to control the atmosphere, the ability to control shape and size of the crystal, small temperature gradient in solid-liquid interface, and non-vacuum or high pressure growth.

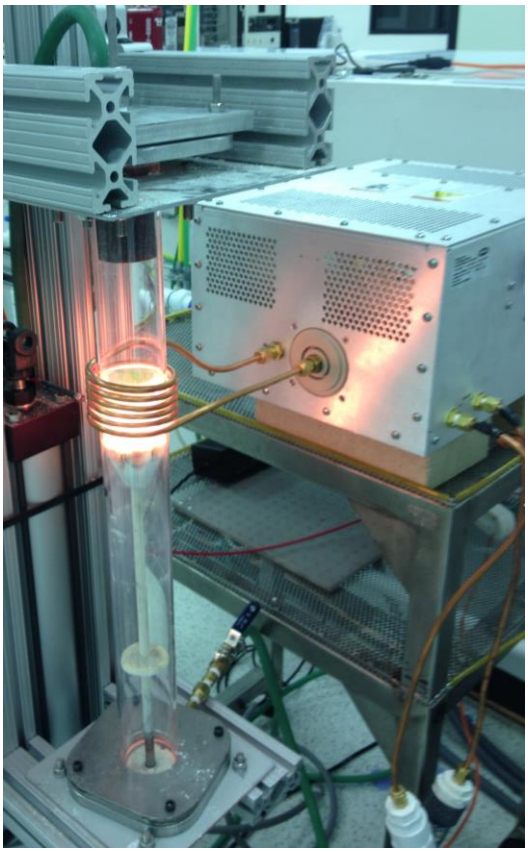

Figure 22 – Induction furnace during testing phase.

To prepare samples for XRD analysis, the product crystals were cut into wafers of 1 mm ±0.25 mm thickness with a precision diamond wire saw. The wire saw, made of stainless steel wire with diamonds embedded into the surface, produces smooth, sharp-edged surfaces on virtually any material.

The sample holder, which goes into the XRD instrument, was made with 3D printer from Makerbot. It is a desktop 3D printer that is very easy to use and has tolerances of ±0.1 mm. Each UO_2 crystal wafer was glued to a plastic wafer, also made with the 3D printer, as shown in Figure 23. After the glue dried, the crystal wafer was leveled with the top surface of the plastic sample holder using a glass microscope slide.

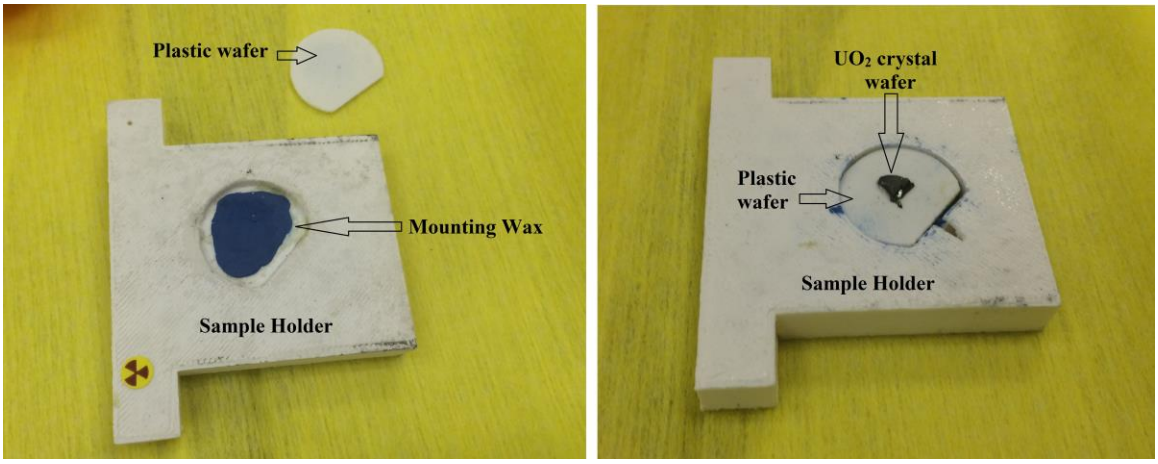

Figure 23 - 3D printed sample holder and insert wafer (left) with UO_2 wafer sample attached (right).

CHAPTER IV: MEASUREMENTS

In order to achieve results that provide useful information about the UO_2 crystal structure, an instrument background calibration had to be performed. The National Institute of Standards and Technology (NIST) has a standard reference material (SRM) for high-resolution x-ray diffraction (HRSRD) calibration. Figure 24 shows the instrumental background for both an LC scan and an RC scan, which gave an average instrumental FWHM of 0.1525°. Since the SRM is a double-polished (100)-oriented silicon (Si) single crystal with only $9x10^{-7}$ nm uncertainty in the *d*-spacing, it will provide diffraction pattern dominated by the instrument background. The certified values for the SRM, which were given for the sample, were used to subtract from the original scans to achieve the average FWHM for the instrument. Measuring the width of the peak at half of the maximum of the intensity for both peaks each from LC and RC scan, and taking an average of both calculates the average FWHM.

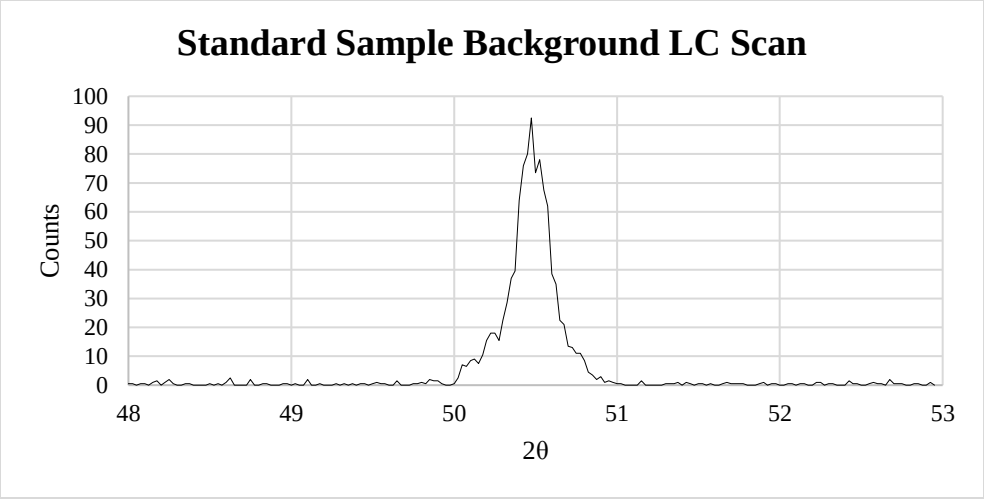

(a)

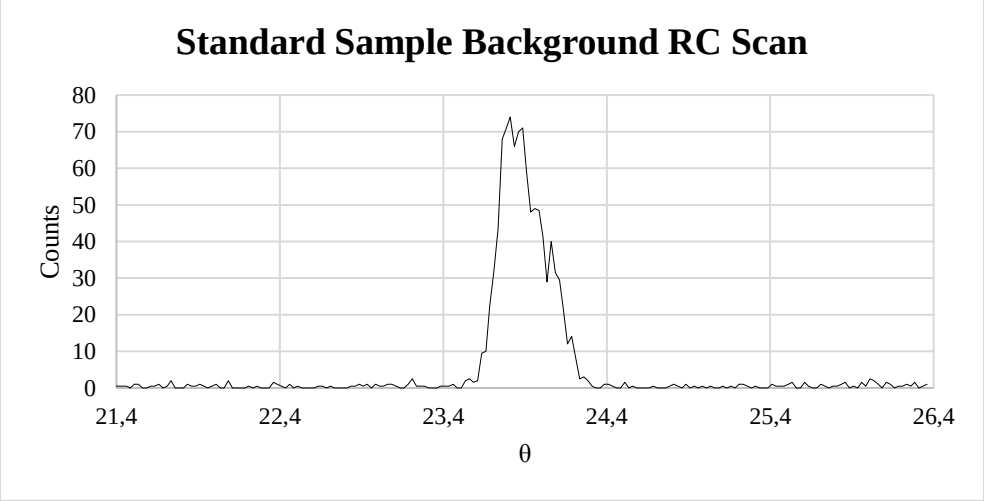

(b)

Figure 24 – Instrumental Background Data using SRM 2000; (a) Locked Couple Scan, (b) Rocking Curve Scan.

By using the nickel filter in the xrd optics, the wavelength (λ) of the x-rays was approximately 0.154 nm. The lattice constant (a) of UO_2 is known as 0.547 nm, where using Equation 1 and Equation 2 together will give 2θ values for each specific plane. As a result, plane (111) had a 2θ value of 28.2° and plane (200) had a 2θ value of 32.7°. Knowing both values for 2θ, the next step was to find the orientation of both planes in the crystal wafers by using a broad scan of ϕ and χ. The broad scans were made more efficient by

increasing the step sizes and lowering the angle ranges in order to take less time for each scan. Therefore, ϕ was set to go from 0º to 359º by 1º steps, and χ was set to go from 0º to 50º by 1º steps with estimated values of θ =14.1°, 2θ = 28.2°, and *x-drive* of 30 mm (middle of the sample holder) for plane (111). Plane (200) scan used estimated values of θ =16.4°, 2θ = 32.7°, and *x-drive* of 30 mm to find distinct peaks at different φ and χ; sample 2 for plane (111) scan is shown in Figure 25. Plane (111) was much easier to find and analyze due to a stronger signal for each crystal wafer compared to plane (200).

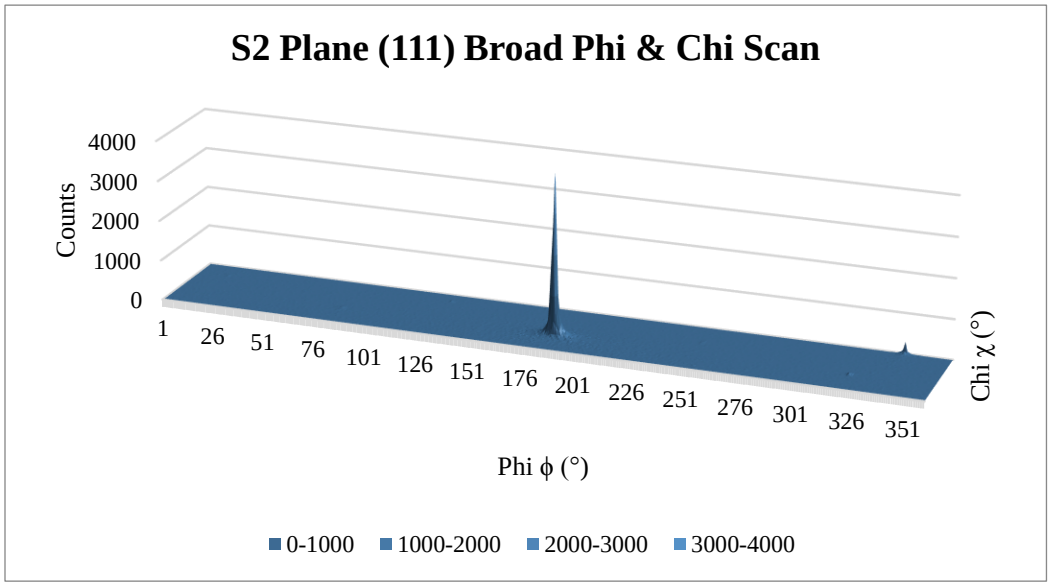

Figure 25 – XRD broad scan for UO_2 crystal sample 2.

Once the orientation of each plane was found by using the broad scans, a more precise scans had to be performed. Coupled scans are used to study lattice mismatch and its parameters. Rocking curves are primarily used to study defects in the crystal structure. Also, introducing new strain into the crystal structure, in this case using an americium-241 source, could show further variations in the lattice mismatch and deformations in the crystalline structure. A total of eight (8) UO_2 wafers were scanned before and after alpha-irradiation, and half of them were scanned twice before alpha-radiation to test the

consistency of the data collection. Once ϕ and χ are found for each sample, more detailed scans are done to find all of the other values for θ, 2θ, χ, ϕ, and *x-drive* by running locked coupled (LC) scans, rocking curve (RC) scans, *x-drive* scan, and phi and chi scans with smaller step sizes.

Figure 26 shows one of the final scans for sample 1 in plane (111) orientation, where 2θ was set to go from 20° to 100° by 0.1° step size at fixed χ and ϕ previously found from the broad scan.

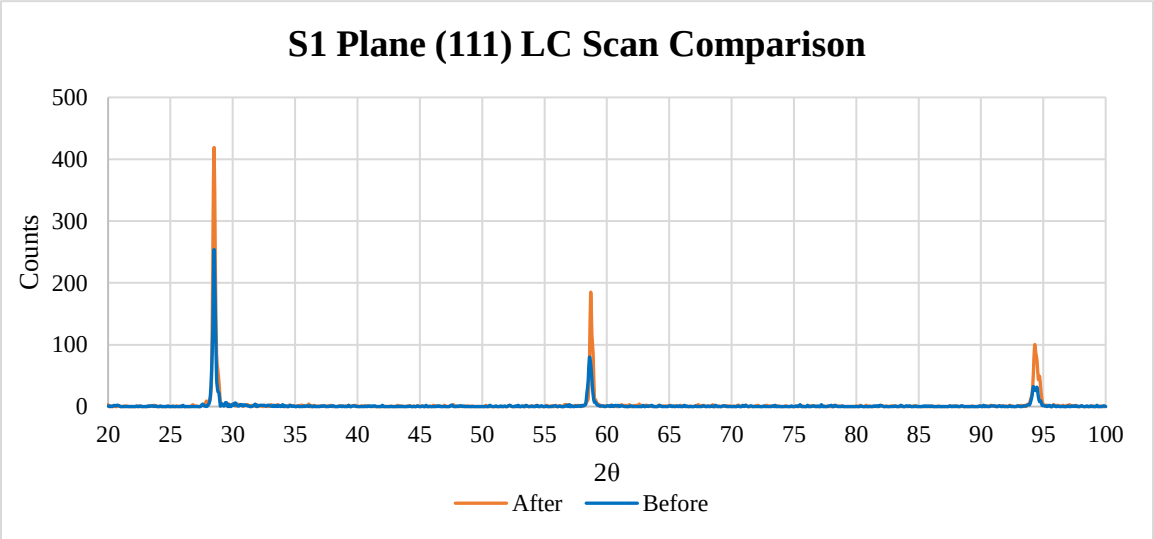

Figure 26 –XRD Locked Coupled Scan for Plane (111) of UO_2 crystal sample 1 before and after irradiation.

Figure 27 shows the final LC scan for sample 1 in plane (111) orientation, where 2θ was set to go from 28° to 29° by 0.001° step size at fixed χ and ϕ previously found from the broad scan. One of the final RC scans is shown in Figure 28, where θ was set to go from 13.5° to 15.5° by 0.001° step size at fixed 2θ, χ and ϕ previously found from the broad scan and LC scan.

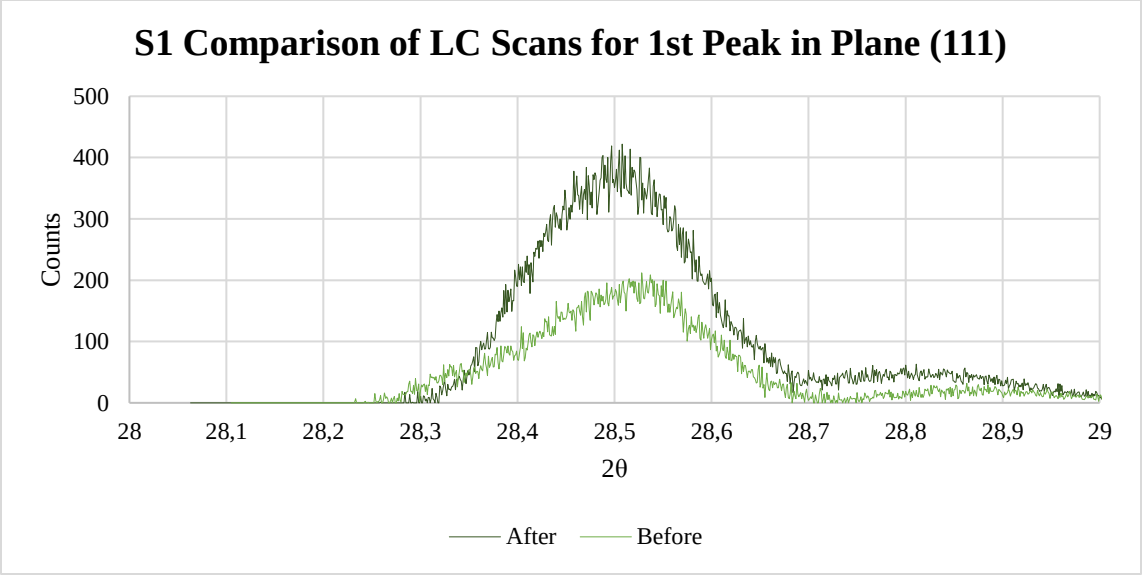

Figure 27 – Sample 1 Before and After Irradiation Locked Coupled Scan for Plane (111).

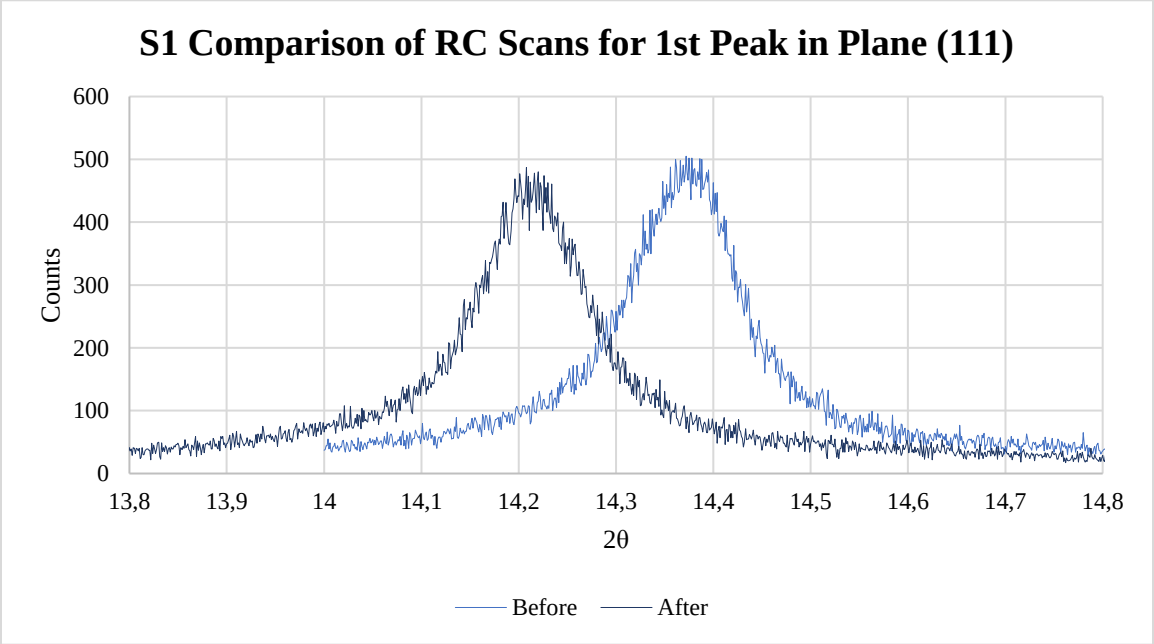

Figure 28 – Sample 1 Before and After Irradiation Rocking Curve Scan for Plane (111).

CHAPTER V: RESULTS

Once all of the measurements were collected, it was necessary to curve fit each diffraction peak for analysis. All of the LC and RC scans measured had a Gaussian fit with at least a 95% coefficient of determination. Equation 7 shows a basic Gaussian function, where *a1* is the amplitude, *b1* is the centroid, and *c1* is related to the peak width. Therefore, Equation 8 shows how the Gaussian *c* constant can be directly related to the FWHM of the peak. Figure 29 shows a sample 1 LC scan and its Gaussian fit function with a coefficient of determination of 97.5%.

$$f(x) = a1e^{-(\frac{(x-b1)}{c1})^2}$$

Equation 7 - Gaussian function

where

f(x) – function of x
x – variable 1
a1, b1, c1 –arbitrary real constants

$$FWHM = 2\sqrt{2\ln 2\, c} \cong 2.35482c$$

Equation 8 – Relationship between Gaussian constant and FWHM of the curve.

where

FWHM – full width at half maximum of the peak
c – arbitrary real constant from Gaussian function

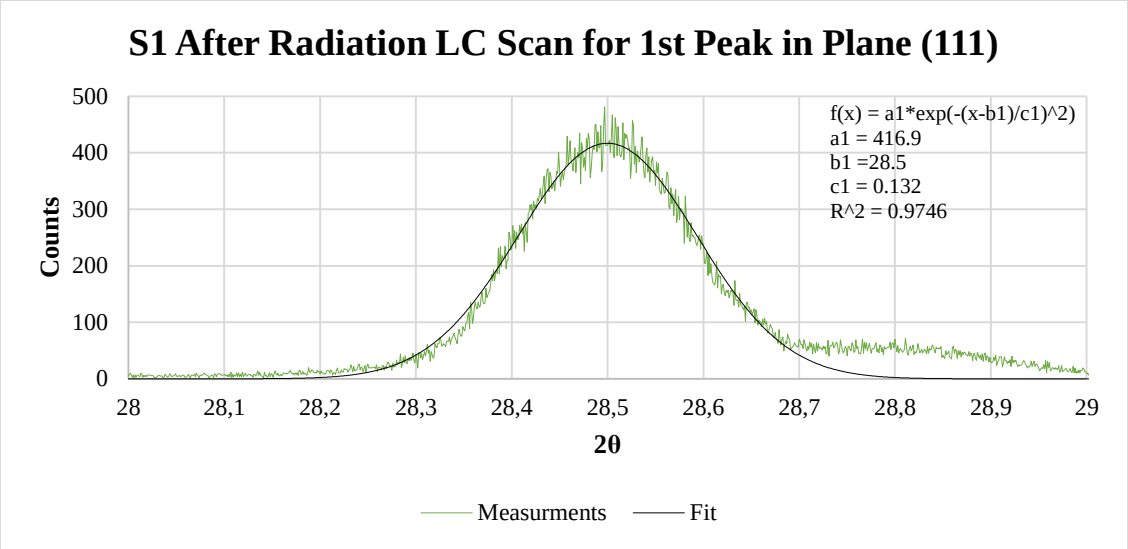

Figure 29 - Sample 1 Locked Couple Scan After Radiation for Plane (111) with Gaussian fit function.

Half of the crystal wafers were scanned twice before alpha-irradiation to test the consistency of the data collection. As a result, Figure 30 shows random shifts in the collected data for the sample 7. The crystal wafers could vary up to ±0.25 mm in thickness across the whole surface and the sample holder's surface could also vary up to ±0.1 mm. Since the xrd instrument has very precise movements, it was able to detect the small variations in the surface of each wafer and sample holder. Simply taking the crystal wafer out of the sample holder and putting it back in generates changes in the data. The rest of the sample scans are shown in Appendix A.

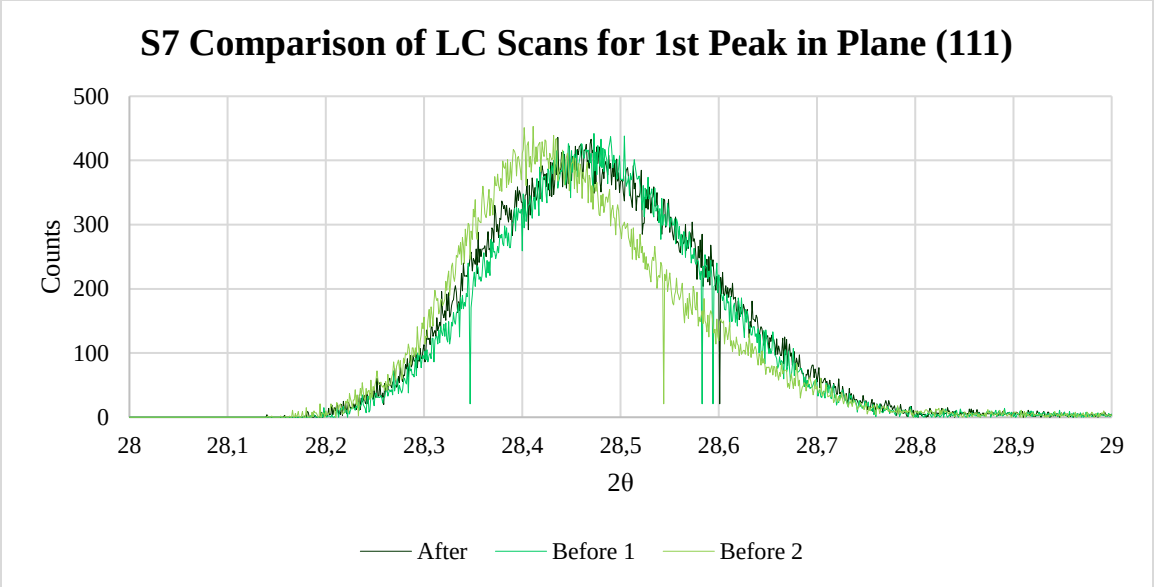

Figure 30 – Sample 7 Before and After Irradiation Locked Coupled Scan for Plane (111).

As mentioned earlier, LC scans are used to study lattice mismatch and its parameters. By measuring the FWHM of the diffraction peak and using its Bragg angle (*θ)* from each LC scan, it was now possible to use Equation 3 to estimate the average crystallite size of each UO_2 wafer. Table 2 shows the estimates of crystallite sizes for both planes, (111) and (200). Since some of the data for plane (200) show sizes bigger than 100 nm, it would be beneficial to also measure the samples with microscopy techniques (SEM or TEM). Also, plane (200) had much weaker signals for the diffraction patterns compared to Plane (111), which showed higher variations in the data set. The biggest size variations were for sample 3 with 78% for plane (111), and sample 4 with 92% for plane (200). By simply removing samples 3 and 4 from the data set, the average percent difference for size estimates dropped to 29% for plane (111) and 53% for plane (200).

Table 2 – Crystallite size estimates for UO_2 samples using LC Scans for:

(a) Plane (111)

Sample	Size Before (nm)	Size After (nm)	Δsize (nm)	Difference %
1	61.60	44.39	17.21	27.9%
2	77.34	46.23	31.11	40.2%
3	80.48	17.99	62.49	77.6%
4	74.98	20.56	54.42	72.6%
5	35.97	32.18	3.79	10.5%
6	59.12	36.96	22.16	37.5%
7	47.70	31.93	15.77	33.1%
8	50.67	38.31	12.36	24.4%
Average	**60.98**	**33.57**	**27.41**	**40.5%**

(b) Plane (200)

Sample	Size Before (nm)	Size After (nm)	Δsize (nm)	Difference %
1	168.83	27.17	141.66	83.9%
2	37.16	44.23	-7.07	19.0%
3	52.58	24.68	27.90	53.1%
4	399.75	32.25	367.50	91.9%
5	26.02	32.73	-6.70	25.8%
6	75.25	36.28	38.97	51.8%
7	314.89	52.14	262.76	83.4%
8	215.91	100.72	115.19	53.3%
Average	**161.30**	**43.77**	**117.52**	**57.8%**

LC scans are also used to calculate the lattice parameters. Earlier in the measurements, the 2θ values were estimated by using the wavelength (λ) of the x-rays as 0.154 nm, and the lattice constant (a) of UO_2 as 0.547 nm. In this case, LC scans were used for measuring 2θ values and going backwards to measure the lattice constant a for each UO_2 wafer. Again, using Equation 1 and Equation 2 with estimated wavelength of 0.154 nm and measured 2θ values for each plane from the LC scans, the lattice constant a was estimated. Table 3 shows results very close to the actual lattice constant of 0.5470 nm

with a maximum variation of only 1.4%. Furthermore, the lattice parameters before and after radiation are consistent with a maximum percent variation of only 0.3%.

Table 3 - *D*-spacing and lattice parameter calculations for UO_2 samples:

(a) Plane (111)

Sample	d-spacing Bef (nm)	d-spacing After (nm)	Lattice "a" Bef (nm)	Lattice "a" After (nm)	Actual "a" (nm)	Diff in "a" Before	Diff in "a" After	Diff in Bef & After "a"
1	0.3125	0.3130	0.5413	0.5421	0.5470	1.04%	0.90%	0.14%
2	0.3126	0.3128	0.5414	0.5418	0.5470	1.02%	0.96%	0.07%
3	0.3121	0.3117	0.5406	0.5398	0.5470	1.16%	1.31%	-0.15%
4	0.3131	0.3122	0.5423	0.5407	0.5470	0.86%	1.15%	-0.30%
5	0.3120	0.3115	0.5405	0.5395	0.5470	1.20%	1.38%	-0.18%
6	0.3124	0.3130	0.5411	0.5421	0.5470	1.08%	0.89%	0.19%
7	0.3131	0.3137	0.5422	0.5433	0.5470	0.87%	0.68%	0.20%
8	0.3118	0.3121	0.5401	0.5406	0.5470	1.27%	1.18%	0.09%
Average	**0.3125**	**0.3125**	**0.5412**	**0.5412**	**0.5470**	**1.06%**	**1.06%**	**0.01%**

(b) Plane (200)

Sample	d-spacing Bef (nm)	d-spacing After (nm)	Lattice "a" Bef (nm)	Lattice "a" After (nm)	Actual "a" (nm)	Diff in "a" Before	Diff in "a" After	"Δa" Before & After
1	0.2698	0.2700	0.5395	0.5400	0.5470	1.36%	1.29%	0.08%
2	0.2702	0.2702	0.5403	0.5404	0.5470	1.22%	1.20%	0.02%
3	0.2707	0.2707	0.5413	0.5413	0.5470	1.04%	1.04%	0.00%
4	0.2707	0.2710	0.5414	0.5419	0.5470	1.03%	0.92%	0.10%
5	0.2698	0.2697	0.5396	0.5394	0.5470	1.35%	1.39%	-0.04%
6	0.2698	0.2702	0.5396	0.5403	0.5470	1.35%	1.22%	0.13%
7	0.2697	0.2704	0.5393	0.5407	0.5470	1.40%	1.15%	0.26%
8	0.2705	0.2710	0.5409	0.5420	0.5470	1.11%	0.92%	0.20%
Average	**0.2701**	**0.2704**	**0.5403**	**0.5408**	**0.5470**	**1.23%**	**1.14%**	**0.09%**

The last set of precise scans measured were the RC scans, which are primarily used to study defects, or strains, in the crystal structure. By measuring the FWHM of the diffraction peak and using its Bragg angle (θ) from each RC scan, it was now possible to use Equation 5 to estimate the uniform strain in each UO_2 wafer. Table 4 shows that the strain estimates are not very consistent across all of the UO_2 samples. Again, plane (200) had much weaker signals in the diffraction patterns compared to plane (111), which showed the biggest variations in the strain estimates. The biggest strain variations are in

sample 3 and 4 for both planes. Sample 3 had 152% strain variation for plane (111) and 439% for plane (200); where sample 4 had 317% for plane (111) and 346% for plane (200). This is due to multiple factors affecting the samples, i.e. inconsistent data collection from the sample holder, temperature factors and low quality or multiple single crystals within the sample. By simply removing samples 3 and 4 from the data set, the average percent difference for strain estimates dropped to 19% for plane (111) and 33% for plane (200).

Table 4 - Strain estimates for UO_2 samples using RC Scans for:

(a) Plane (111)

Sample	Strain Before	Strain After	Δstrain	Difference %
1	0.0019	0.0020	0.0002	9.00%
2	0.0196	0.0176	-0.0019	9.90%
3	0.0029	0.0074	0.0045	152.35%
4	0.0025	0.0106	0.0081	317.14%
5	0.0066	0.0055	-0.0011	16.69%
6	0.0034	0.0044	0.0011	31.26%
7	0.0076	0.0101	0.0025	32.38%
8	0.0080	0.0090	0.0010	12.51%
Average	**0.0066**	**0.0083**	**0.0018**	**72.7%**

(b) Plane (200)

Sample	Strain Before	Strain After	Δstrain	Difference %
1	0.0024	0.0033	0.0009	36.87%
2	0.0105	0.0022	-0.0083	78.81%
3	0.0018	0.0095	0.0078	439.06%
4	0.0034	0.0152	0.0118	345.95%
5	0.0038	0.0051	0.0013	34.69%
6	0.0031	0.0037	0.0006	18.10%
7	0.0019	0.0013	-0.0006	29.53%
8	0.0086	0.0089	0.0002	2.42%
Average	**0.0044**	**0.0061**	**0.0017**	**123.2%**

Finally, another method for estimating size and strain values for each UO_2 sample was done by using the Williamson-Hall method. The method required a plot of $B\cos\theta$ with respect to $\sin\theta$ for multiple data points by using the Bragg angle (θ) and average FWHM (B) from each LC scan for both planes. Since each plane had at least two diffraction peaks (Figure 26) detected, it was possible to plot multiple data points shown in Figure 31. Finding *slope* and *y-intercept* from the plot for each UO_2 sample was necessary to estimate the size and strain values. Using Equation 6 with *slope* and *y-intercept* values from each plot estimated the crystallite size and strain for each UO_2 sample. Table 5 shows the results, which have smaller size values but larger strain values on average than the previous method. Sample 3 had the largest variation in size of 620%, followed by sample 8 with 376%. Sample 4 had the largest strain variation of 4700%, followed by sample 3 with 353%. This could be due to having a limited number of collected data from only two sets of planes, and having weaker signals from the plane (200) with biggest variation in data points shown in Figure 31 (right half of the plot). Therefore, collecting more data for multiple peaks with additional planes would improve the results. By taking sample 3 and 8 away from the size estimates the average percent difference is only 47% (before 159%); and taking sample 3 and 4 away from the strain estimates the average percent difference is only 42% (before 663%).

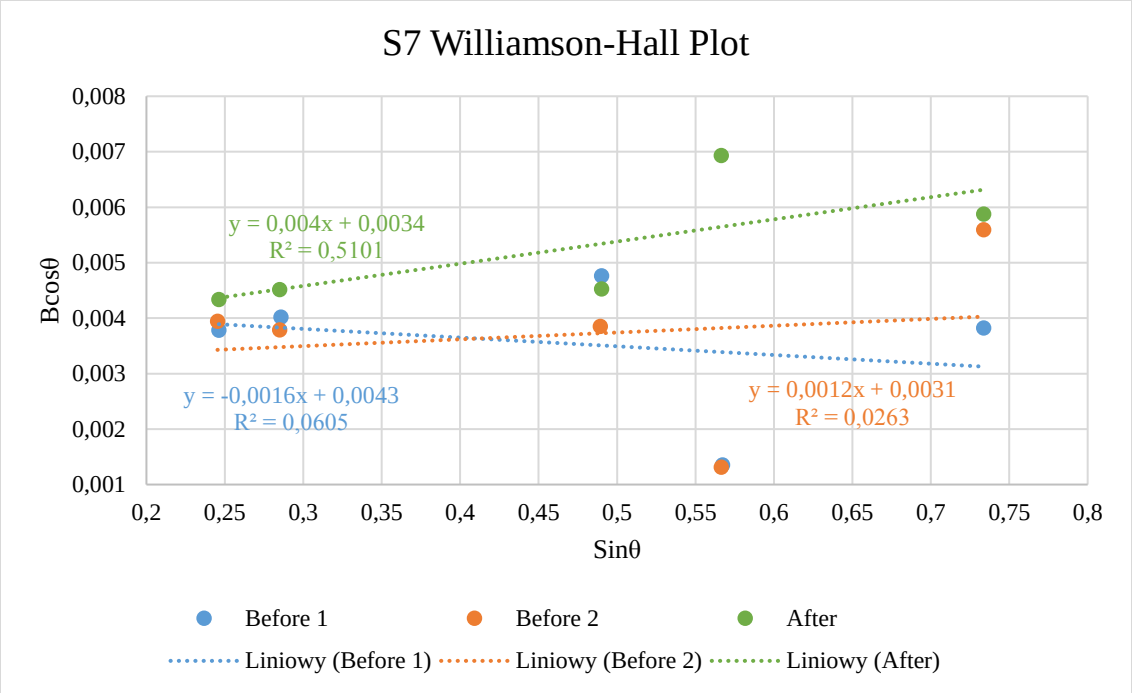

Figure 31 – Williamson-Hall Plot for Sample 7.

Table 5 - Williamson-Hall method results for size and strains for UO_2 samples for:

(a) Size Estimates:

Sample	Size Before (nm)	Size After (nm)	Δsize (nm)	Difference %
1	51.35	69.33	-17.97	35.0%
2	44.73	53.33	-8.60	19.2%
3	19.26	138.65	-119.40	620.0%
4	13.73	24.76	-11.03	80.4%
5	44.73	66.03	-21.30	47.6%
6	53.33	72.98	-19.65	36.8%
7	86.66	34.66	52.00	60.0%
8	2.47	11.75	-9.28	376.3%
Average	**39.53**	**58.94**	**19.40**	**159.4%**

(b) Strain Estimates:

Sample	Strain Before	Strain After	Δstrain	Difference %
1	0.0150	0.0066	-0.0084	56.16%
2	0.0125	0.0080	-0.0045	36.07%
3	0.0031	0.0139	0.0109	353.33%
4	0.0004	0.0197	0.0193	4700.00%
5	0.0141	0.0094	-0.0047	33.33%
6	0.0066	0.0092	0.0027	40.63%
7	0.0088	0.0070	-0.0018	20.93%
8	0.0340	0.0113	-0.0228	66.87%
Average	**0.0118**	**0.0106**	**0.0012**	**663.4%**

CHAPTER VI: CONCLUSION

This study showed that the UO_2 crystals grown at the RISE complex have single crystal components with less than 2% variation in lattice constant. However, the induced strains and the sizes of the single crystals are very inconsistent across all of the samples. Furthermore, the design of the sample holder needs improvement to allow for more consistent data collection of the UO_2 samples. Collecting more XRD data with other diffraction peaks and planes could give a better understanding of the induced strains in the samples. Both methods for calculating size and strains of single crystals showed that samples 3, 4 and 8 were very inconsistent compared to all the other samples. The xrd instrument is capable of deriving a lot of information about crystal structures; however, it would be beneficial to combine that information with SEM and TEM results as well.

REFERENCES

[1] Fultz, B., & Howe, J. M. (2013). Diffraction and the X-Ray Powder Diffractometer. *Transmission Electron Microscopy and Diffractometry of Materials*, 1-59. doi:10.1007/978-3-540-73886-2_1

[2] Sardela, M. (2008). 2008 Advanced Materials Characterization Workshop. Retrieved April 21, 2016, from https://mrl.illinois.edu/sites/default/files/pdfs/Workshop08_X-ray_Handouts.pdf

[3] Cullity, B. D., & Stock, S. R. (2001). *Elements of x-ray diffraction*. Upper Saddle River, NJ: Prentice Hall.

[4] Murty, K. L., & Charit, I. (2013). *An introduction to nuclear materials: Fundamentals and applications*. Weinheim, Germany: Wiley-VCH.

[5] "Lattice Constant | Wikiwand." *Wikiwand*. N.p., n.d. Web. 06 June 2016. <http://www.wikiwand.com/en/Lattice_constant>.

[6] "Symmetry, Crystal Systems and Bravais Lattices." *Home*. N.p., n.d. Web. 06 June 2016. <http://www.physics-in-a-nutshell.com/article/6>.

[7] "Homework - Crystallography - SOLUTIONS." *Homework - Crystallography - SOLUTIONS*. N.p., n.d. Web. 06 June 2016. <http://fog.ccsf.cc.ca.us/~wkaufmyn/ENGN45/ENGN45_Online_Homework/03_Homework_Crystallography_SOLUTIONS.htm>.

[8] *Crystallography and Diffraction Techniques*. (2016, April 18). Reading.

[9] Cheary, R. W., Coelho, A. A., & Cline, J. P. (2004, January/February). Fundamental Parameters Line Profile Fitting in Laboratory Diffractometers. Retrieved April 15, 2016, from http://nvlpubs.nist.gov/nistpubs/jres/109/1/j91che.pdf

[10] Duncan, Martin. "File:Peak Strain.png." *Mediawiki*. N.p., 15 Feb. 2015. Web. 6 June 2016. <http://129.89.58.197/mediawiki/index.php/File:Peak_strain.png>.

[11] "Crystallite Size and Strain." Accessed May 8, 2016. http://pd.chem.ucl.ac.uk/pdnn/peaks/size.htm

[12] SIEMENS (Comp.). (2014). D 5000 Diffractometer Manual.

[13] Weaver, M. L. (n.d.). *Class 17 - X-ray Diffraction*. Lecture. Retrieved April 14, 2016, from http://bama.ua.edu/~mweaver/courses/MTE583/MTE 583_Class_17.pdf

Appendix A

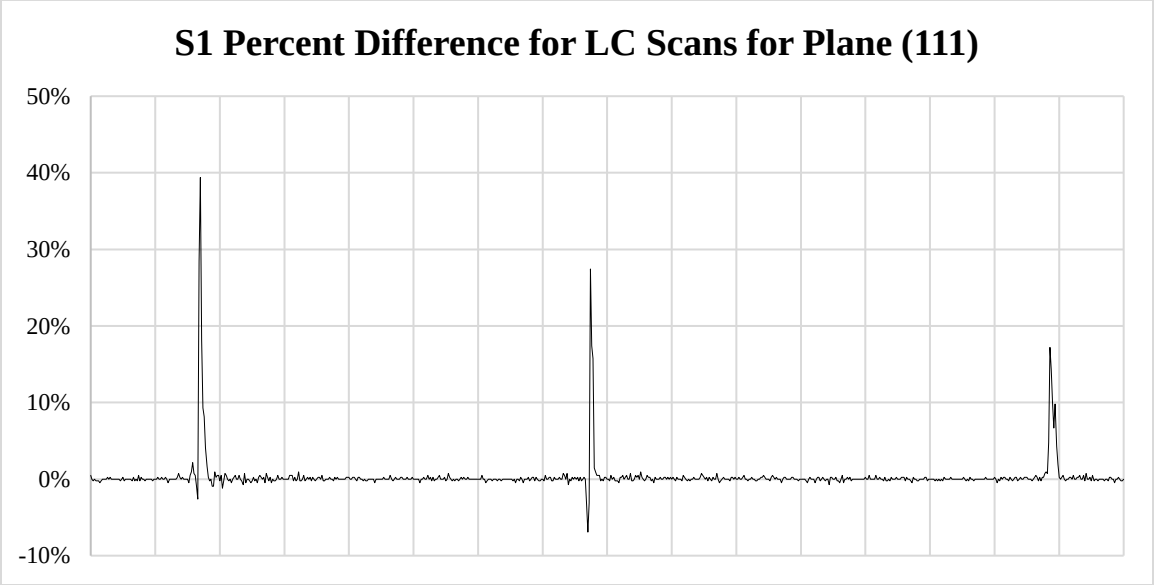

Figure 32 – Percent Difference for XRD Locked Coupled Scan for Plane (111) of UO_2 crystal sample 1 before and after irradiation.

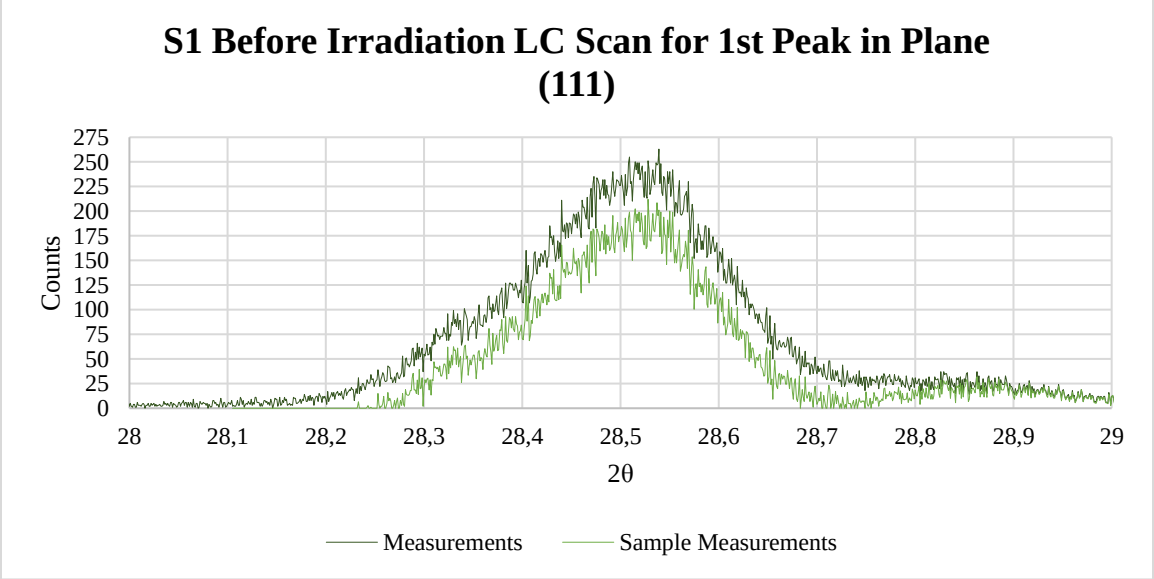

Figure 33 – Sample 1 Locked Coupled Scan Before Radiation for Plane (111) with Instrumental Background Adjustment.

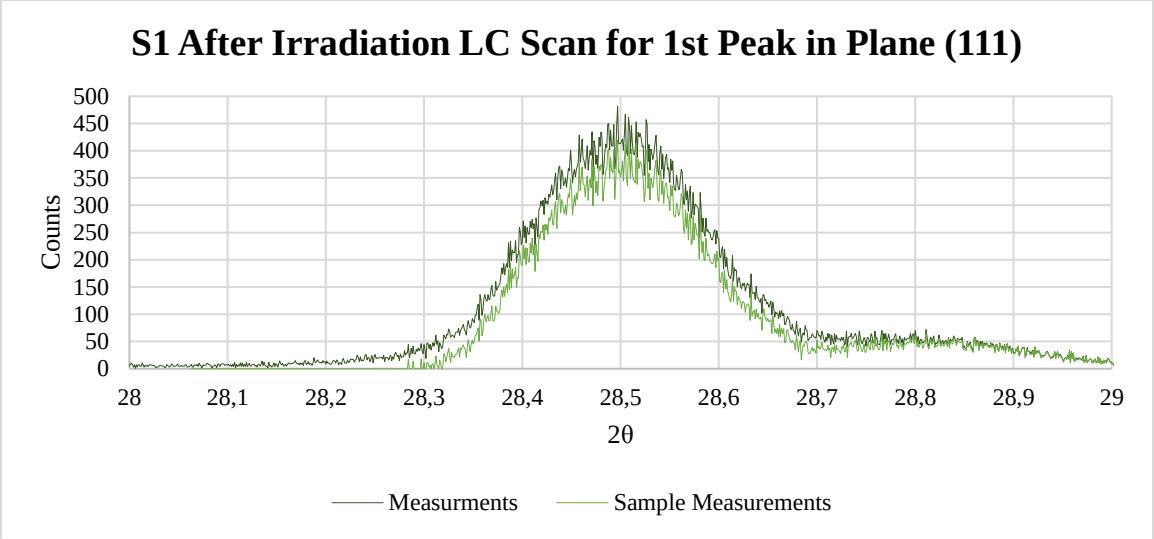

Figure 34 – Sample 1 Locked Coupled Scan After Radiation for Plane (111) with Instrumental Background Adjustment.

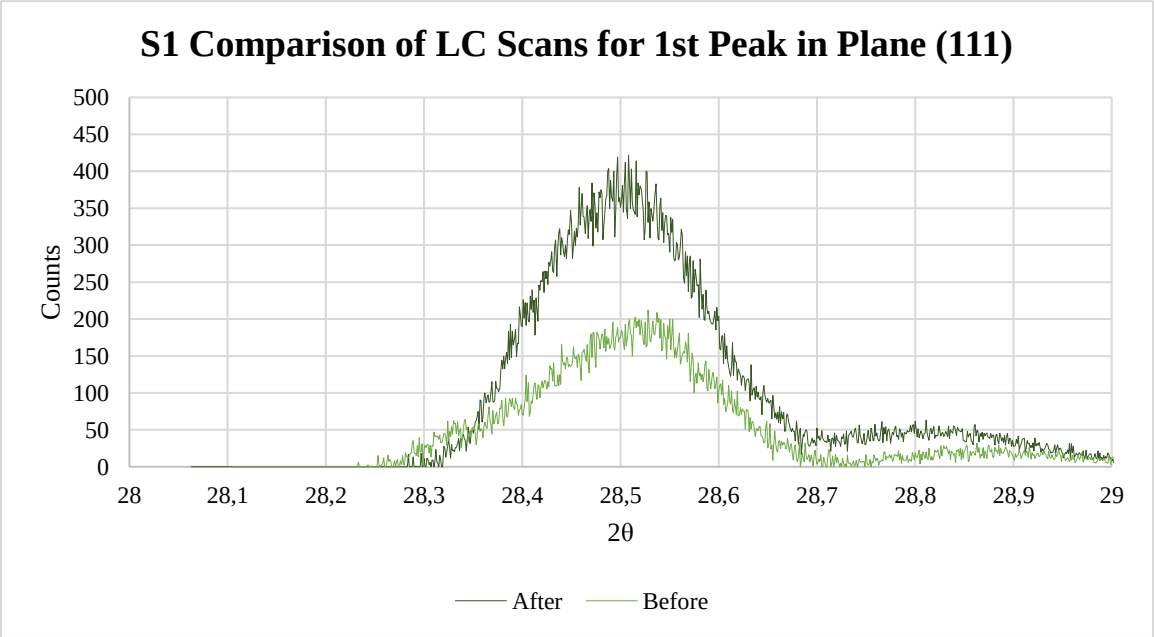

Figure 35 – Sample 1 Before and After Irradiation Locked Coupled Scan for Plane (111).

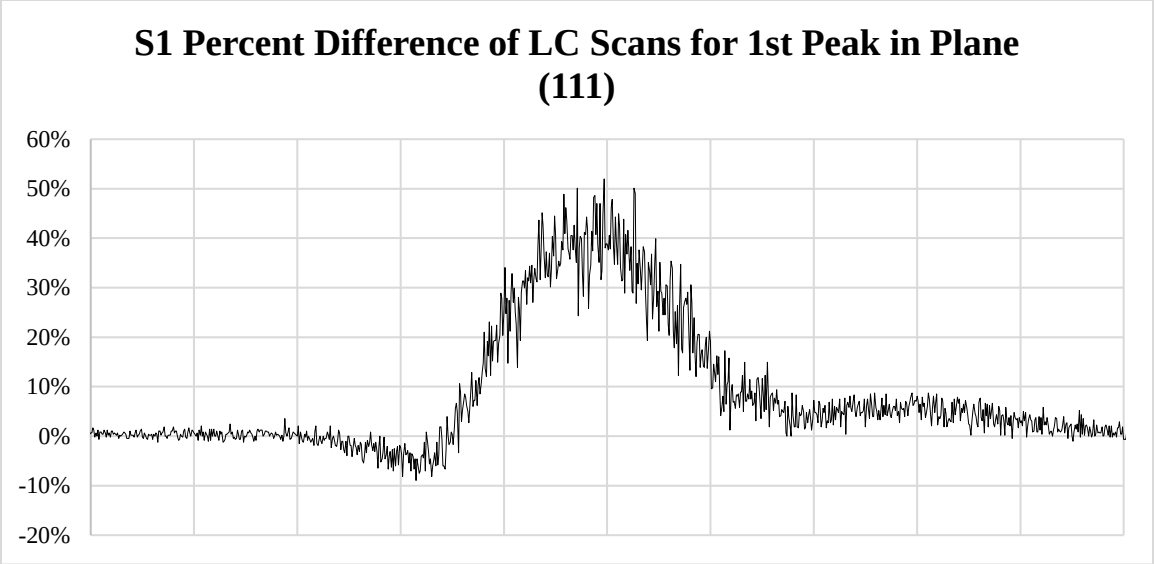

Figure 36 – Percent Difference for Sample 1 Before and After Irradiation Locked Coupled Scans for Plane (111).

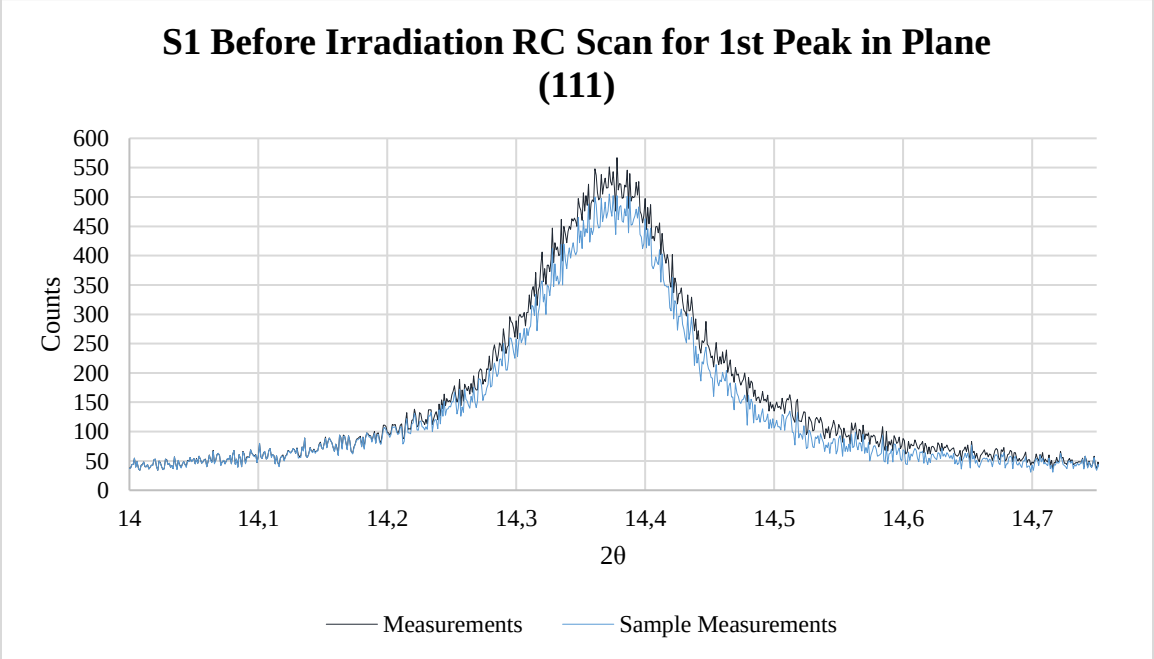

Figure 37 – Sample 1 Before Irradiation Rocking Curve Scan for Plane (111) with Instrumental Background Adjustment.

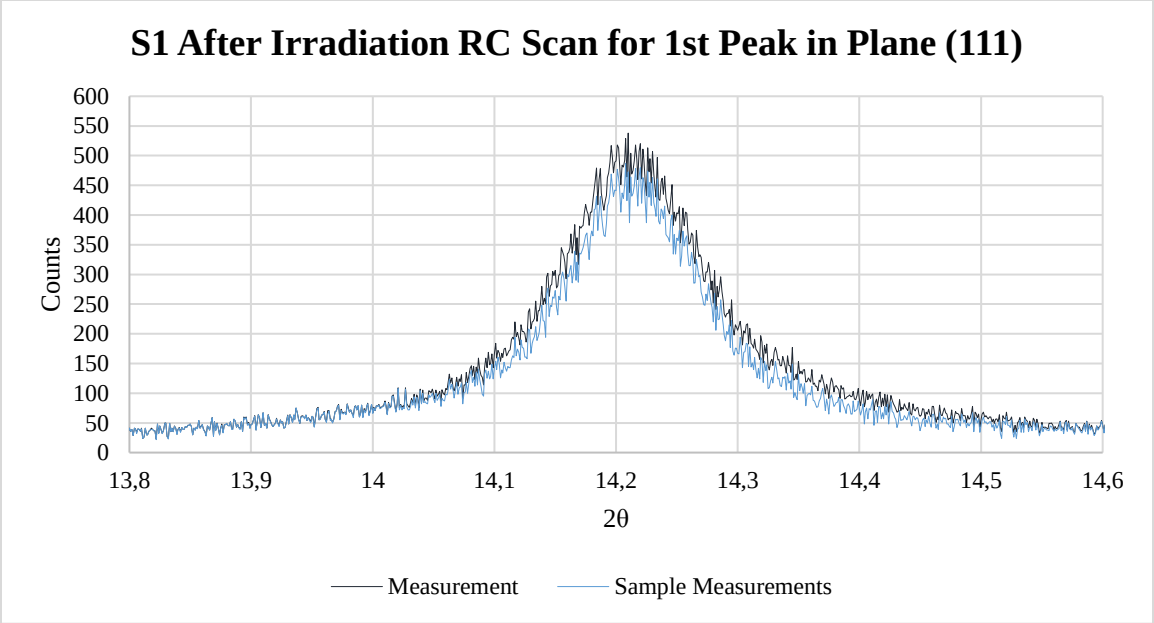

Figure 38 – Sample 1 After Irradiation Rocking Curve Scan for Plane (111) with Instrumental Background Adjustment.

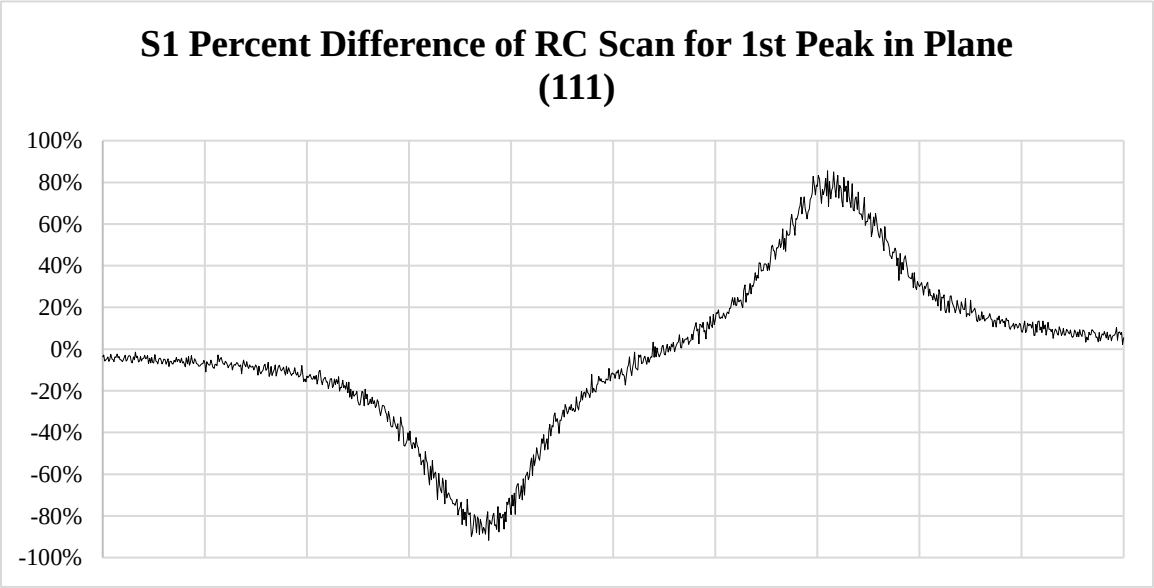

Figure 39 – Percent Difference for Sample 1 Before and After Irradiation Rocking Curve Scans for Plane (111).

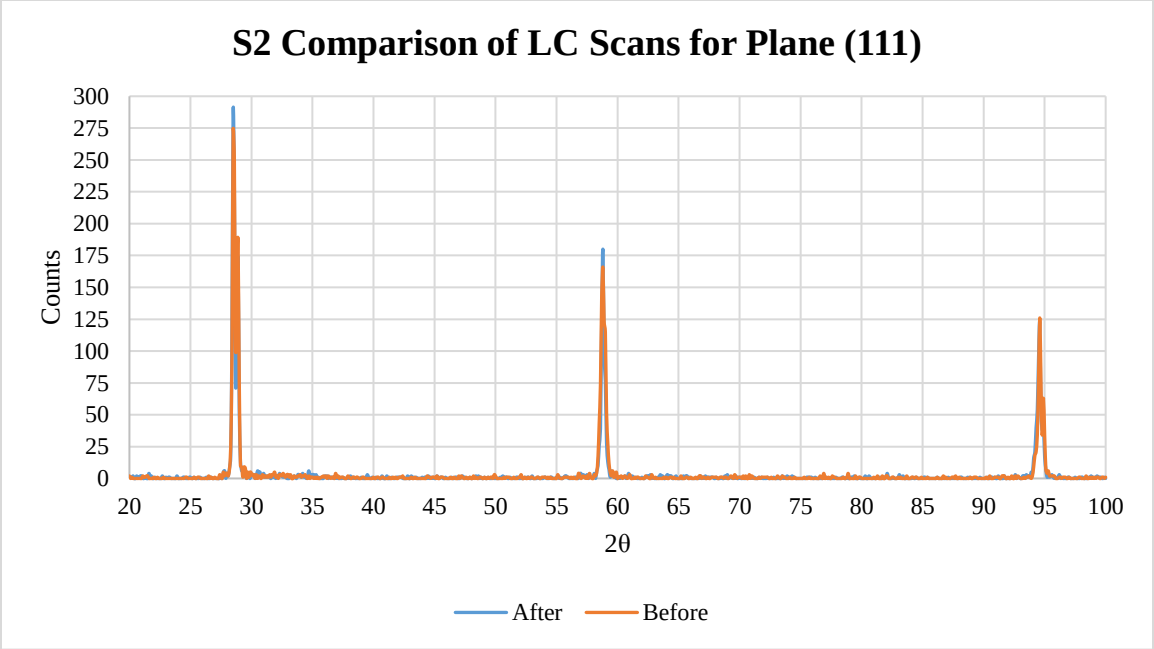

Figure 40 – XRD Locked Coupled Scan for Plane (111) of UO_2 crystal sample 2 before and after irradiation.

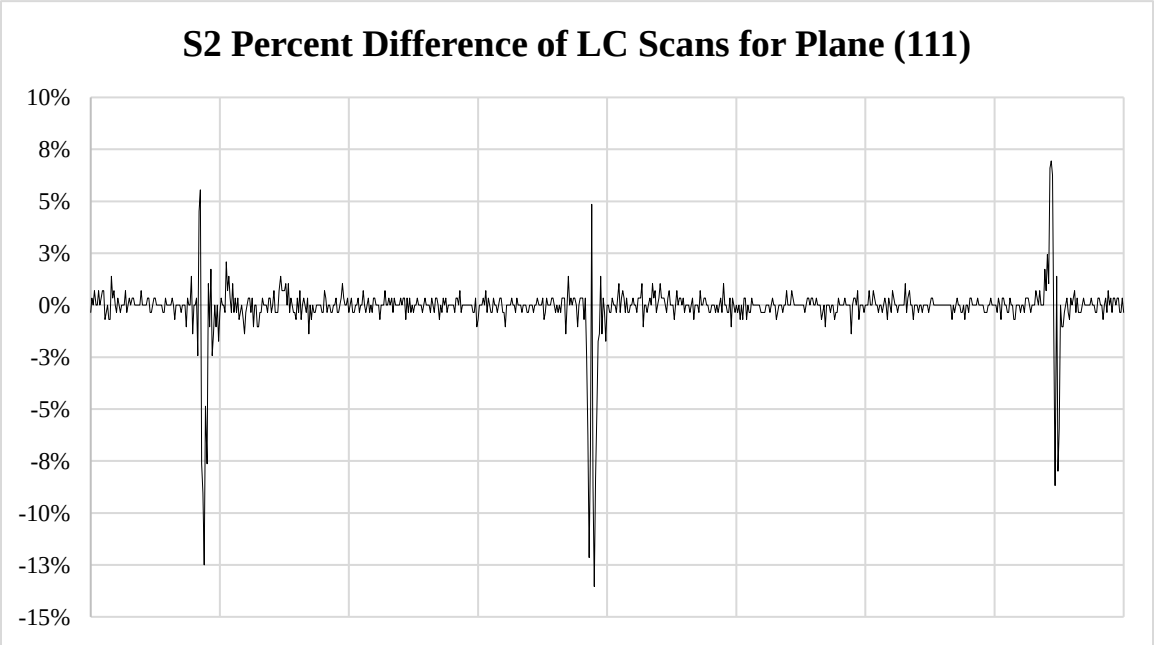

Figure 41 – Percent Difference for XRD Locked Coupled Scan for Plane (111) of UO_2 crystal sample 2 before and after irradiation.

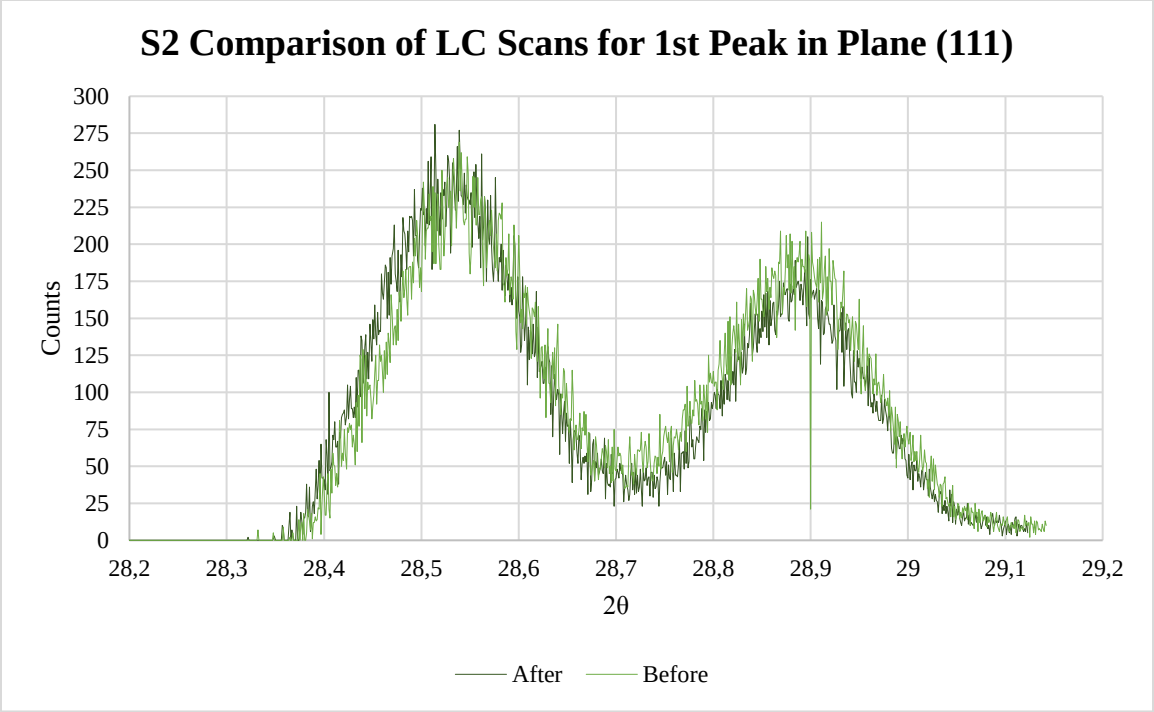

Figure 42 – Sample 2 Before and After Irradiation Locked Coupled Scan for Plane (111).

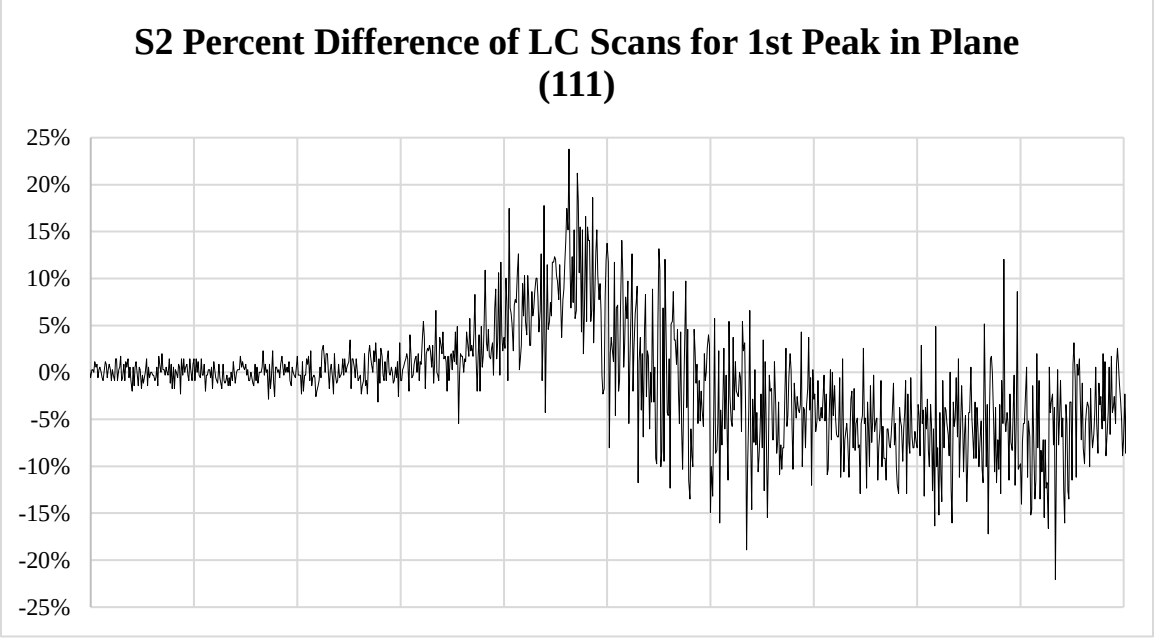

Figure 43 – Percent Difference for Sample 2 Before and After Irradiation Locked Coupled Scan for Plane (111).

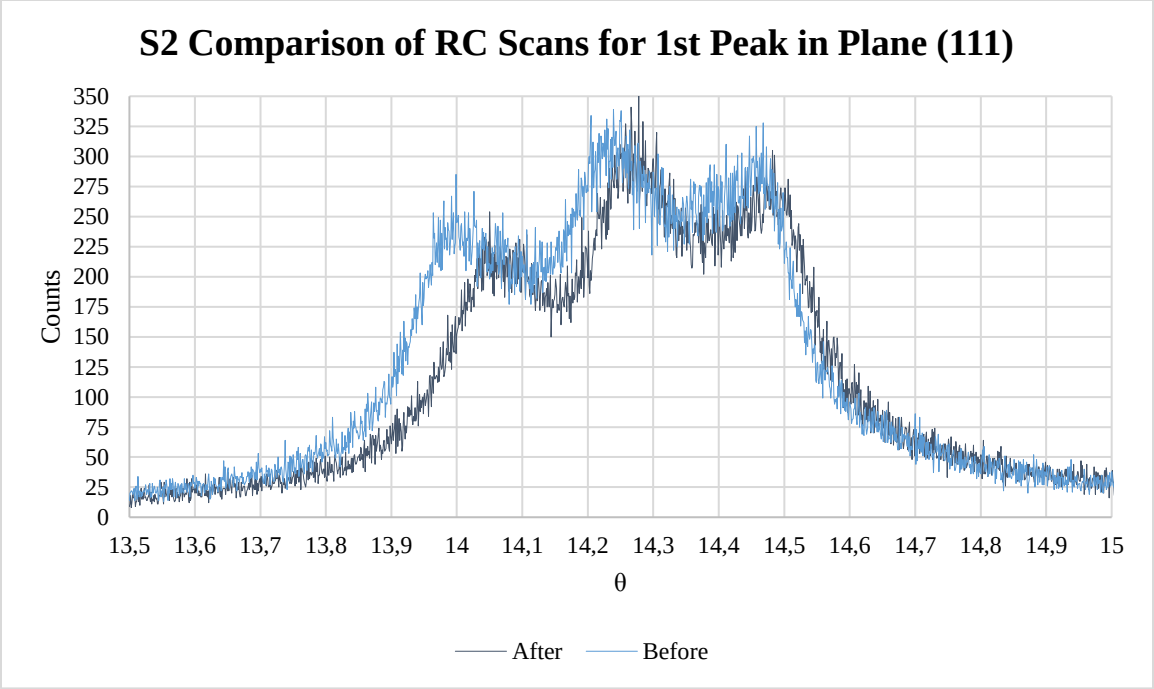

Figure 44 – Sample 2 Before and After Irradiation Rocking Curve Scan for Plane (111).

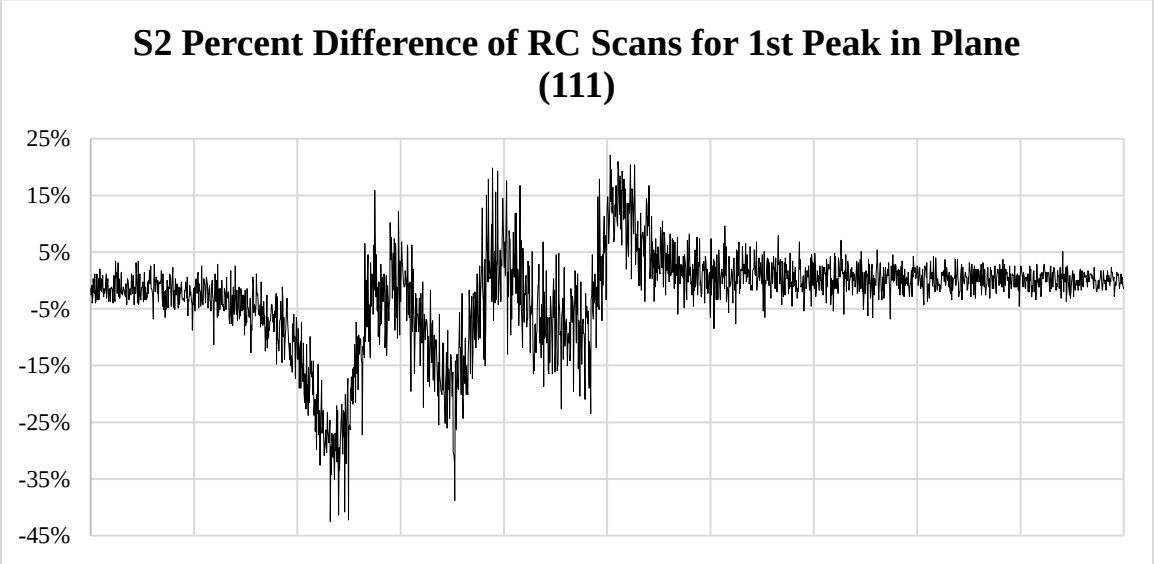

Figure 45 – Percent Difference for Sample 2 Before and After Irradiation Rocking Curve Scan for Plane (111).

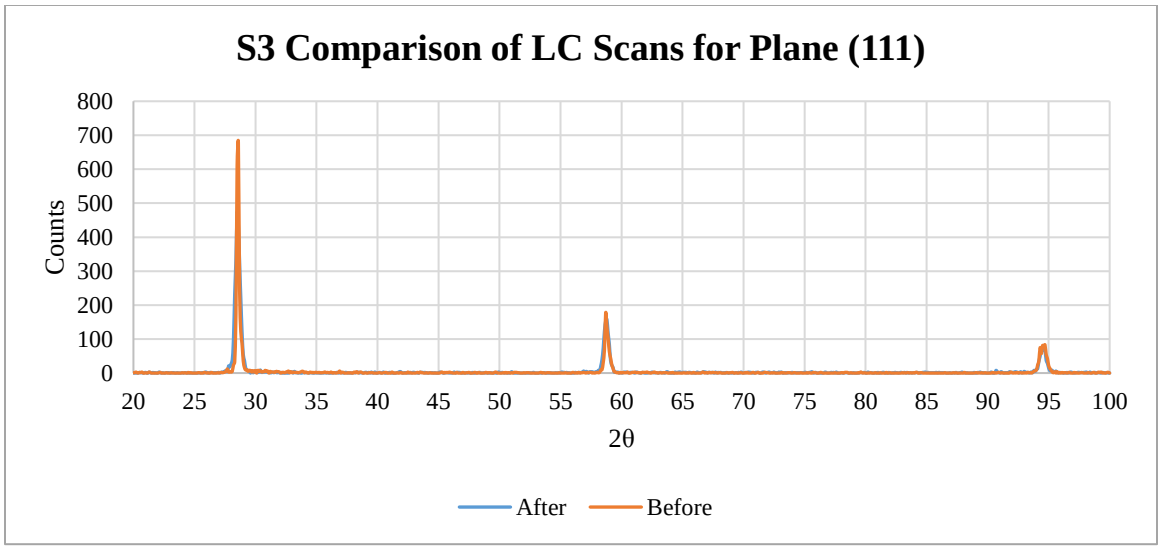

Figure 46 – XRD Locked Coupled Scan for Plane (111) of UO_2 crystal sample 3 before and after irradiation.

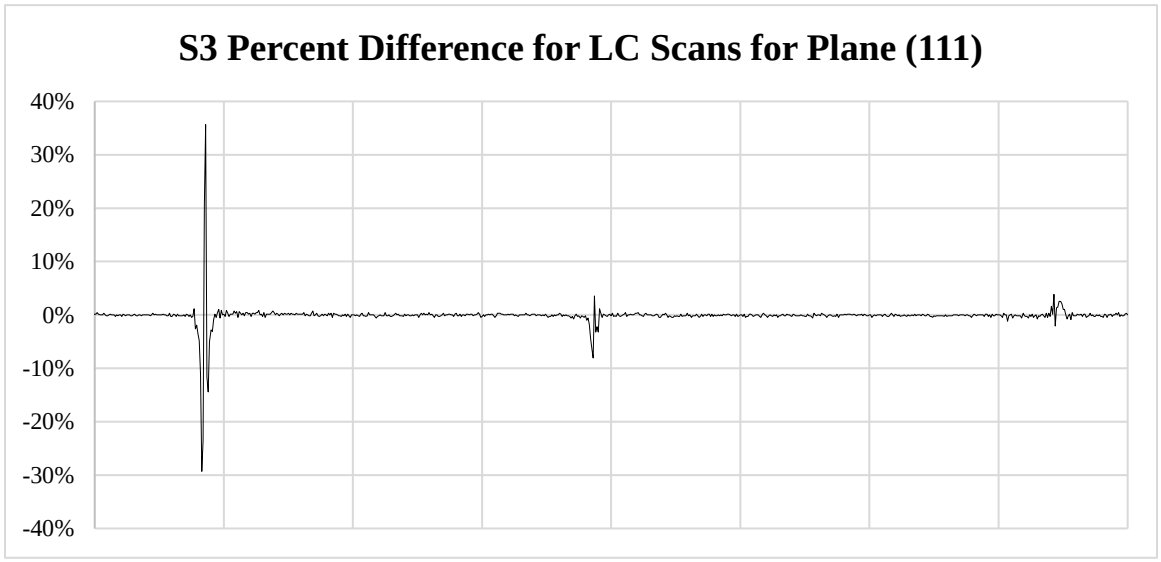

Figure 47 – Percent Difference for XRD Locked Coupled Scan for Plane (111) of UO_2 crystal sample 3 before and after irradiation.

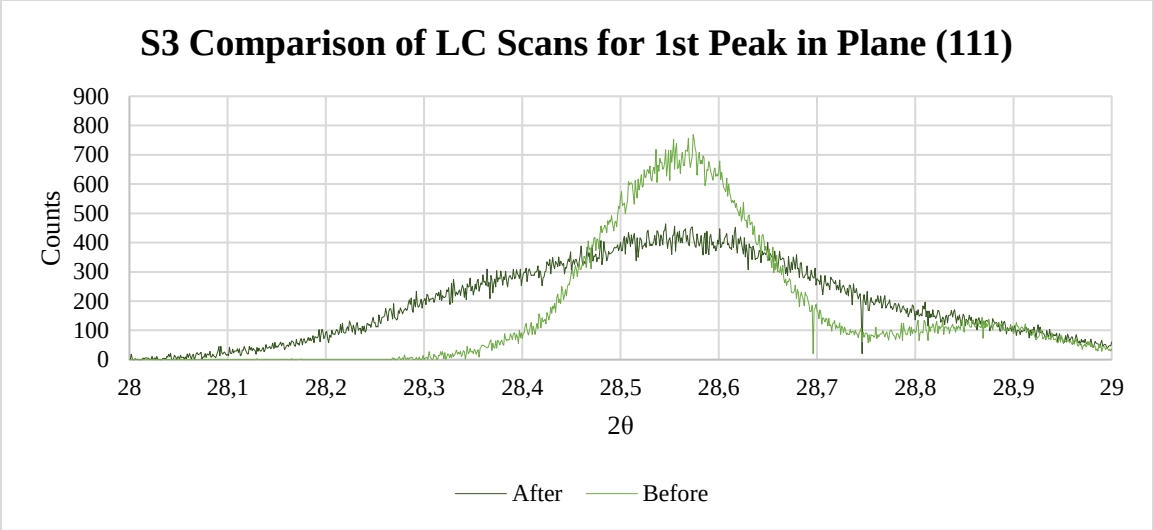

Figure 48 – Sample 3 Before and After Irradiation Locked Coupled Scan for Plane (111).

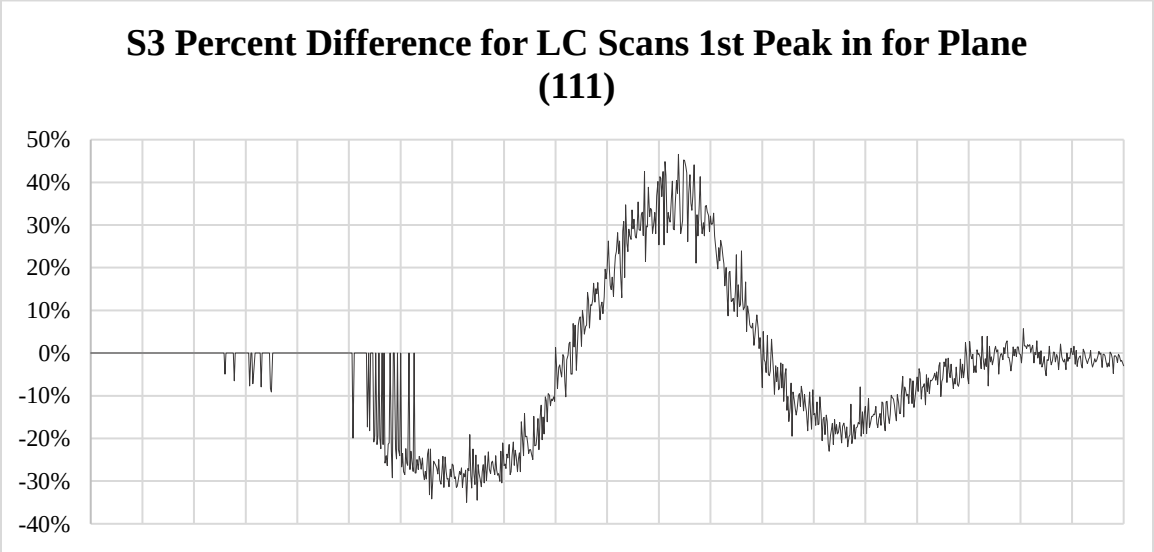

Figure 49 – Percent Difference for Sample 3 Before and After Irradiation Locked Coupled Scan for Plane (111).

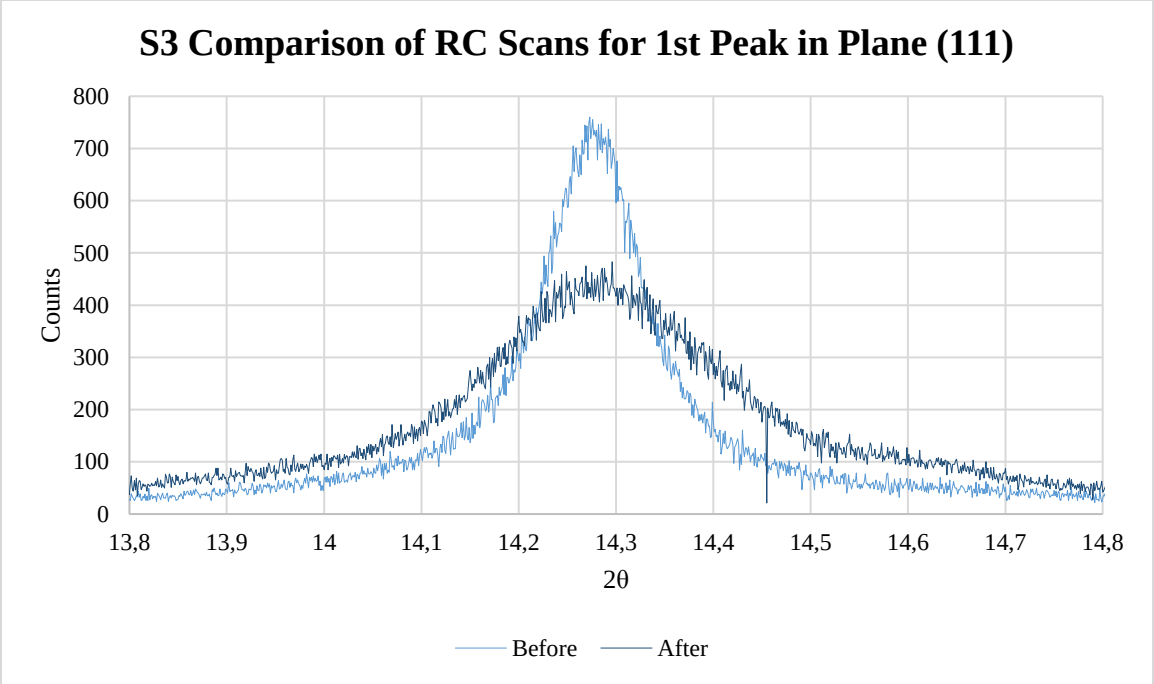

Figure 50 – Sample 3 Before and After Irradiation Rocking Curve Scan for Plane (111).

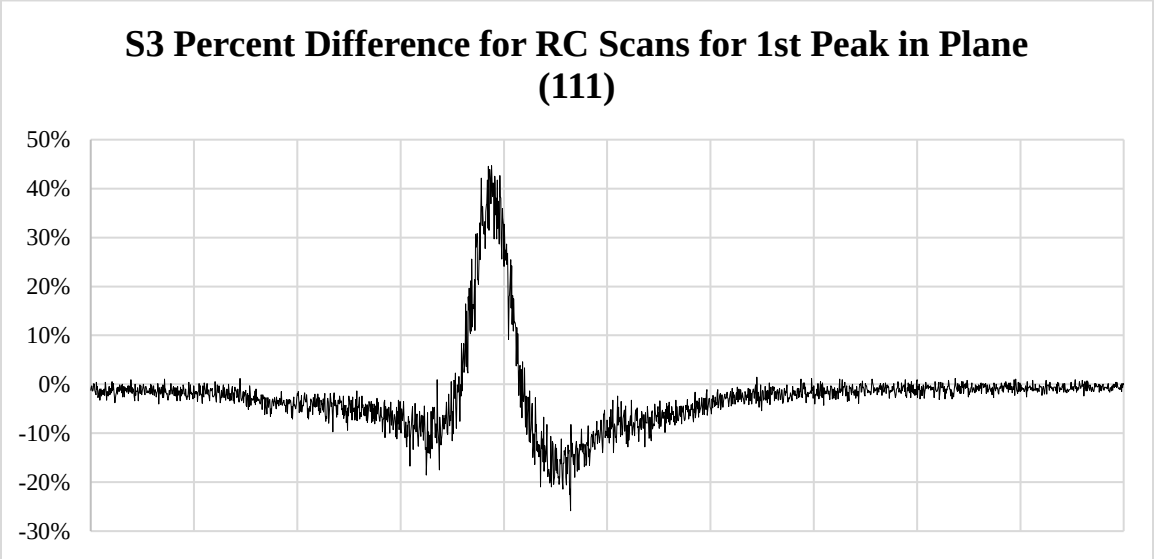

Figure 51 – Percent Difference for Sample 3 Before and After Irradiation Rocking Curve Scan for Plane (111).

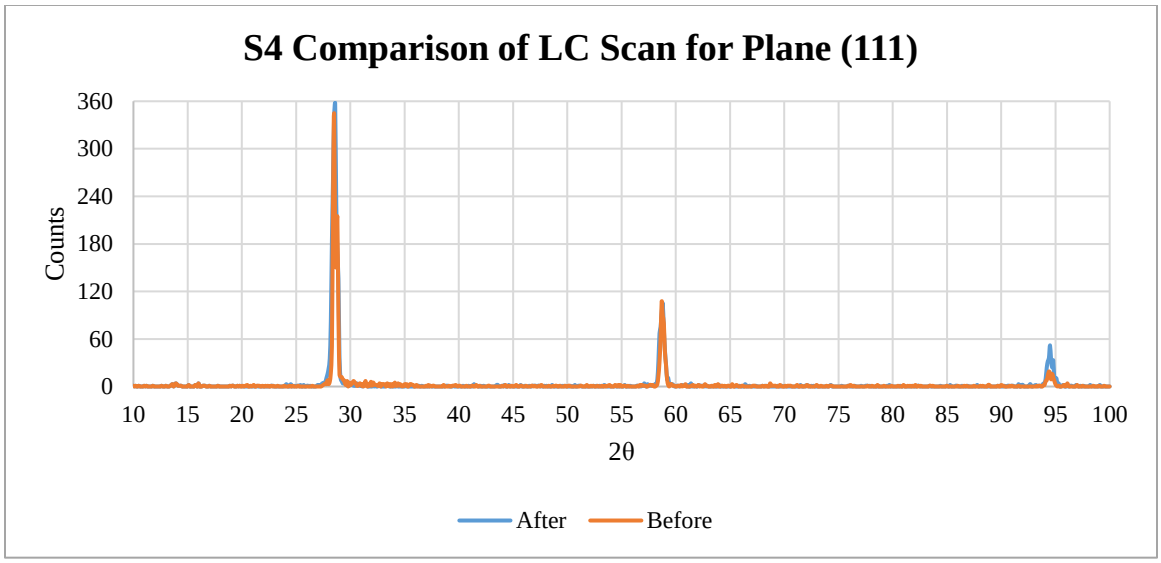

Figure 52 - XRD Locked Coupled Scan for Plane (111) of UO_2 crystal sample 4 before and after irradiation.

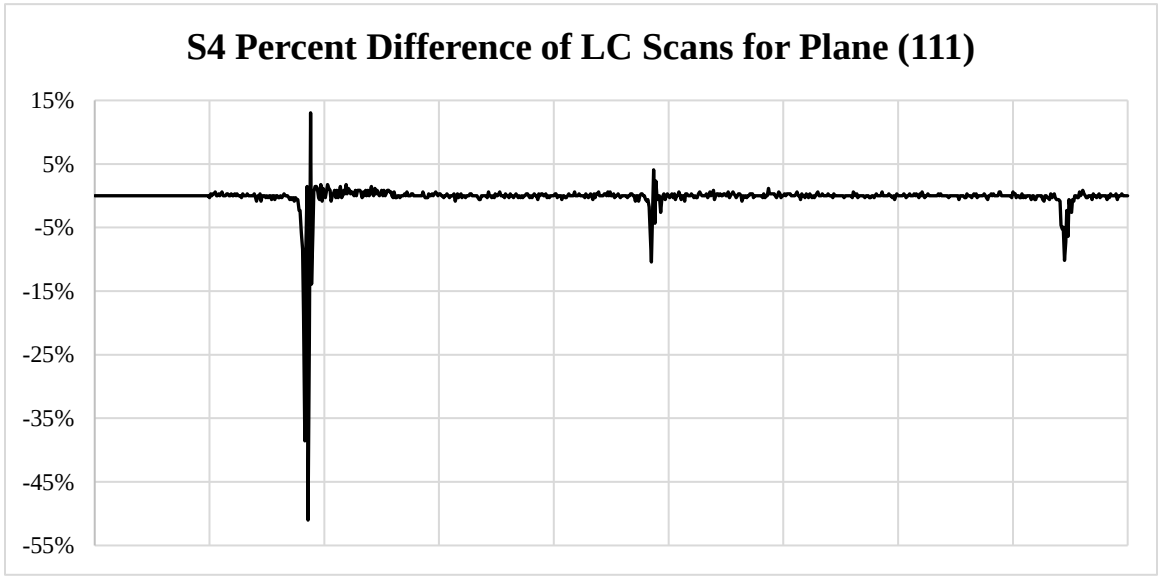

Figure 53 – Percent Difference for XRD Locked Coupled Scan for Plane (111) of UO_2 crystal sample 4 before and after irradiation.

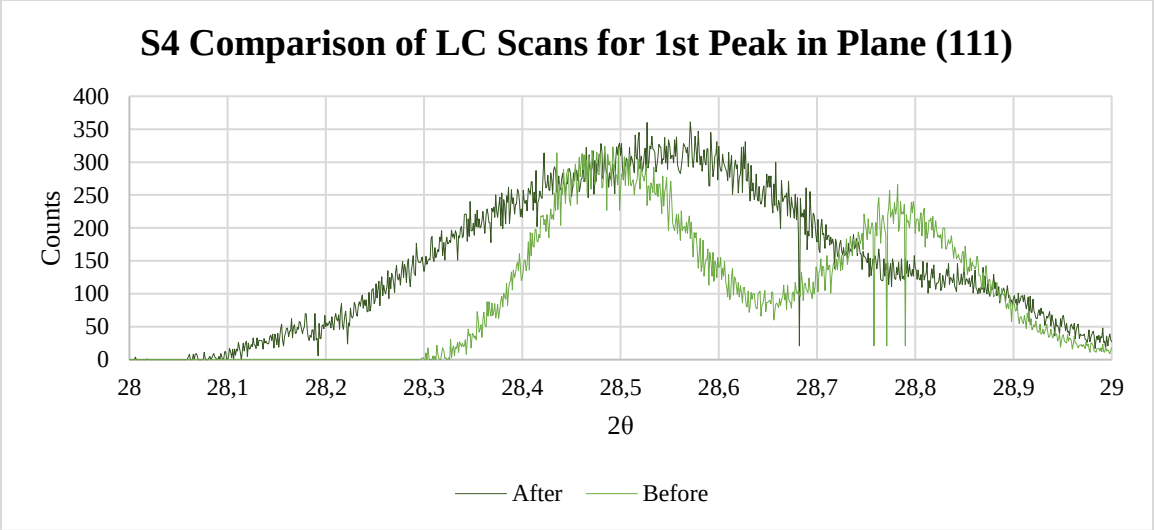

Figure 54 – Sample 4 Before and After Irradiation Locked Coupled Scan for Plane (111).

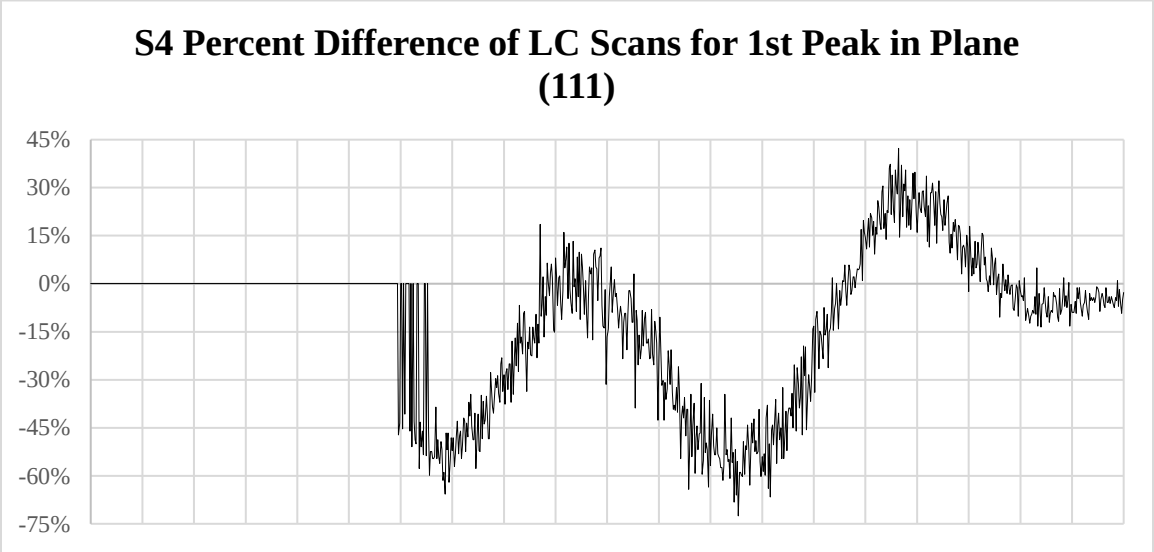

Figure 55 – Percent Difference for Sample 4 Before and After Irradiation Rocking Curve Scan for Plane (111).

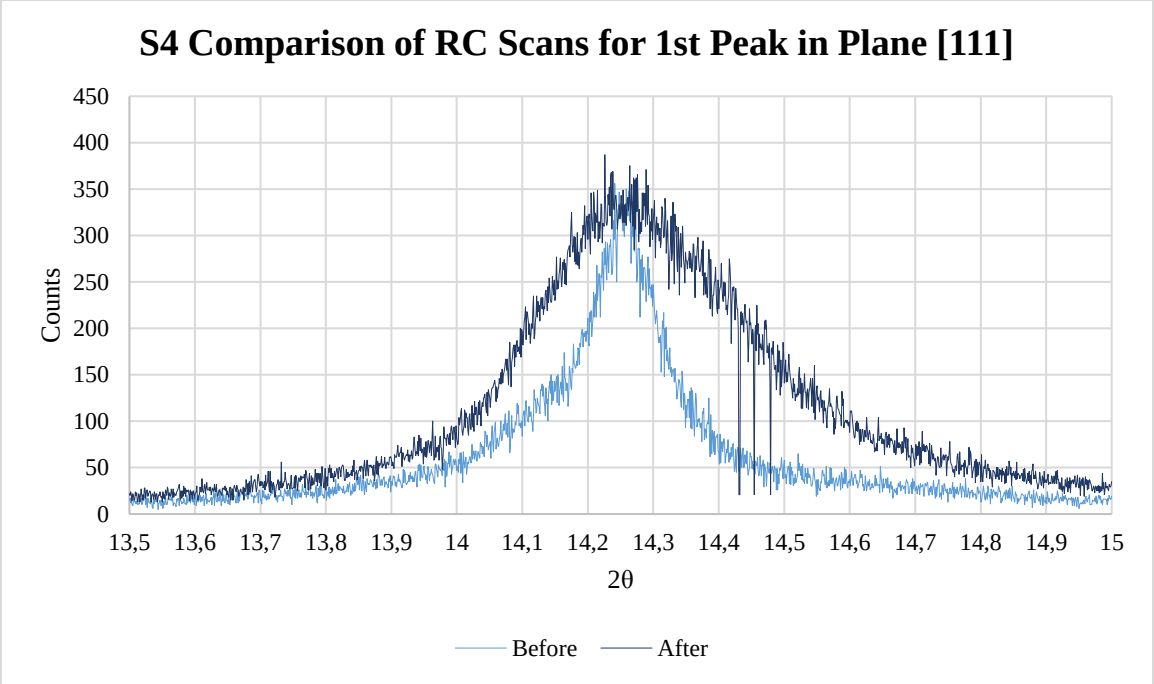

Figure 56 – Sample 4 Before and After Irradiation Rocking Curve Scan for Plane (111).

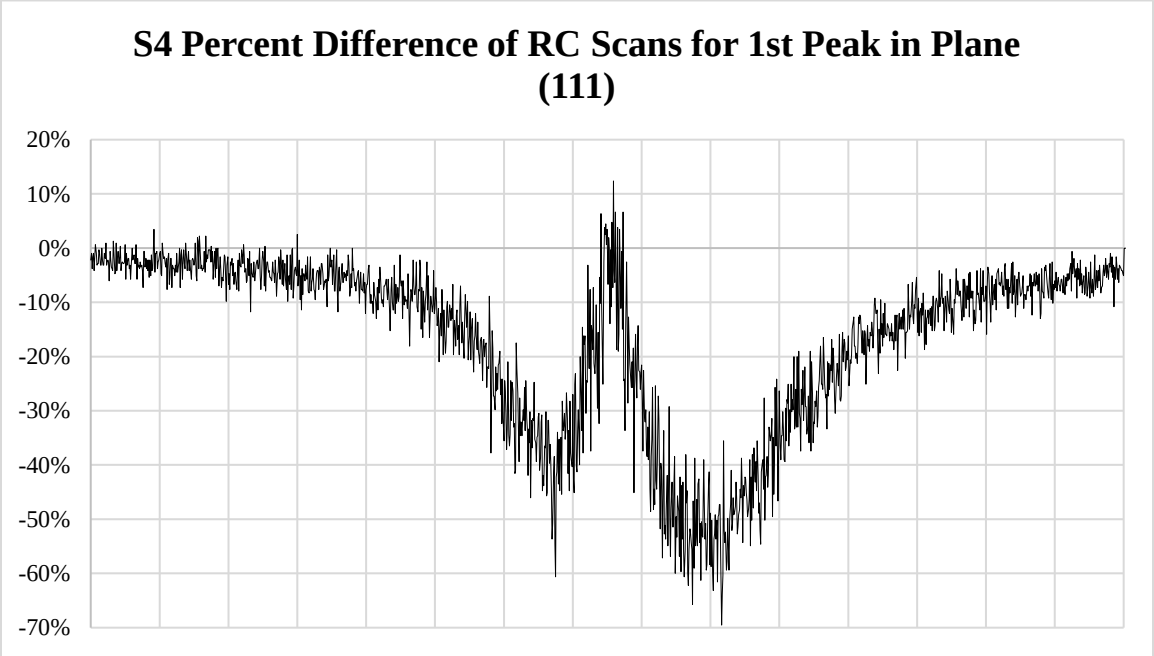

Figure 57 – Percent Difference for Sample 4 Before and After Irradiation Rocking Curve Scan for Plane (111).

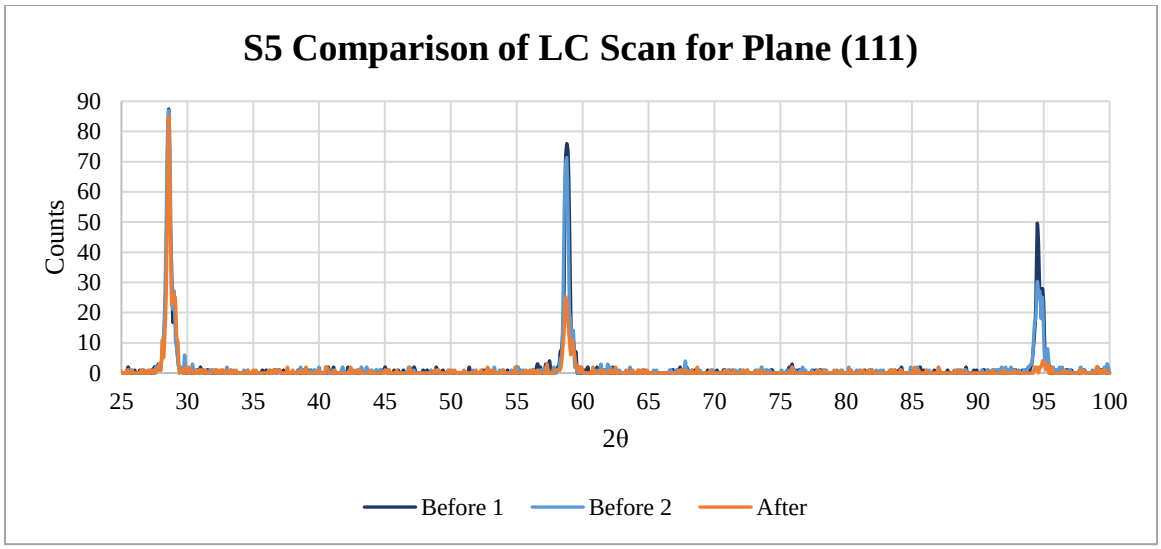

Figure 58 – XRD Locked Coupled Scan for Plane (111) of UO_2 crystal sample 5 before and after irradiation.

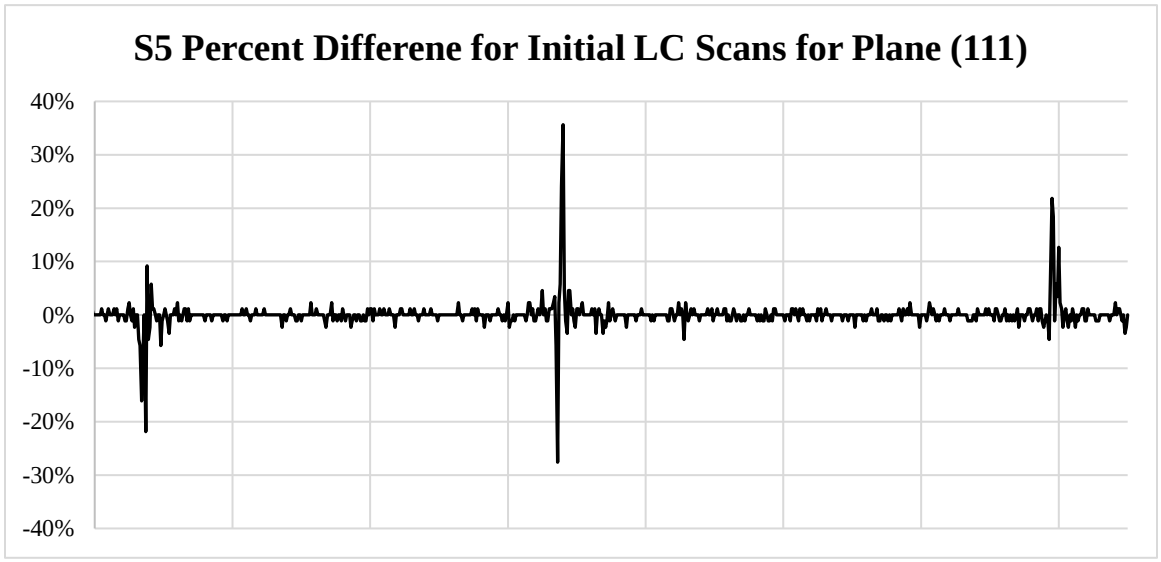

Figure 59 – Percent Difference for XRD Locked Coupled Scan for Plane (111) of UO_2 crystal sample 5 before1 and before2 irradiation.

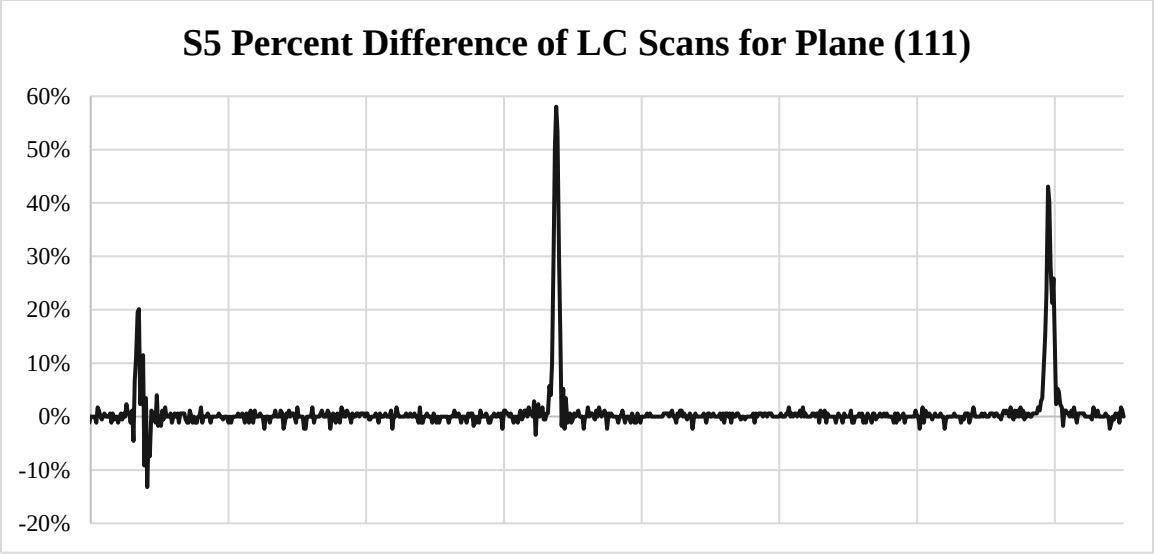

Figure 60 – Percent Difference for XRD Locked Coupled Scan for Plane (111) of UO_2 crystal sample 5 average before and after irradiation.

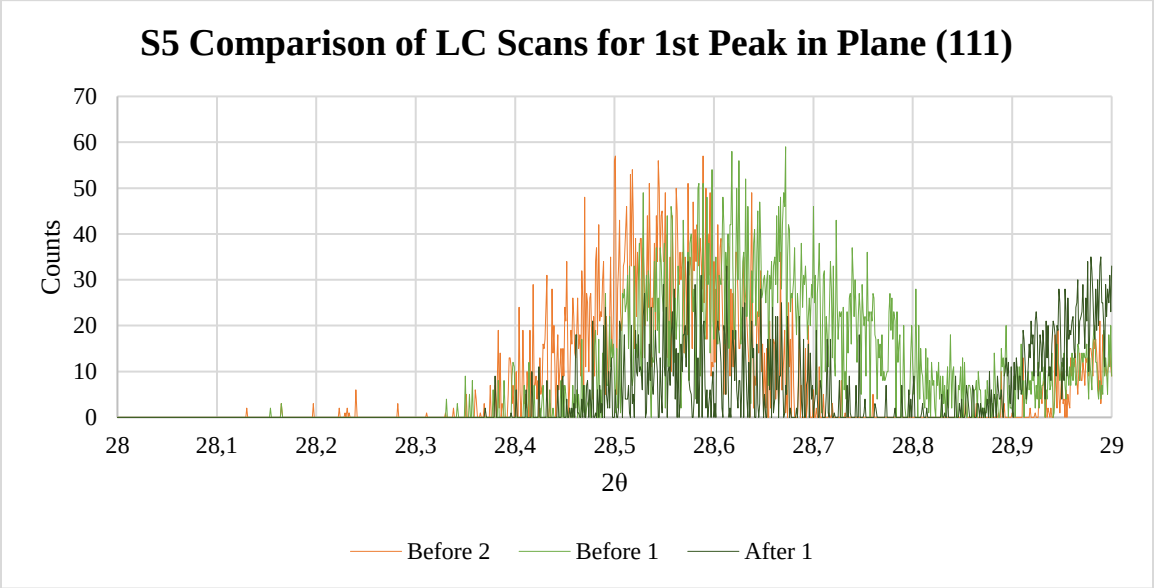

Figure 61 – Sample 5 Before and After Irradiation Locked Coupled Scan for Plane (111).

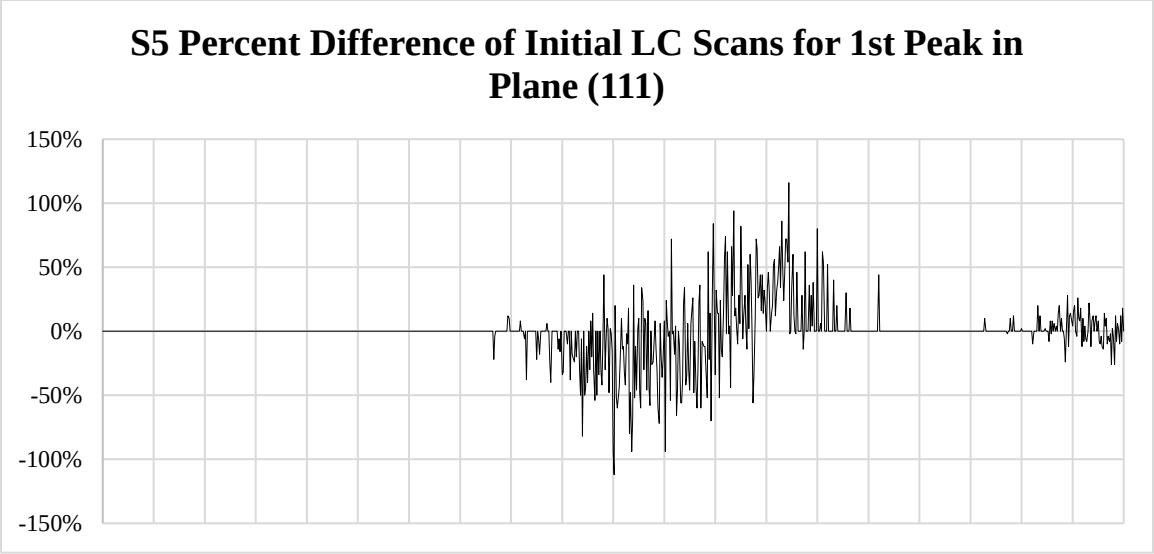

Figure 62 – Percent Difference for Sample 5 Before1 and Before2 Irradiation Locke Coupled Scan for Plane (111).

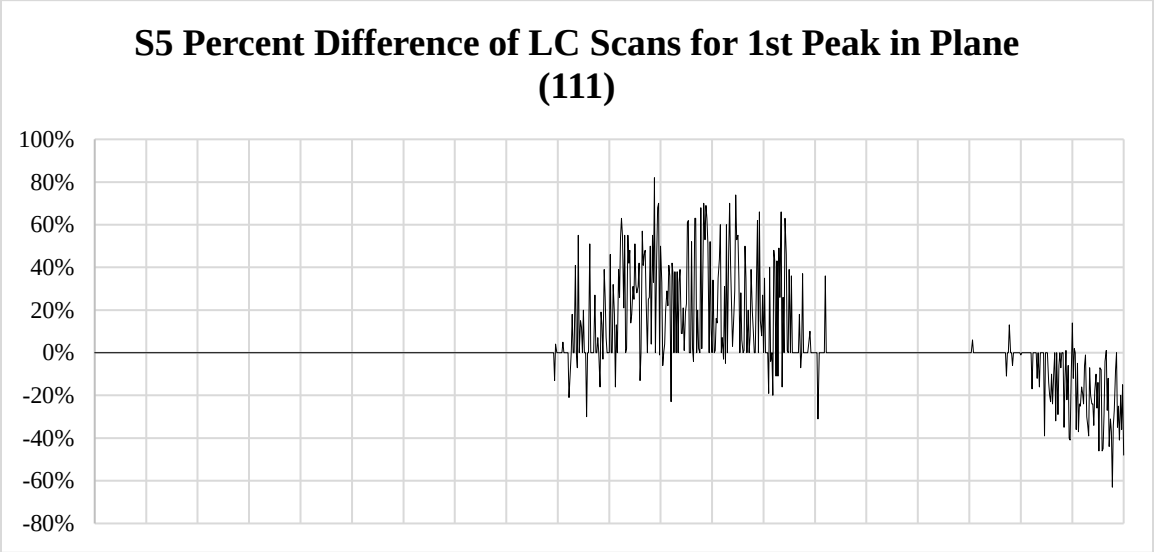

Figure 63 – Percent Difference for Sample 5 Averaged Before and After Irradiation Locked Coupled Scan for Plane (111).

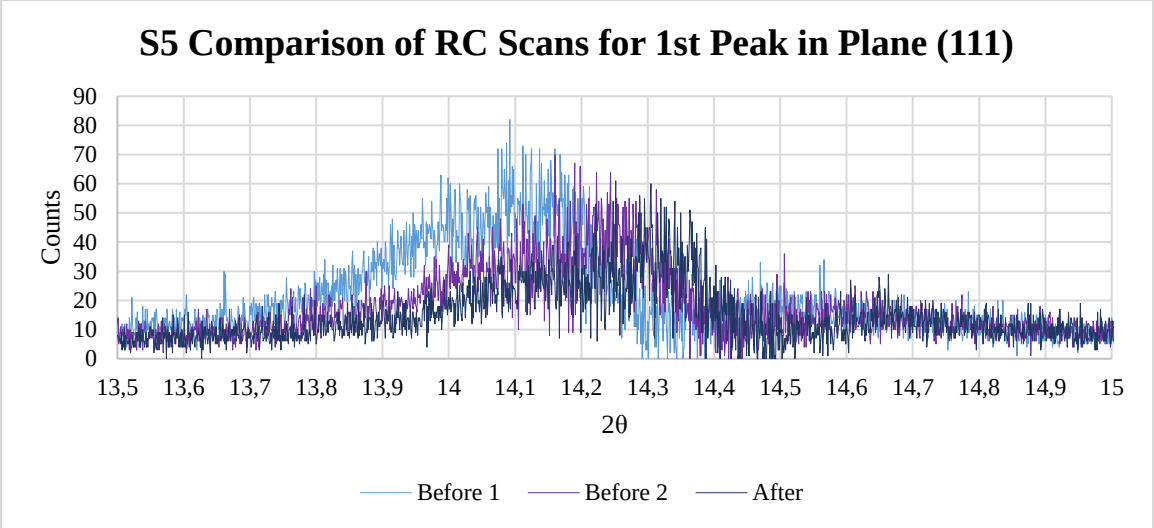

Figure 64 - Sample 5 Before and After Irradiation Rocking Curve Scan for Plane (111).

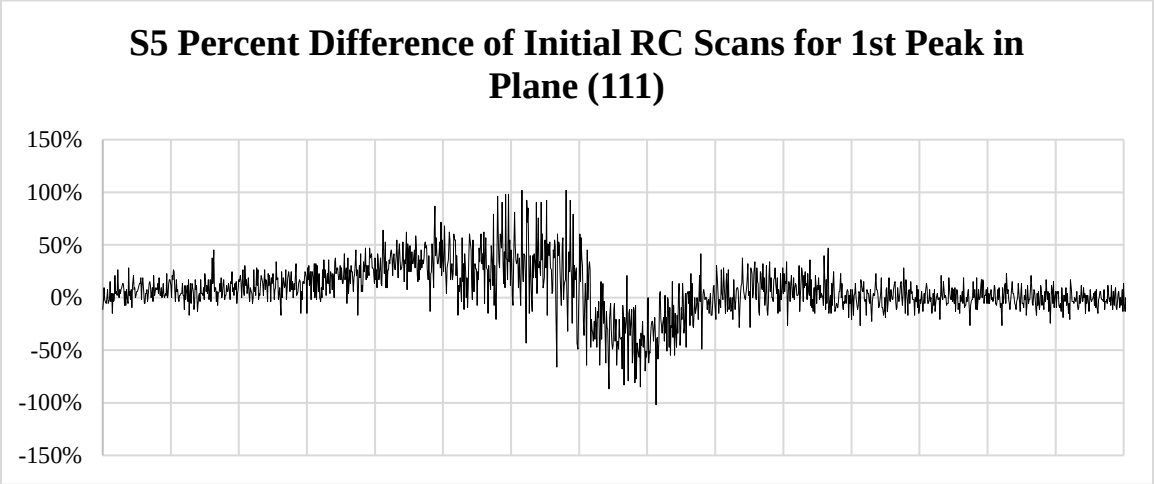

Figure 65 – Percent Difference for Sample 5 Before1 and Before2 Irradiation Rocking Curve Scan for Plane (111).

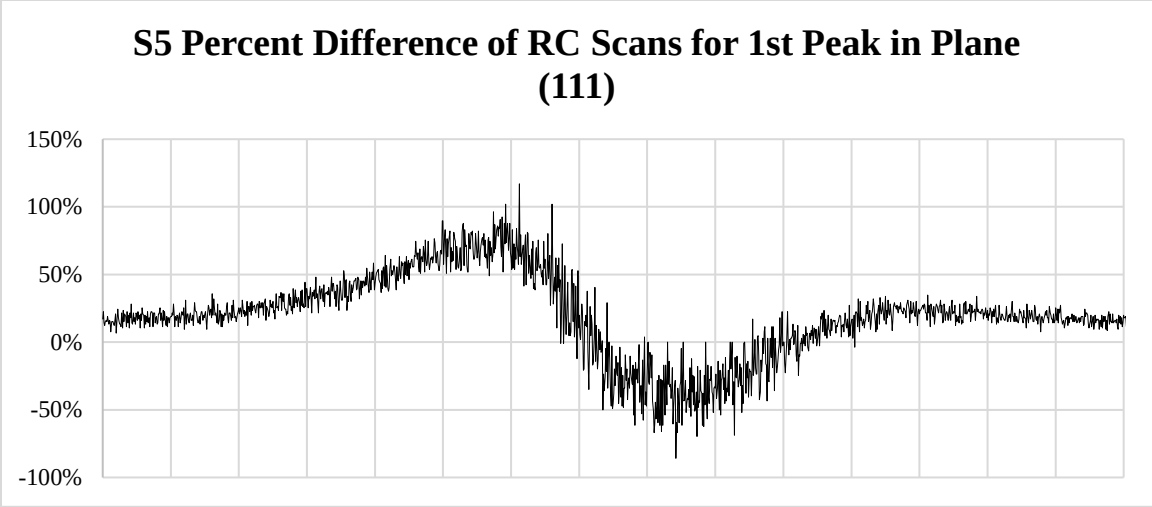

Figure 66 – Percent Difference for Sample 5 Averaged Before and After Irradiation Rocking Curve Scan for Plane (111).

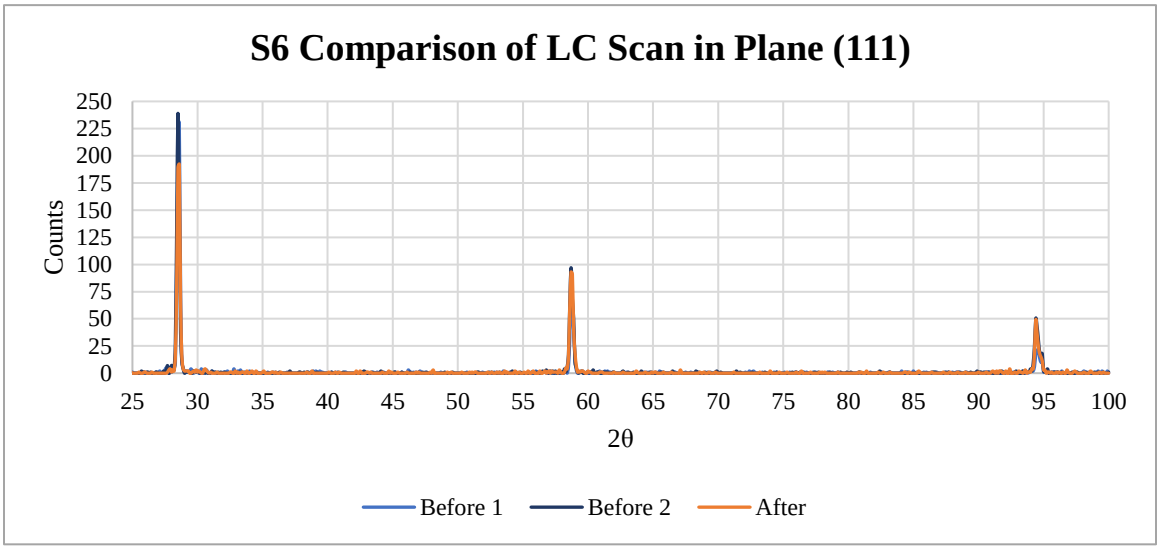

Figure 67 – XRD Locked Coupled Scan for Plane (111) of UO_2 crystal sample 6 before and after irradiation.

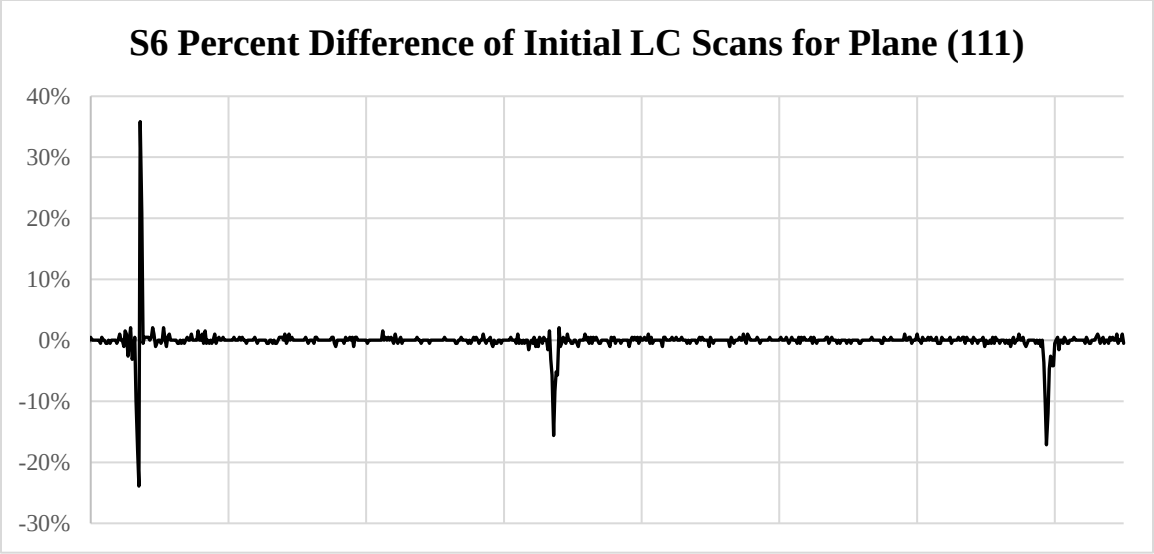

Figure 68 – Percent Difference for XRD Locked Coupled Scan for Plane (111) of UO_2 crystal sample 6 before1 and before2 irradiation.

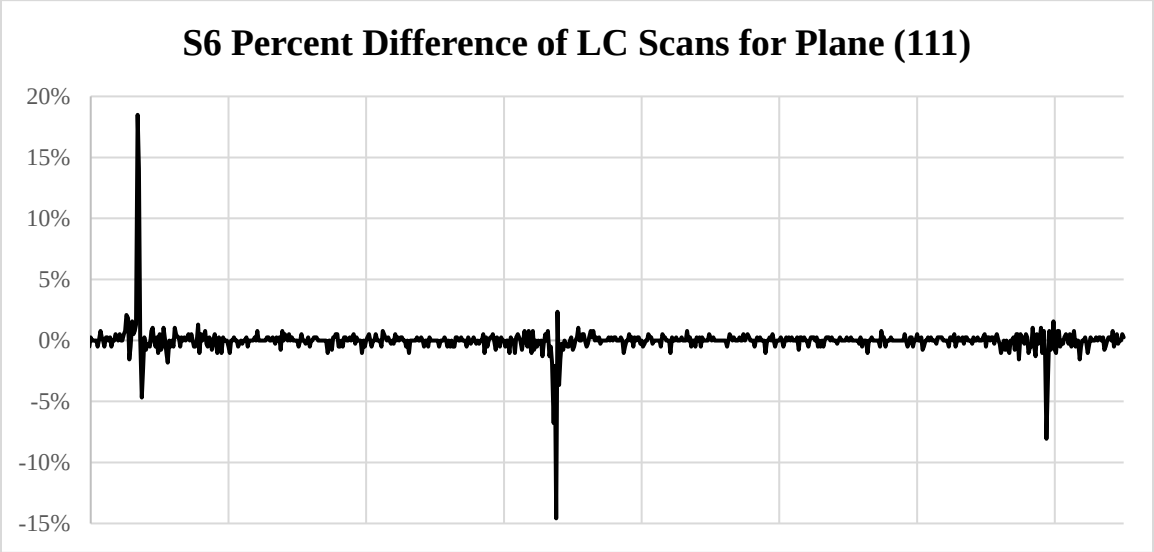

Figure 69 – Percent Difference for XRD Locked Coupled Scan for Plane (111) of UO_2 crystal sample 6 averaged before and after irradiation.

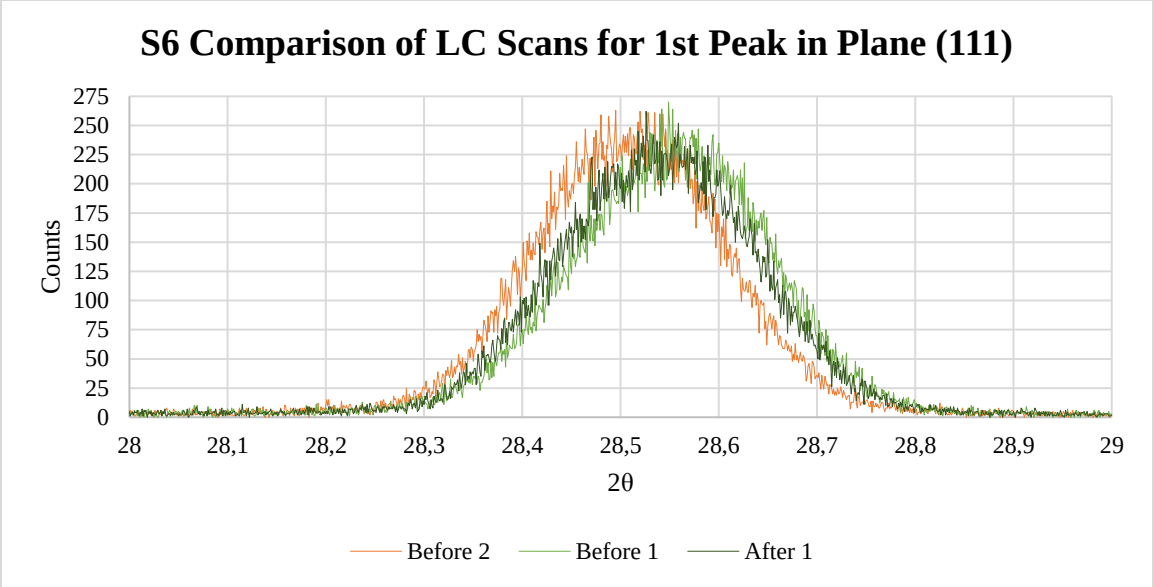

Figure 70 – Sample 6 Before and After Irradiation Locked Coupled Scan for Plane (111).

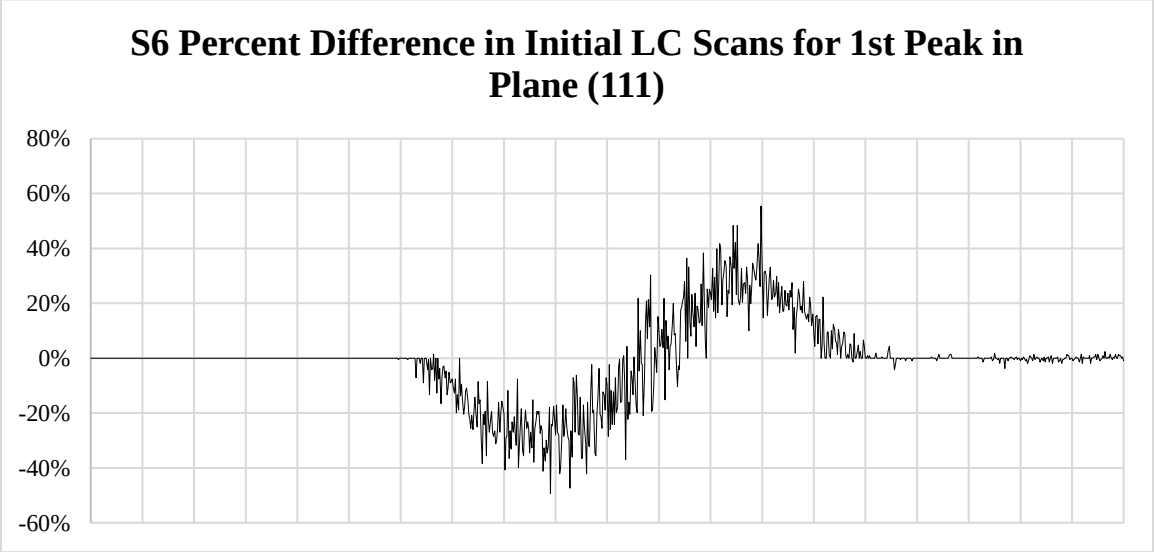

Figure 71 – Percent Difference for Sample 6 Before1 and Before2 Irradiation Locked Coupled Scan for Plane (111).

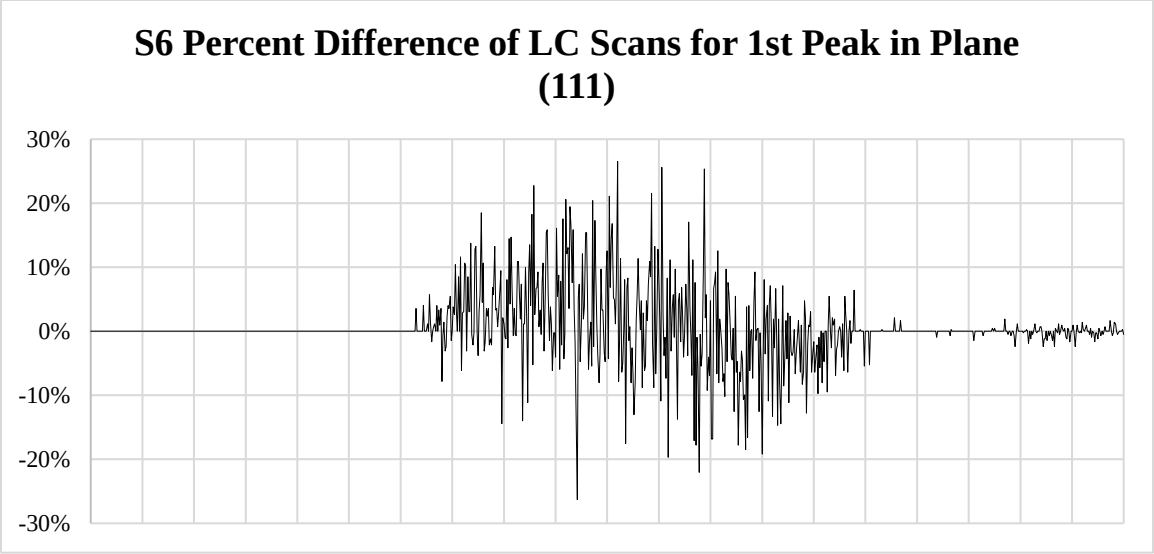

Figure 72 – Percent Difference for Sample 6 Averaged Before and After Irradiation Locked Coupled Scan for Plane (111).

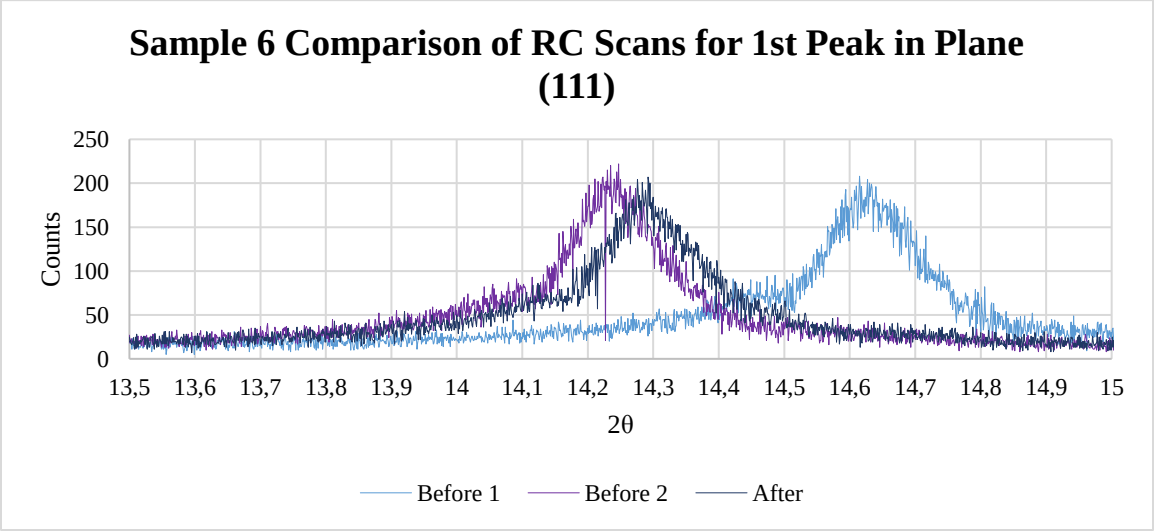

Figure 73 – Sample 6 Before and After Irradiation Rocking Curve Scan for Plane (111).

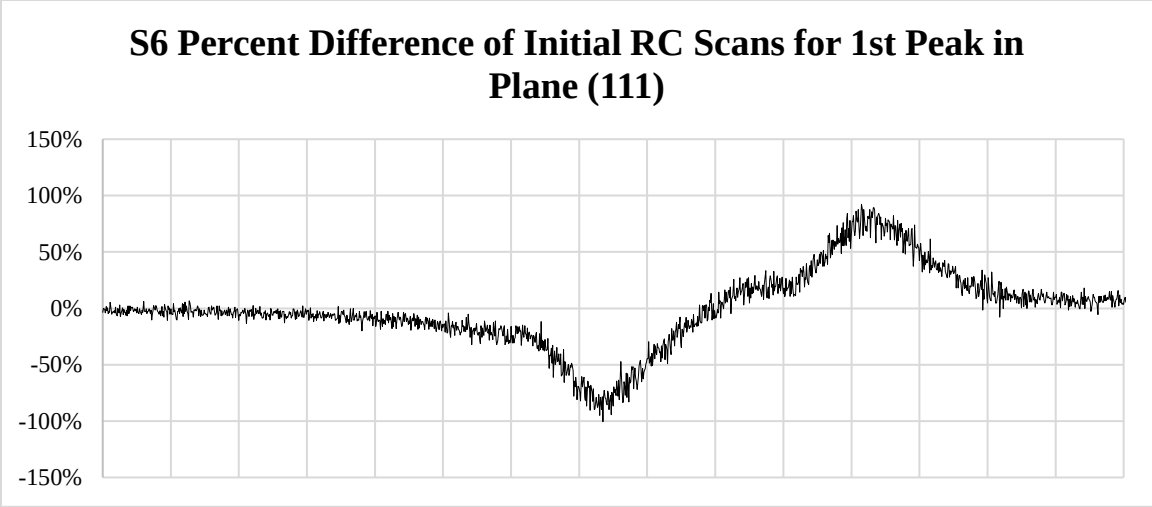

Figure 74 – Percent Difference for Sample 6 Before1 and Before2 Irradiation Rocking Curve Scan for Plane (111).

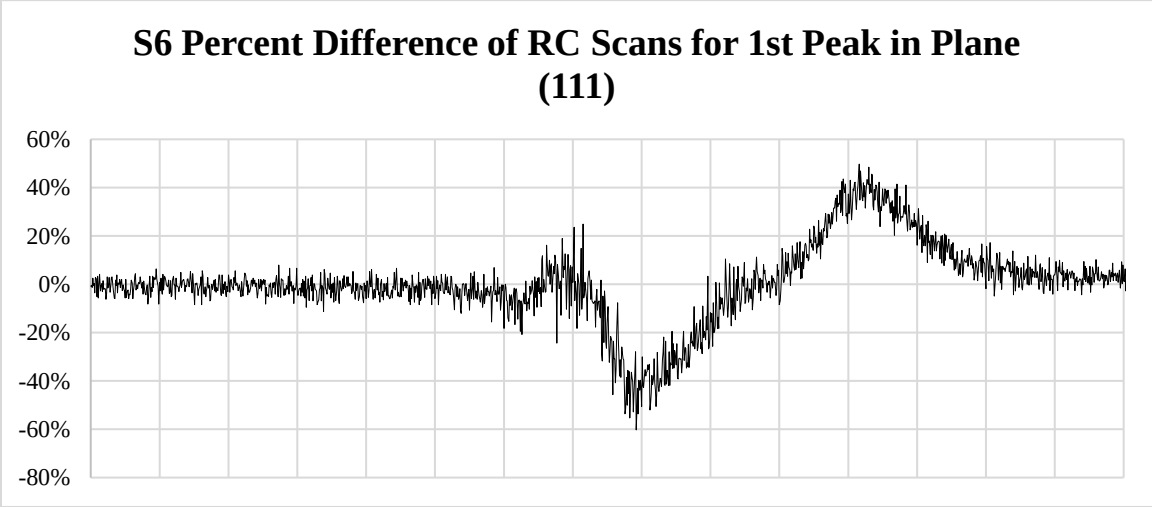

Figure 75 – Percent Difference for Sample 6 Averaged Before and After Irradiation Rocking Curve Scan for Plane (111).

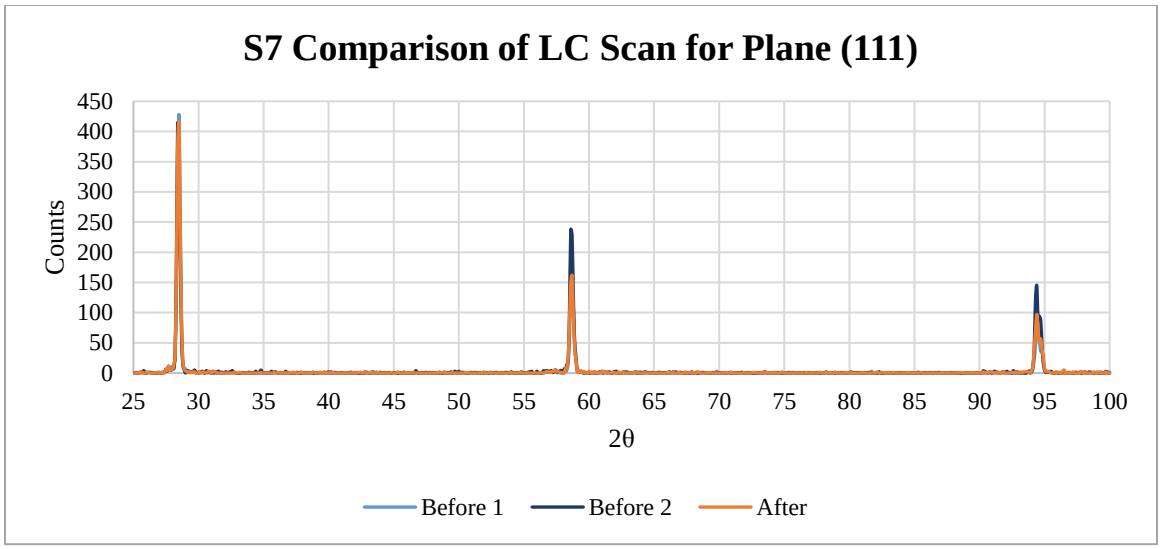

Figure 76 – XRD Locked Coupled Scan for Plane (111) of UO_2 crystal sample 7 before and after irradiation.

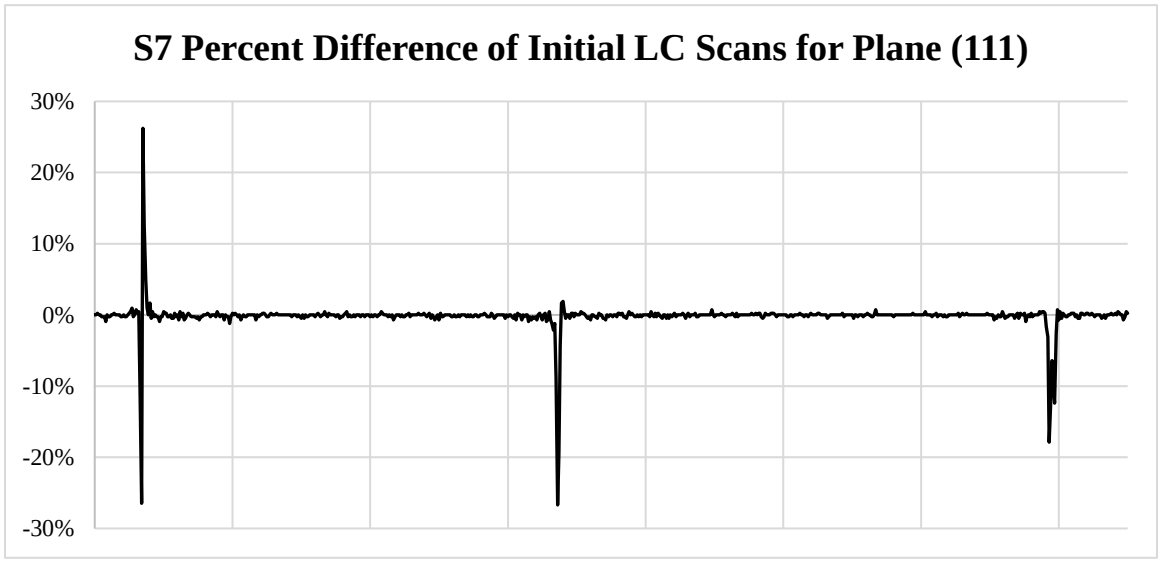

Figure 77 – Percent Difference for XRD Locked Coupled Scan for Plane (111) of UO_2 crystal sample 7 before1 and before2 irradiation.

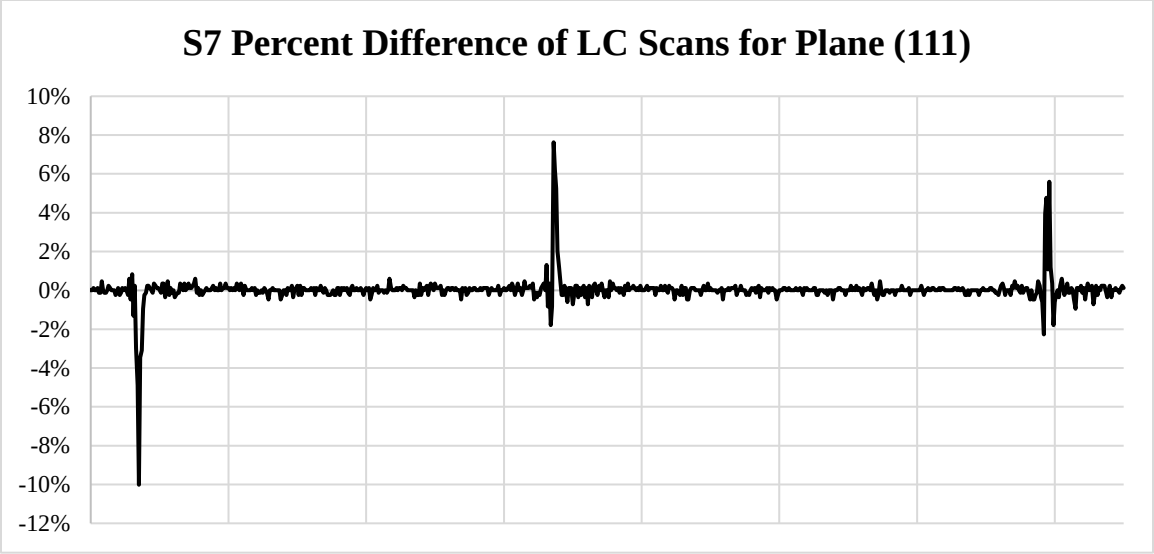

Figure 78 – Percent Difference for XRD Locked Coupled Scan for Plane (111) of UO_2 crystal sample 7 averaged before and after irradiation.

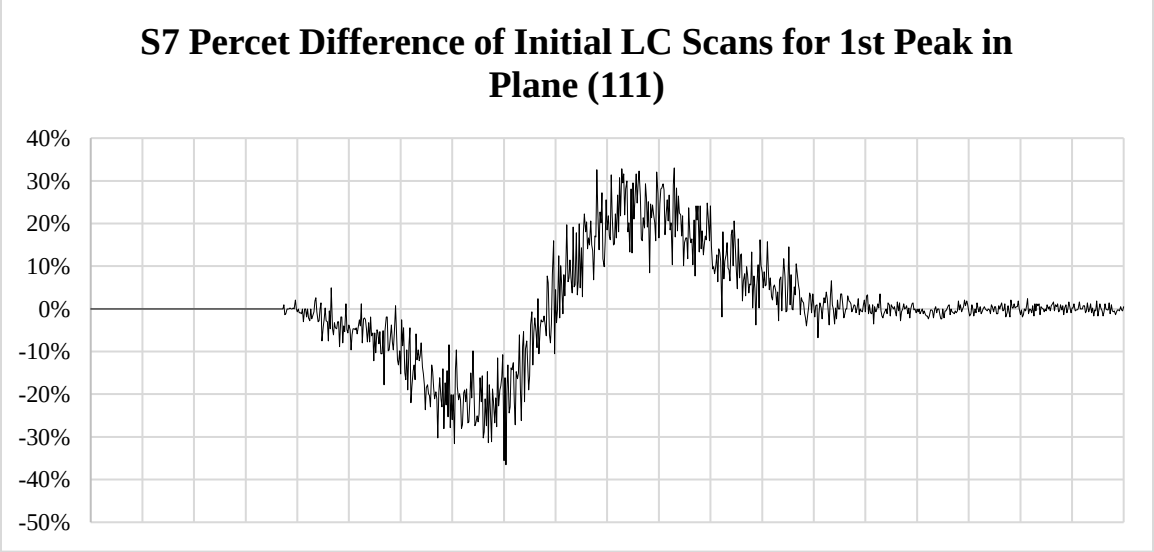

Figure 79 – Percent Difference for Sample 7 Before1 and Before2 Irradiation Locked Coupled Scan for Plane (111).

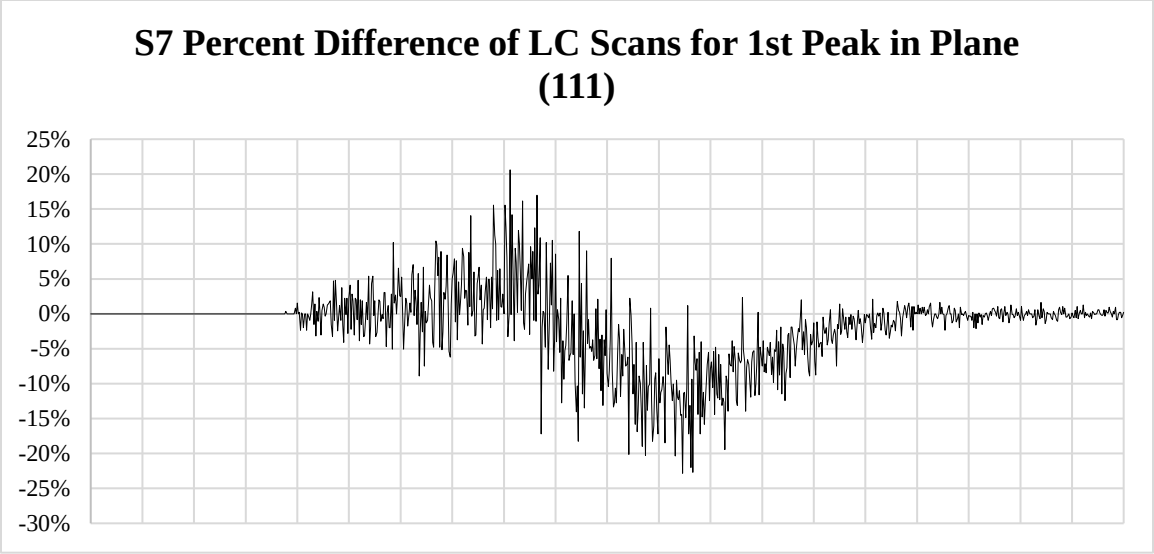

Figure 80 – Percent Difference for Sample 7 Averaged Before and After Irradiation Locked Coupled Scan for Plane (111).

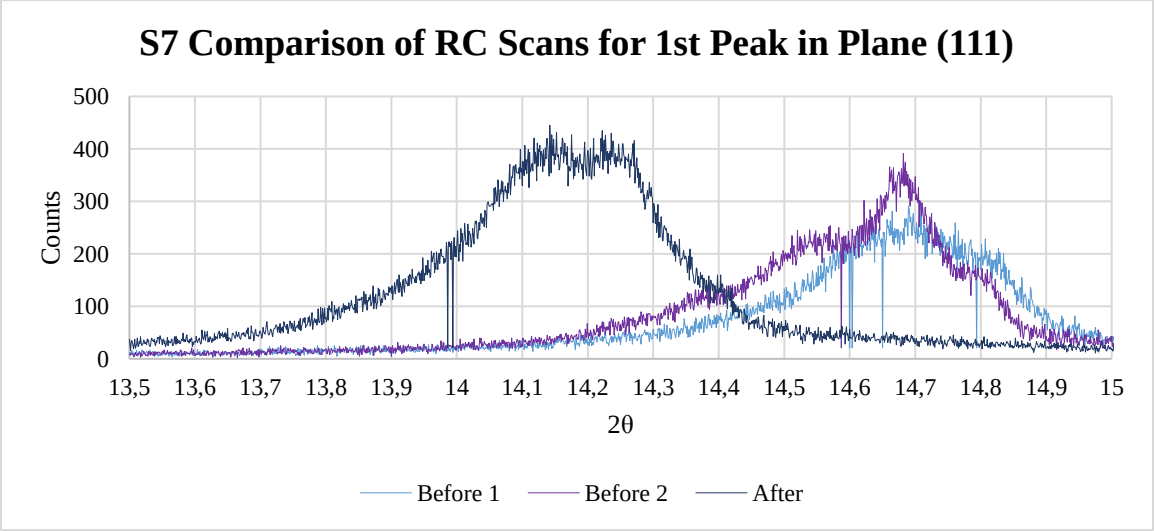

Figure 81 – Sample 7 Before and After Irradiation Rocking Curve Scan for Plane (111).

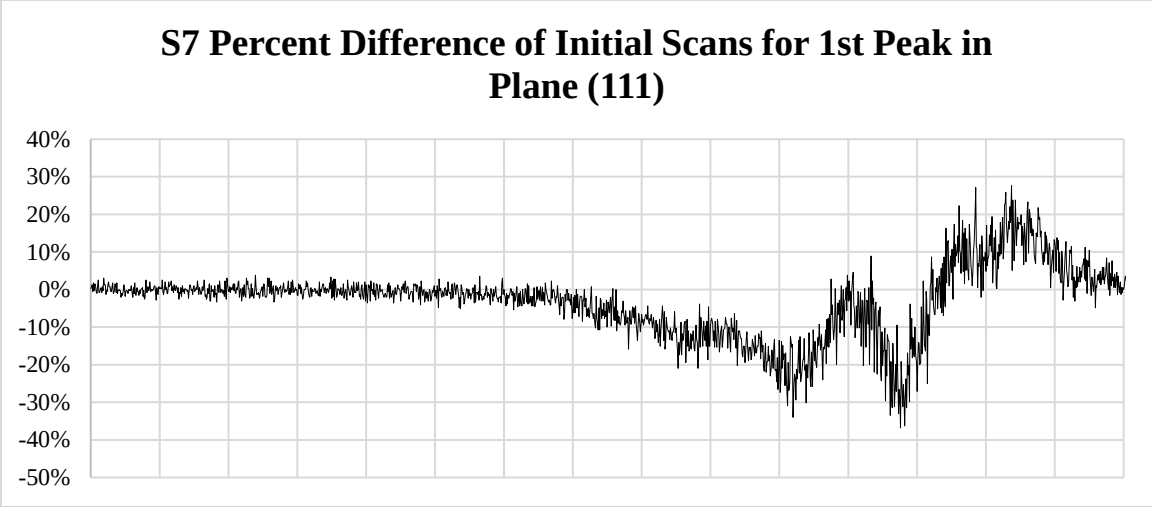

Figure 82 – Percent Difference for Sample 7 Before1 and Before2 Irradiation Rocking Curve Scan for Plane (111).

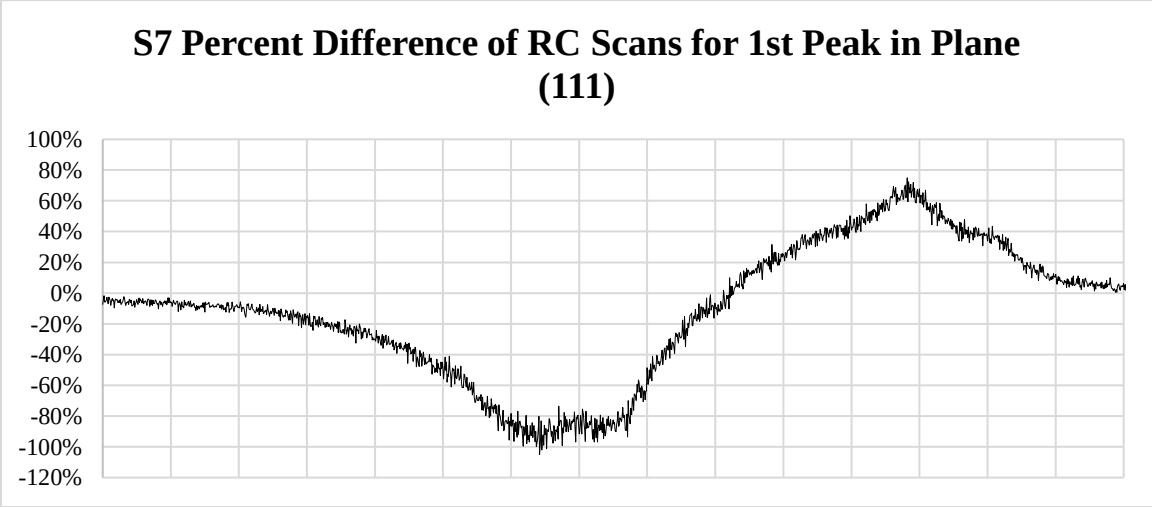

Figure 83 – Percent Difference for Sample 7 Averaged Before and After Irradiation Rocking Curve Scan for Plane (111).

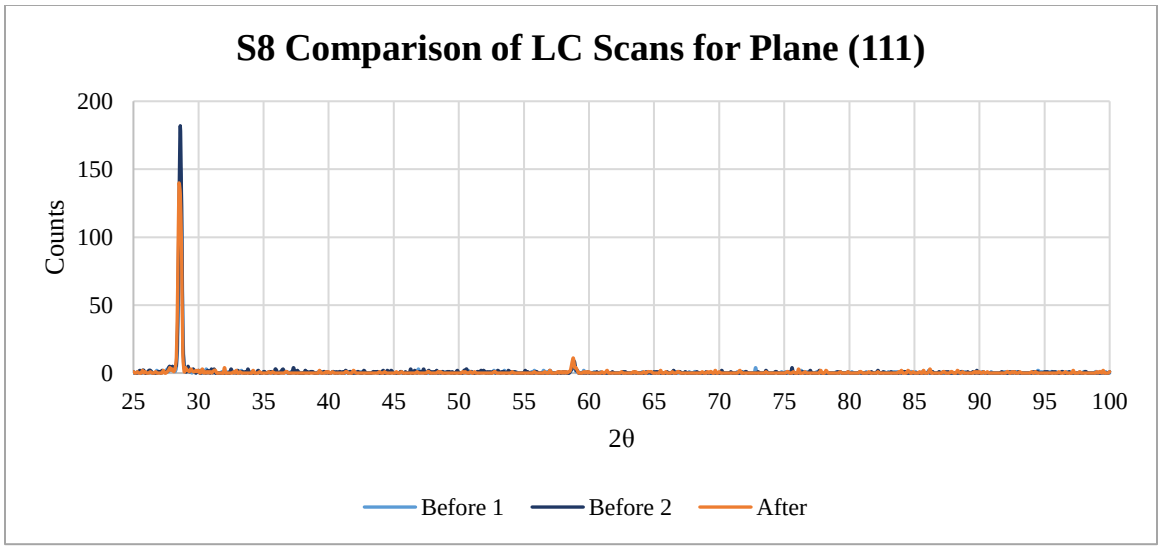

Figure 84 – XRD Locked Coupled Scan for Plane (111) of UO_2 crystal sample 8 before and after irradiation.

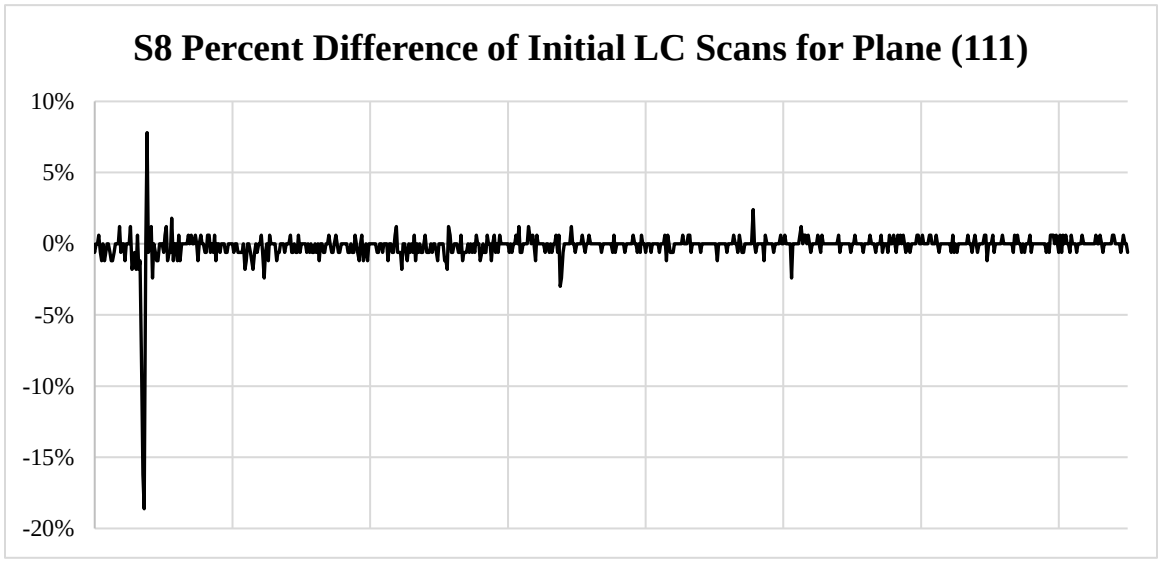

Figure 85 – Percent Difference for XRD Locked Coupled Scan for Plane (111) of UO_2 crystal sample 8 before1 and before2 irradiation.

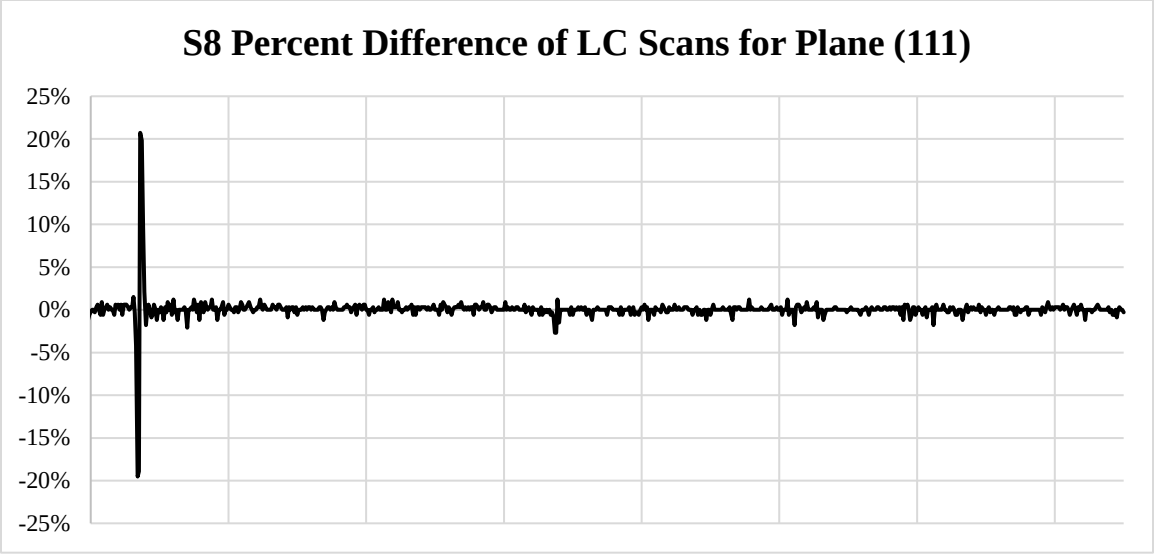

Figure 86 – Percent Difference for XRD Locked Coupled Scan for Plane (111) of UO_2 crystal sample 8 averaged before and after irradiation.

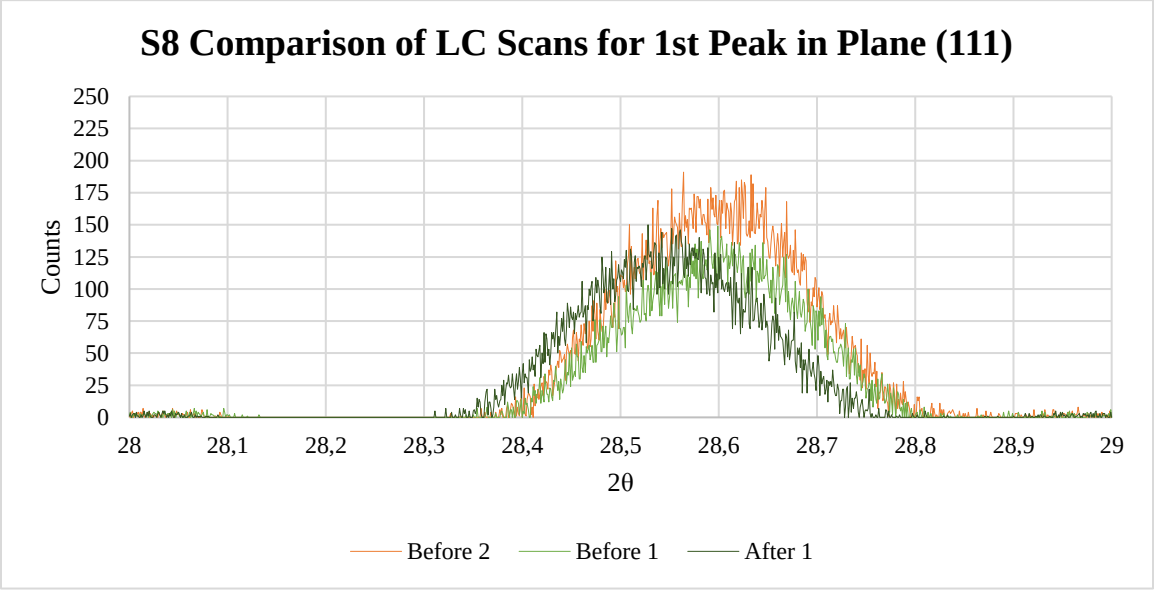

Figure 87 – Sample 8 Before and After Irradiation Locked Coupled Scan for Plane (111).

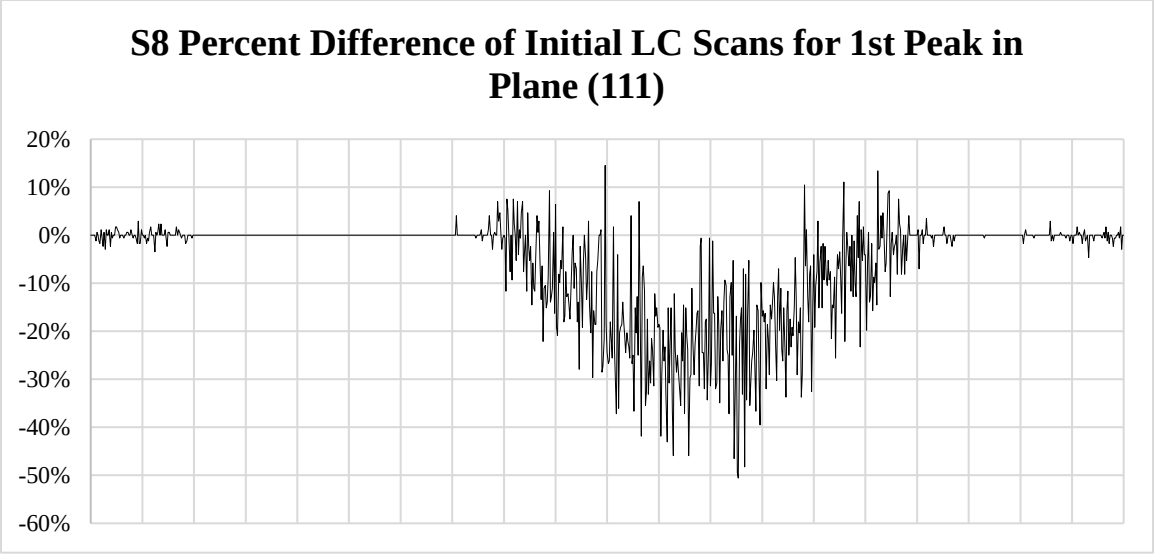

Figure 88 – Percent Difference for Sample 8 Before1 and Before2 Irradiation Locked Coupled Scan for Plane (111).

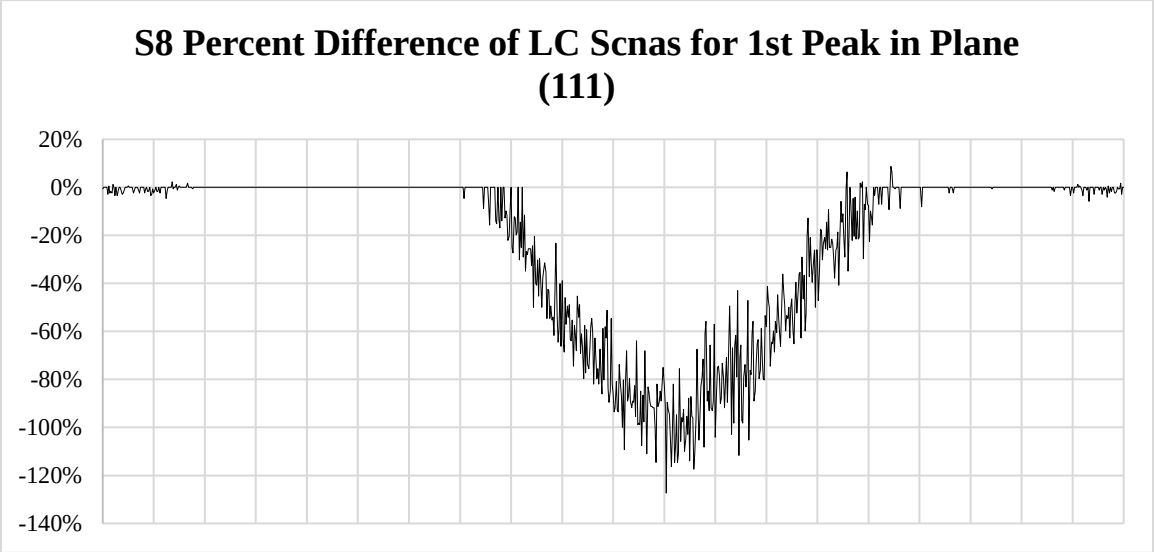

Figure 89 – Percent Difference for Sample 8 Averaged Before and After Irradiation Locked Coupled Scan for Plane (111).

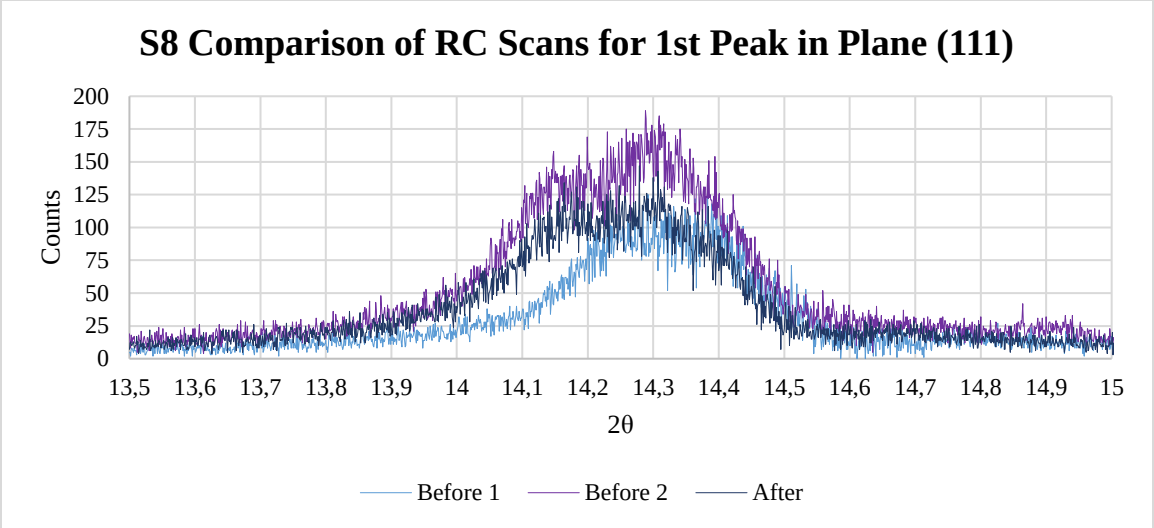

Figure 90 – Sample 8 Before and After Irradiation Rocking Curve Scan for Plane (111).

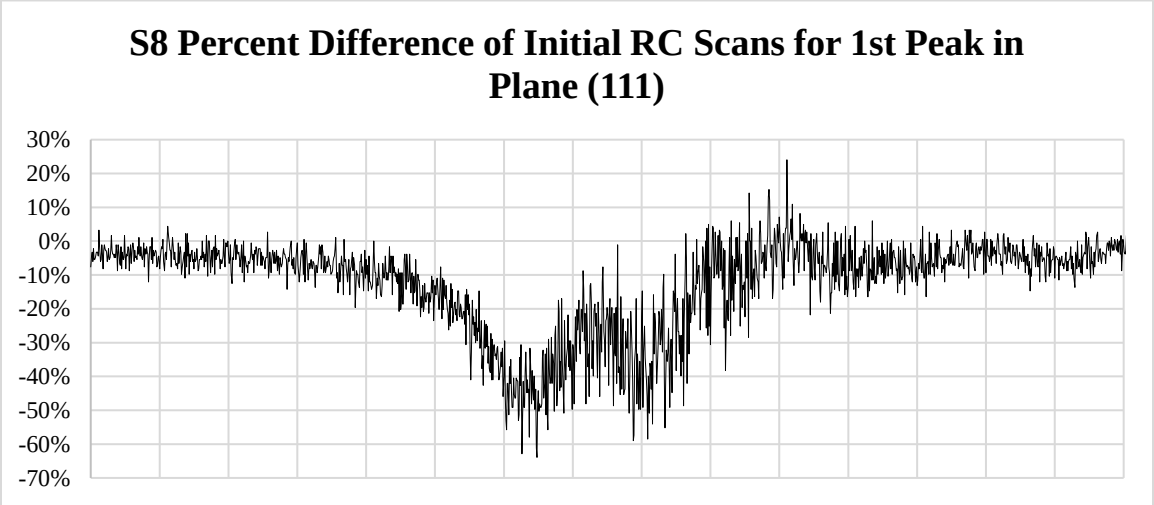

Figure 91 – Percent Difference for Sample 8 Before1 and Before2 Irradiation Rocking Curve Scan for Plane (111).

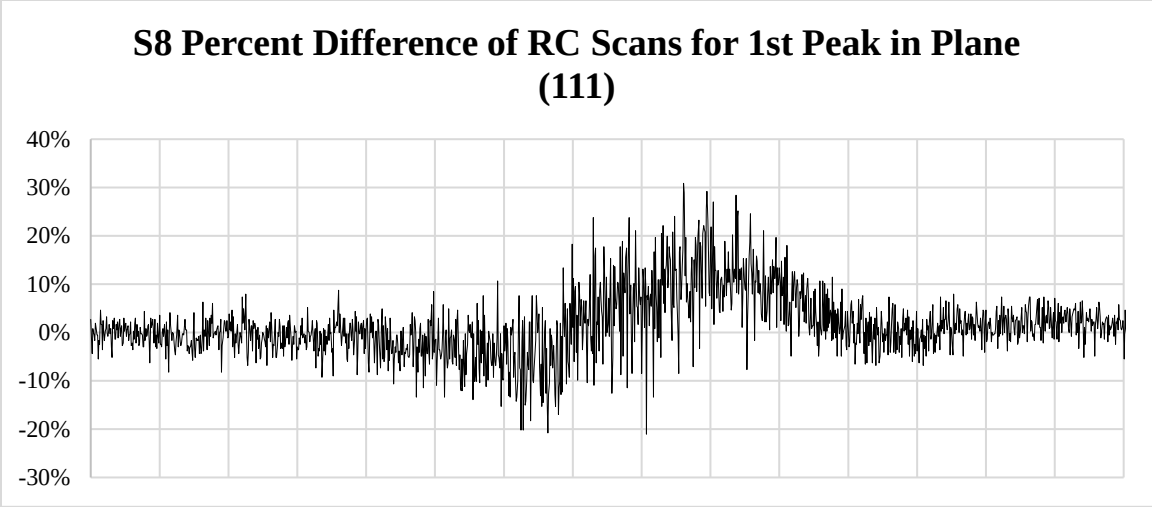

Figure 92 – Percent Difference for Sample 8 Averaged Before and After Irradiation Rocking Curve Scan for Plane (111).

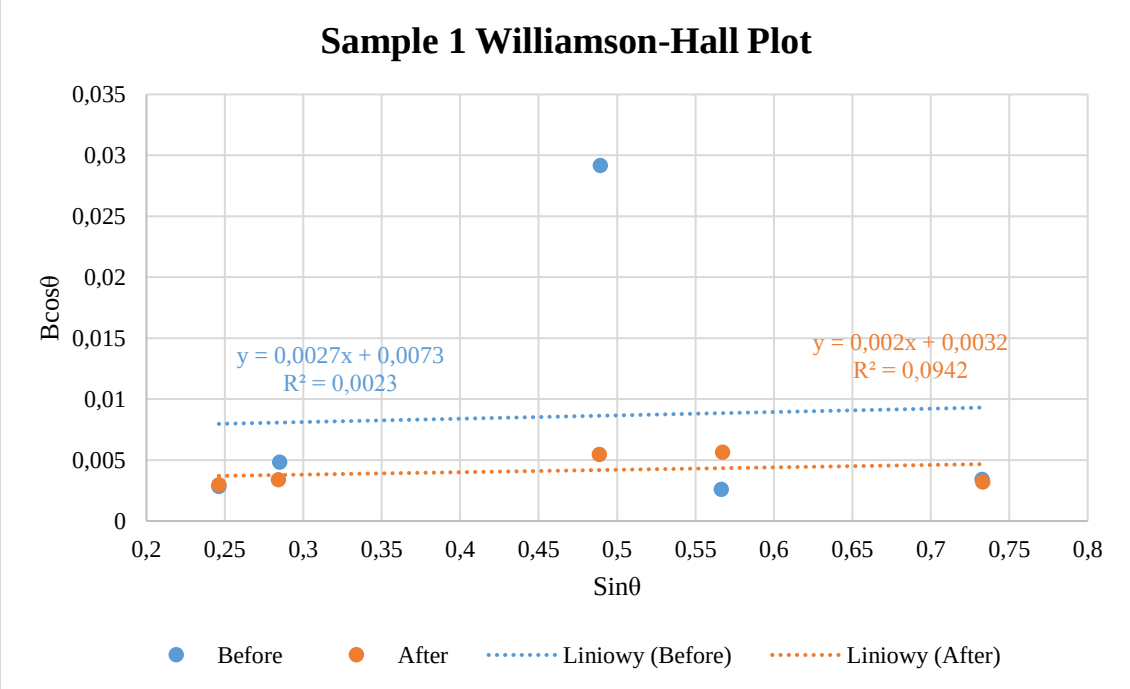

Figure 93 – Sample 1 Williamson-Hall plot for size and strain calculations.

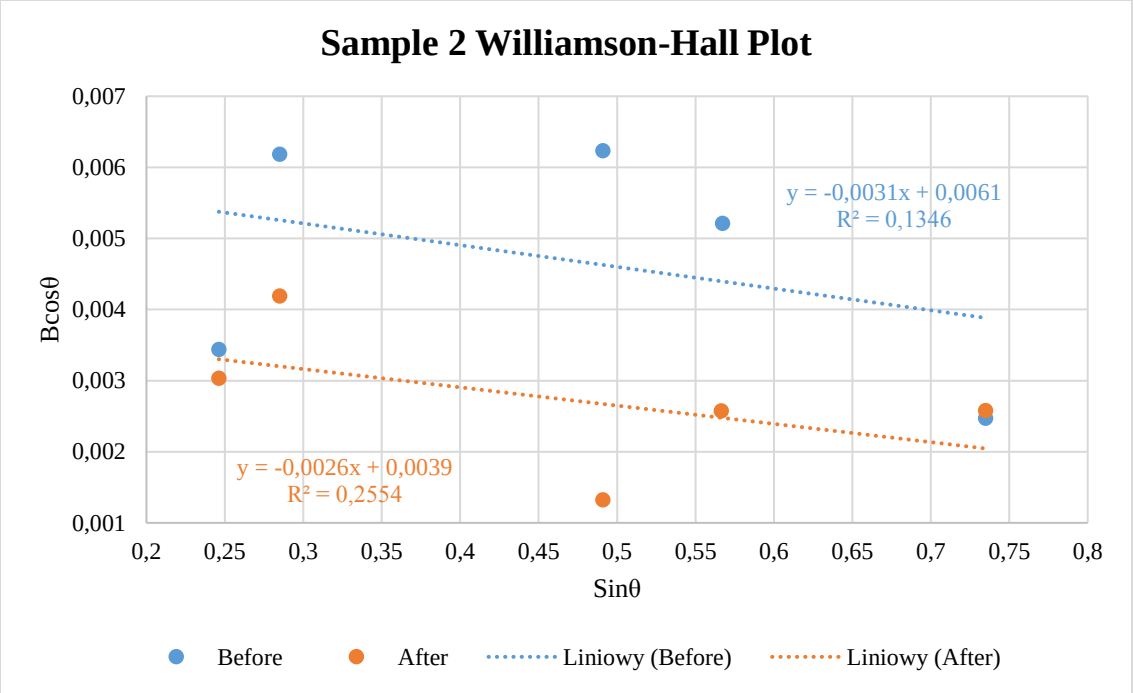

Figure 94 – Sample 2 Williamson-Hall plot for size and strain calculations.

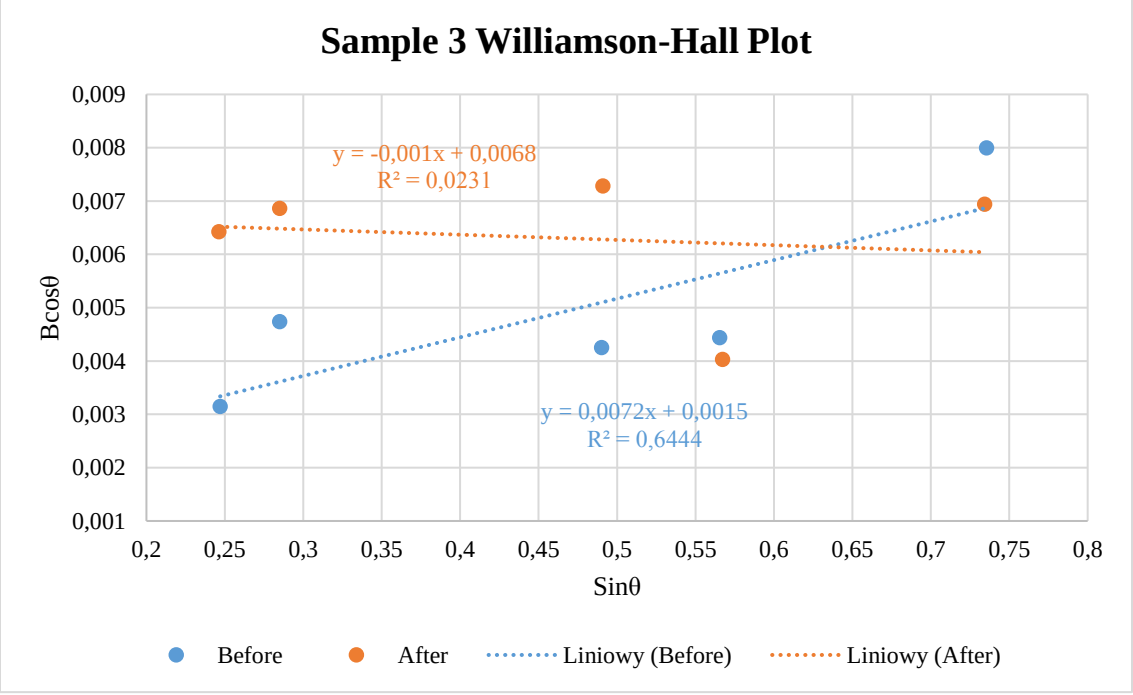

Figure 95 – Sample 3 Williamson-Hall plot for size and strain calculations.

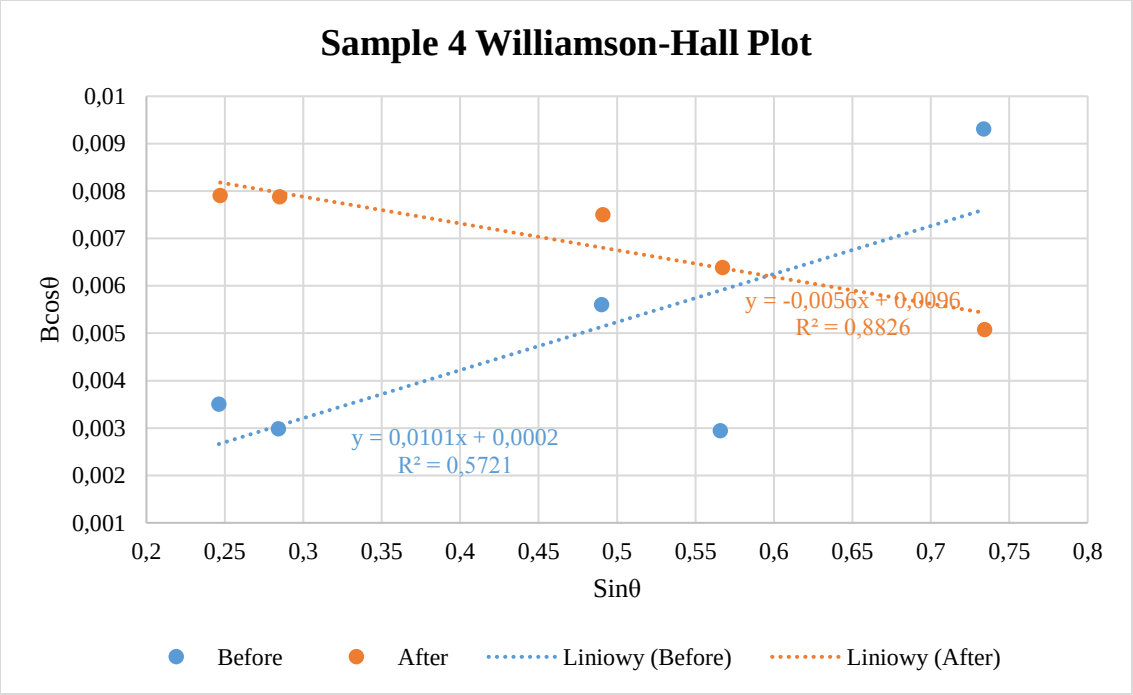

Figure 96 – Sample 4 Williamson-Hall plot for size and strain calculations.

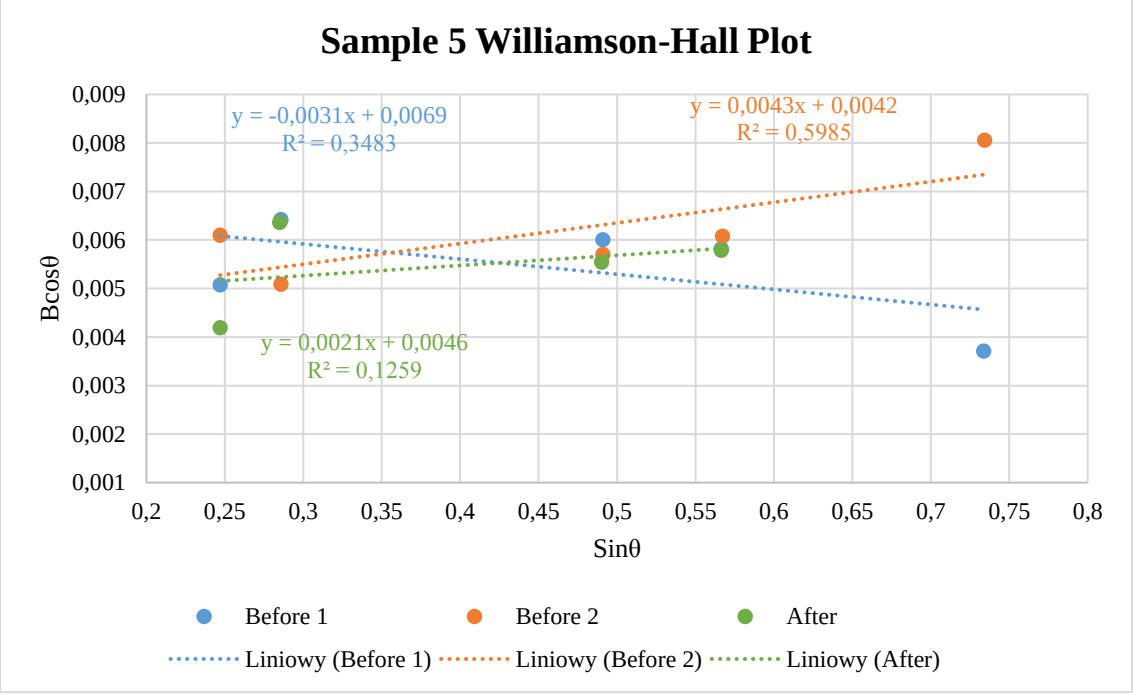

Figure 97 – Sample 5 Williamson-Hall plot for size and strain calculations.

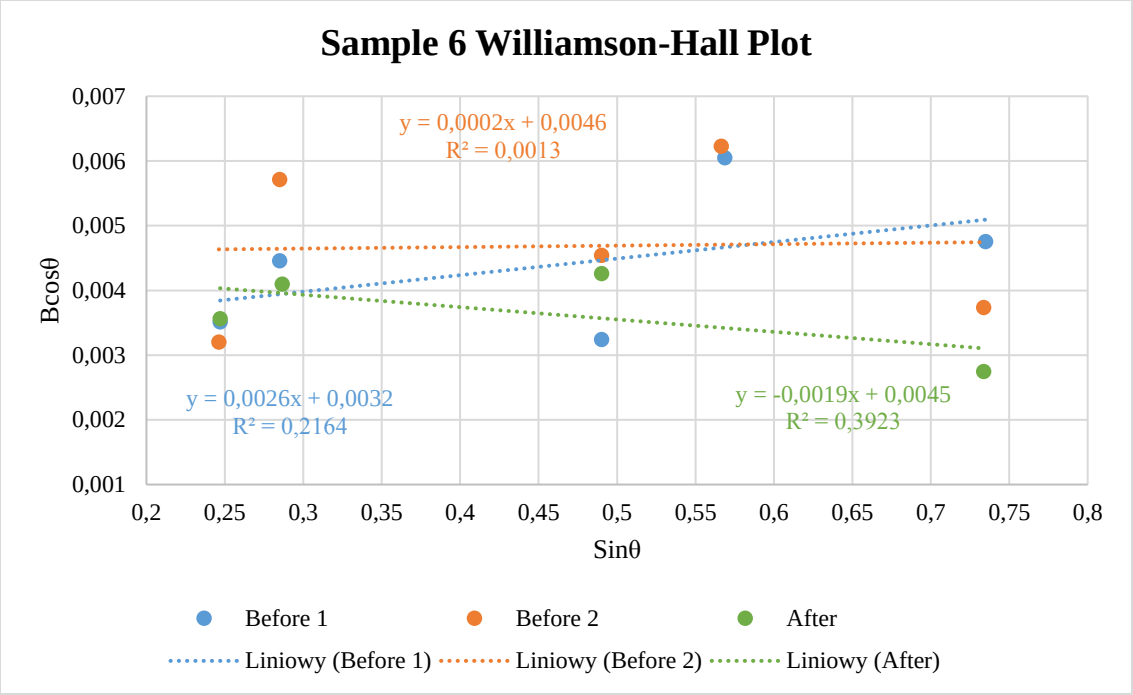

Figure 98 - Sample 6 Williamson-Hall plot for size and strain calculations.

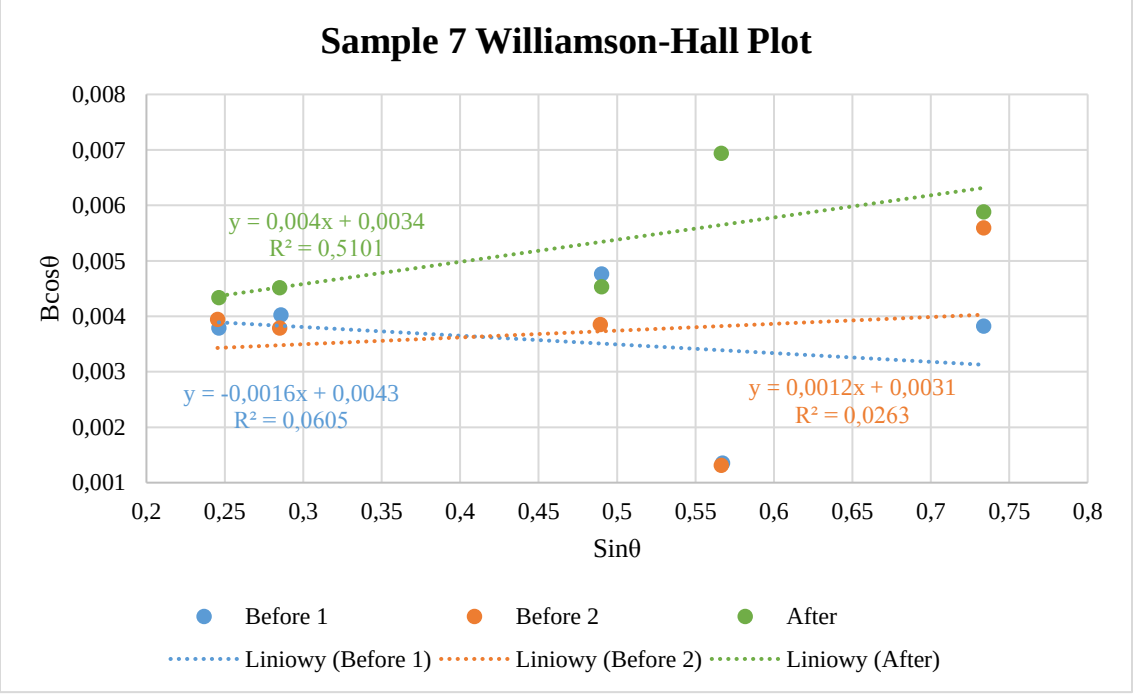

Figure 99 – Sample 7 Williamson-Hall plot for size and strain calculations.

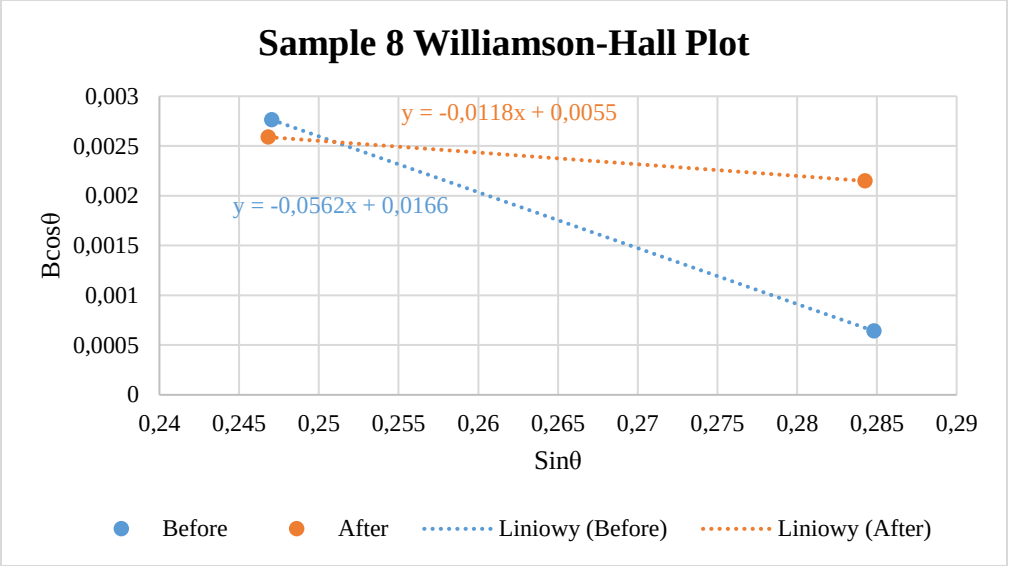

Figure 100 - Sample 8 Williamson-Hall plot for size and strain calculations.

Table 6 – FWHM calculations using LC scans for all of the UO_2 samples.

Locked Scans								
Sample	**Plane**	**FWHM m**	**FWHM inst**	**FWHM Bef**	**FWHM m**	**FWHM inst**	**FWHM Aft**	**Diff**
1	111	0.2018	0.1525	0.1322	0.1834	0.1525	0.1019	0.0303
	200	0.1444	0.1525	0.0490	0.3047	0.1525	0.2638	0.2148
2	111	0.1853	0.1525	0.1053	0.1761	0.1525	0.0881	0.0172
	200	0.2700	0.1525	0.2228	0.1872	0.1525	0.1086	0.1142
3	111	0.1830	0.1525	0.1012	0.4526	0.1525	0.4261	0.3250
	200	0.2192	0.1525	0.1575	0.3355	0.1525	0.2988	0.1414
4	111	0.1872	0.1525	0.1086	0.3960	0.1525	0.3655	0.2569
	200	0.1539	0.1525	0.0207	0.2567	0.1525	0.2065	0.1858
5	111	0.2729	0.1525	0.2263	0.2530	0.1525	0.2019	0.0244
	200	0.3529	0.1525	0.3182	0.2530	0.1525	0.2019	0.1163
6	111	0.2071	0.1525	0.1400	0.2240	0.1525	0.1641	0.0240
	200	0.1881	0.1525	0.1100	0.2282	0.1525	0.1698	0.0597
7	111	0.2311	0.1525	0.1736	0.2593	0.1525	0.2097	0.0361
	200	0.1548	0.1525	0.0263	0.1588	0.1525	0.0443	0.0180
8	111	0.2235	0.1525	0.1634	0.2161	0.1525	0.1531	0.0103
	200	0.1476	0.1525	0.0383	0.0822	0.1525	0.1285	0.0901

Table 7 – FWHM calculations using RC scans for all of the UO_2 samples.

Rocking Scans								
Sample	**Plane**	**FWHM m**	**FWHM inst**	**FWHM Bef**	**FWHM m**	**FWHM inst**	**FWHM Aft**	**Diff**
1	111	0.1428	0.1525	0.0535	0.1409	0.1525	0.0583	0.0048
	200	0.1289	0.1525	0.0815	0.1040	0.1525	0.1115	0.0300
2	111	0.5841	0.1525	0.5638	0.5304	0.1525	0.5080	0.0558
	200	0.3849	0.1525	0.3534	0.1699	0.1525	0.0749	0.2785
3	111	0.1270	0.1525	0.0844	0.2620	0.1525	0.2130	0.1286
	200	0.1637	0.1525	0.0595	0.3552	0.1525	0.3208	0.2613
4	111	0.1338	0.1525	0.0732	0.3412	0.1525	0.3052	0.2321
	200	0.1907	0.1525	0.1145	0.5329	0.1525	0.5106	0.3961
5	111	0.2435	0.1525	0.1898	0.2197	0.1525	0.1582	0.0317
	200	0.1984	0.1525	0.1268	0.2290	0.1525	0.1708	0.0440
6	111	0.1810	0.1525	0.0974	0.1990	0.1525	0.1278	0.0304
	200	0.1849	0.1525	0.1046	0.0895	0.1525	0.1235	0.0189
7	111	0.2671	0.1525	0.2193	0.3279	0.1525	0.2903	0.0710
	200	0.1390	0.1525	0.0628	0.1588	0.1525	0.0443	0.0186
8	111	0.2757	0.1525	0.2296	0.3000	0.1525	0.2583	0.0287
	200	0.3285	0.1525	0.2909	0.3347	0.1525	0.2979	0.0070

Table 8 – Maximum 2θ using LC scans and calculated values for 2θ.

Sample	**Plane**	**Max 2θ Bef**	**Max 2θ Aft**	**Max 2θ c**
1	111	28.54	28.50	28.24
	200	33.18	33.16	32.72
2	111	28.53	28.51	28.24
	200	33.13	33.13	32.72
3	111	28.57	28.62	28.24
	200	33.07	33.07	32.72
4	111	28.48	28.57	28.24
	200	33.07	33.03	32.72
5	111	28.58	28.64	28.24
	200	33.18	33.19	32.72
6	111	28.55	28.50	28.24
	200	33.18	33.13	32.72
7	111	28.49	28.43	28.24
	200	33.20	33.11	32.72
8	111	28.61	28.58	28.24
	200	33.10	33.03	32.72

Table 9 – Comparing two methods for calculating size and strains in each UO_2 samples.
(a) Size calculations:

Sample	M1 Size Before (nm)	M2 Size Before (nm)	Δsize (nm)	Difference %	M1 Size After (nm)	M2 Size After (nm)	Δstrain	Difference %
1	61.60	51.35	10.24	16.6%	44.39	69.33	24.9383	56.18%
2	77.34	44.73	32.61	42.2%	46.23	53.33	7.0997	15.36%
3	80.48	19.26	61.22	76.1%	17.99	138.65	120.6671	670.86%
4	74.98	13.73	61.25	81.7%	20.56	24.76	4.2018	20.44%
5	35.97	44.73	-8.76	24.3%	32.18	66.03	33.8483	105.19%
6	59.12	53.33	5.79	9.8%	36.96	72.98	36.0139	97.44%
7	47.70	86.66	-38.96	81.7%	31.93	34.66	2.7335	8.56%
8	50.67	2.47	48.21	95.1%	38.31	11.75	-26.5627	69.33%
Average	**60.98**	**39.53**	**21.45**	**53.4%**	**33.57**	**58.94**	**25.3675**	**130.4%**

(b) Strain calculations:

Sample	M1 Strain Before	M2 Strain Before	Δstrain	Difference %	M1 Strain After	M2 Strain After	Δstrain	Difference %
1	0.0019	0.0150	-0.0131	705.8%	0.0020	0.0066	-0.0045	224.1%
2	0.0196	0.0125	0.0071	36.1%	0.0176	0.0080	0.0096	54.6%
3	0.0029	0.0031	-0.0001	5.0%	0.0074	0.0139	-0.0065	88.6%
4	0.0025	0.0004	0.0021	83.9%	0.0106	0.0197	-0.0091	85.8%
5	0.0066	0.0141	-0.0076	114.7%	0.0055	0.0094	-0.0039	71.8%
6	0.0034	0.0066	-0.0032	94.1%	0.0044	0.0092	-0.0048	108.0%
7	0.0076	0.0088	-0.0012	15.9%	0.0101	0.0070	0.0031	30.8%
8	0.0080	0.0340	-0.0261	327.1%	0.0090	0.0113	-0.0023	25.8%
Average	**0.0066**	**0.0118**	**0.0053**	**172.8%**	**0.0083**	**0.0106**	**0.0023**	**86.2%**